Adaptive Nonlinear Control for Robust Trajectory Tracking and Energy Saving of a Quadrotor Helicopter

(4ロータヘリコプタのロバスト軌道追従と
省エネルギー化のための適応非線形制御)

January, 2018

Doctor of Philosophy (Engineering)

Reesa Akbar

Toyohashi University of Technology

Abstract

Compared with manned systems, the viability of unmanned aerial vehicles (UAVs) for a wide range of low-cost applications, e.g., aerial photography, construction inspection, and surveillance, makes them an interesting topic of research. UAVs can operate in conditions that are out-of-reach of humans, such as monitoring the disaster areas of a damaged nuclear plant. UAVs with rotary wings (i.e., a rotorcraft) offer better advantages than those with fixed wings in terms of the ability to perform vertical takeoffs and landings. Moreover, within the rotorcraft class, a quad-rotor helicopter (quadcopter) has simpler mechanical elements and is more agile in maneuvers generated by varying the propeller speed than a conventional-rotor helicopter. In general, aerodynamic forces, gyroscopic effect, altitude variation, and wind payload and resources, influence the overall control performance of UAVs. Therefore, rotorcrafts require a robust controller system to compensate the uncertainties and external disturbances. Furthermore, given that a quadcopter has limited operational time owing to limited power supply capacity, the energy consumption during operations should be efficient to prolong running time.

A quadcopter system has six degrees of freedom (DOFs) and is controlled by four independent inputs. It is described as an underactuated system if the numbers of inputs and outputs are different. Therefore, all DOFs become difficult to directly control at once. To make the system fully

actuated, a virtual input is introduced, and a decoupled system where each motion input can be controlled independently is implemented. As a result, a cascade control structure can be constructed on the basis of the translational and rotational dynamics of the system. The experimental quadcopter testbed can only provide measurements of absolute position and attitude states on each sampling time. Thus, we applied a velocity state estimator based on a reduced-order observer, which performs estimations via a time-continuous dynamic model, by considering a discrete-time control system. We experimentally verified the effectiveness of the control structure and the observer by using a sliding-mode controller.

In this study, we introduce an adaptive nonlinear design for robust tracking and energy saving control based on the sliding-mode control (SMC) of quadcopter dynamics. Our thesis aims to design SMC strategies that can effectively control systems that are influenced by uncertainty/disturbance. A conventional sliding-mode controller (SMCr) exhibits high-frequency oscillations in the control input (i.e., chattering), which potentially damages the actuators and increase energy consumptions. Furthermore, most SMC designs require information on the boundary of disturbance, which is difficult to obtain in practical cases.

To reduce chattering in terms of uncertainty, we propose an adaptive gain tuning mechanism based on the super-twisting algorithm (STA), which can dynamically decrease control gain relative to the magnitude boundary layer of the sliding variable. In this case, information on the uncertainty/disturbance boundary is not necessarily required. An adaptive sliding-mode aims to dynamically increase the control gain until the two-sliding-mode is reached, where the gain starts reducing uncertainty and becomes reversible as soon as the sliding variable or its derivative starts deviating from the two-sliding-mode equilibrium points.

Therefore, our adaptive STA utilizes the boundary layer of the sliding-mode as "limiter" because it prevents the overestimation of the control gain. Once the sliding variable achieves the under-boundary layer condition, the control gain is dynamically reduced until the condition is reversed. Thereafter, the control gain dynamically increases to force the sliding variable to reach the previous condition in finite time.

Our adaptive sliding-mode strategy is used to design a modified STA controller, which is a second-order SMCr (SOSMCr) for quadcopters. To improve the transient performance of the quadcopter, we further propose a nonlinear sliding surface (NLSS)-based adaptive chattering-free SMCr. The NLSS changes the closed-loop dynamic damping ratio from an initial low value to a final high value with respect to the error magnitude. Therefore, fast initial response and a gradual decrease of overshoot is expected.

We evaluated the robustness and energy efficiency of the adaptive gain STA with the NLSS via a simulation and a quadcopter experimental testbed.

Acknowledgement

Alhamdulillahi Rabbil Aalamiin, Praise to Allah SWT, the most gracious and merciful, who gave His guidance, will and strength so that I could finish my study in TUT.

First and foremost, I would like to express my sincere gratitude to my supervisor Prof. Naoki Uchiyama for his invaluable help, patience, support, guidance and encouragement to the success of my study under his System Engineering laboratory.

I extend my thanks to the committee members Prof. Hideki Yanada and Prof. Jun Miura for their great support, constructive ideas, and suggestions in writing this thesis.

Sincere thanks to all my friends and colleagues for the friendship, memories, kindness and moral support during my study.

I would like to acknowledge Directorate General of Higher Education of Ministry of Research, Technology and Higher Education of the Republic of Indonesia for providing the scholarship, and also Politeknik Elektronika Negeri Surabaya (PENS) for support during my PhD study in TUT.

Finally, my deepest gratitude goes to my lovely wife Kenya Permata K. and my daughters Harumi, Miyosi, Akinaomi for their remote encouragement, endless support that gave to me during the completion of my study. I am also indebted to my mother Soendari Kabat, my father-in-law Prof. Toho and mother-in-law Luluk R, my brothers and sister for support and praying for my success.

List of Publications

List of Papers/Journals

1. Reesa Akbar, Bambang Sumantri, Hitoshi Katayama, Shigenori Sano, and Naoki Uchiyama, "Reduced-Order Observer Based Sliding Mode Control for a Quad-Rotor Helicopter," *Journal of Robotics and Mechatronics*, 2016, vol. 28, no. 3, pp. 1–16. (Chapter 3)

2. Reesa Akbar and Naoki Uchiyama, "Design and Experiment of Adaptive Modified Super-Twisting Control with a Nonlinear Sliding Surface for a Quadrotor Helicopter," *Advances in Mechanical Engineering*, 2018, vol 10 , no. 10, pp. 1-19 (Chapter 4)

List of Papers at International Conference

1. Reesa Akbar and Naoki Uchiyama, "Adaptive Modified Super-Twisting Control for a Quadrotor Helicopter with a Nonlinear Sliding surface," *SICE International Symposium on Control Systems*, 2017, pp. 93–98 (Chapter 4)

Contents

List of Figures

List of Tables

Chapter 1

Introduction

1.1 Introduction

1.1.1 Background

Unmanned aerial vehicles (UAVs) are an interesting topic of research because of their viability in a wide range of applications (e.g., aerial photography, inspecting construction, and surveillance) and their low cost compared with manned systems. On a more practical note, UAVs allow operations in conditions beyond the reach of human pilots, such as the monitoring of disaster-prone areas due to a damaged nuclear plant. Rotor-winged UAVs (i.e., rotorcrafts) have better takeoff and landing capabilities than fixed-winged UAVs. Furthermore, in rotorcrafts, a quadrotor helicopter (quadcopter) has simpler mechanical elements and is more agile in maneuvers generated by varying the propeller speed than a typical helicopter. Therefore, the quadcopter as an autonomous UAV is a good research platform.

Functionally, the quadcopter has limited operational time because of its limited power supply capacity. The energy consumption of UAVs while in operation should be considered because efficient utilization extends its

functional time capability. Some studies have been conducted for energy consumption reduction in quadcopters. Roberts et al. [2] proposed a ceiling placement feature that maintains a bird's-eye view for aerial exploration in an indoor environment because the actuators are allowed to cut off the power source and stop the propellers; this feature improves indoor task performance by using the energy saved. Aleksandrov and Penkov [3] proposed quadcopter energy optimization by evaluating the maximal distance of the gap between the rotors to allow the rotors to generate optimal thrust. Fresk and Nikolakopoulos [4] introduced variable propeller design, rather than a fixed propeller, for pitch to improve the power efficiency of the actuators. These studies focused on energy consumption without considering the algorithm used by the controller and the design of the platform or mechanical parts of the quadcopter.

In general, a quadcopter system is composed of six degrees of freedom (DOFs) and is controlled by four independent inputs. This type of system becomes underactuated if there is a difference between the numbers of inputs and outputs; furthermore, the control of all DOFs directly and simultaneously becomes difficult. There are two types of control structure that can be developed for a quadcopter. On one hand, a cascade control structure can be constructed with outer and inner loops, thus respectively dividing the quadcopter dynamics into two types: (a) translational, which is governed by an underactuated system, and (b) rotational, which is governed by a fully actuated system [5–16]. Algebraic calculations are required to control the input in the underactuated system of the outer loop. On the other hand, the block control structure of dynamics system can be divided into two main blocks: (a) a fully actuated block provides the altitude and heading angle dynamics, and (b) an underactuated block provides the longitudinal and latitudinal dynamics [17–25]. Correspondingly, to obtain the control input, the fully

actuated dynamics can have an independent design, but the underactuated dynamics will require different strategies (i.e., block or backstepping control techniques).

The first control structure is simpler to construct than the second because a generic method can be employed for the design of its control mechanism by considering all motions at once. However, an overdetermined problem occurs, and quadcopter translational motion dynamics requires the solution of three equations with a single control input to obtain the control input for all motions. Conventionally, the control input in translational dynamics is solved by either considering or neglecting the equation of a fully actuated system in altitude motion to assume a zero angle heading. Several motions but not all are allowed for these methods. However, considering all motions and real variable states is a better option because it obtains an optimal control input.

1.1.2   Control of Quad-Rotor Helicopter

Control performance depends significantly on the available information on quadcopter states, which are often difficult to measure using sensors alone [26]. Quadcopter displacement, such as position and attitude, is measured by visual sensors or global positioning systems (GPSs) to generate velocity information numerically and obtain such states. An inertial measurement unit (IMU) measures the linear acceleration and angular velocity of the quadcopter, and these parameters are integrated numerically to obtain all states.

In most practical applications, a control system is developed via a digital computer acting as the discrete-time controller of a continuous-time system. System dynamics is generally modeled as nonlinear continuous-time systems. Designing a controller via a digital computer requires

the consideration of dynamics as a discrete-time system consisting of a sampler (i.e., analog-to-digital converter) and a zero-order holder (i.e., a digital-to-analog converter, which is alternatively known as a sampled-data system) [27]. Considering that an exact discrete-time model of a nonlinear system may be difficult to obtain, a simple approximation via the Euler model of a quadcopter may prove sufficient [28]. Moreover, it could be challenging to design a Euler-model-based observer, including a practical, semiglobal, discrete-time, reduced-order observer [29, 30] which can estimate the velocity states by using sensor-available position and attitude data.

A quadcopter exhibits a highly nonlinear and time-varying behavior and is influenced by unpredictable disturbances, i.e., wind gusts, particularly in an outdoor environment. Therefore, controller design and the stabilization of fully autonomous quadcopters remain a challenge. To date, several control strategies have been proposed. For instance, linear control strategies have been implemented [31–39]. Pounds et al. [33,34] introduced a proportional integral differential (PID)-based controller to regulate the quadcopter attitude. Bouabdallah et al. [31] presented a linear quadratic controller and compared it with the classical PID controller. Moreover, Refs. [36, 37] and [38] proposed proportional differential (PD)- and proportional integral (PI)-based controllers, respectively.

Many studies have attempted nonlinear control strategies. Refs. [6, 10–12, 40–43] employed feedback linearization to control a quadcopter. Refs. [10–12]combined feedback linearization with an observer to control flight without focusing considerably on the sensors. In fact, feedback linearization has been applied to control a partially dynamic system based on a fully actuated subsystem and has been combined with an observer to obtain information on translational dynamics. Mian and Daobo [15] employed a PD controller, along with feedback linearization,

to control the translational motion of a quadcopter. They also designed a backstepping-based PID nonlinear controller for the rotational motion of a rotorcraft. Refs. [16, 44] adopted a backstepping method, and Refs. [24, 45–47]considered a nested input saturation.

Nevertheless, these linear-based or feedback linearization control strategies were unsuccessful in handling uncertainties/disturbances, which can be addressed by the sliding-mode control (SMC) strategy, owing to specific characteristics of robustness against disturbance, uncertainty, unmodeled dynamics, and invariance during a sliding-mode. SMC was applied to a quadcopter in Refs. [6,9,13,14,17,19–23,48–61] and in Refs. [9, 13,56] where it was combined with an observer to increase the quadcopter control performance against an external disturbance. Furthermore, Refs. [20, 21] employed an SMC based on the block control technique to solve an underactuated problem.

1.1.3   Sliding-Mode Control

Initially introduced in the early 1950s as a class of variable structure control, SMC has continually attracted research attention because of its simple design [62, 63]. SMC is categorized as a robust controller owing to its invariant property given its simplicity, thus suggesting that its system is insensitive against parametric uncertainty and external disturbance [64] (Fig. 1.1). An SMC has two design stages: (1) design of a stable sliding surface to obtain the desired control performance and (2) design of a control mechanism to force the system states to reach the sliding surface and consequently make it an invariant manifold.

Given its robustness, SMC still suffers from chattering, which is a phenomenon effected by a high-frequency switching control type. In an ideal SMC, the controller is assumed to switch with an unlimited
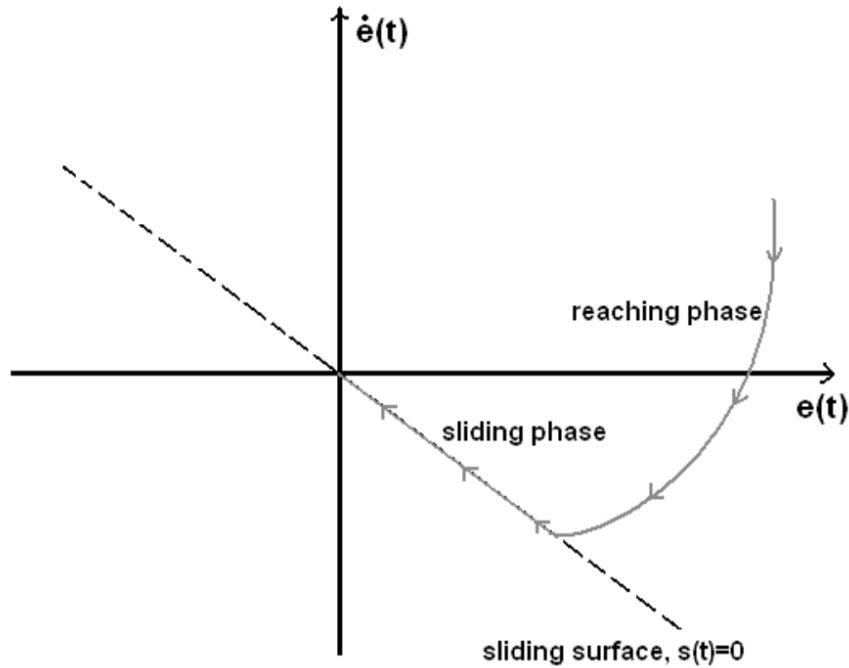
Figure 1.1: Phase portrait of a sliding motion in sliding-mode control [1]

frequency range. However, given the limitation of the actuators and the sampling time of the digital device in real-world implementations, the controller is switched at certain high-frequency restrictions, thus resulting in chattering. At high frequencies, chattering potentially damages the actuator and increases the energy consumption of the system. Therefore, SMC should be designed to reduce this occurrence. A continuous-type controller may replace the switching controller to effectively achieve this objective for a boundary layer around the sliding surface [65]; however, this type of controller eliminates the robustness of the invariant property inside the layer.

1.1.4   Second-Order Sliding-Mode Control

Another promising solution to reduce the chattering phenomenon is the second order sliding-mode control (SOSMC) which guarantees the existence of invariant property [66]. In this method, the switching controller occurs in the second-time derivative of the sliding variable

because the standard SMC occurs in the first derivative. SOSMC feasibly increases the control accuracy with an integral part obtaining the control input.

The super-twisting algorithm (STA) is a popular SOSMC technique. It consists of power-rate and integral-constant-reaching mechanisms, which require only the sliding variable information that is applicable for practical cases, whereas other SOSMC methods require the first derivative of the variable. The trajectory of STA in a phase plane is described in a twisting form. Refs. [20, 22, 23, 58–60] employed STA on a quadcopter; nevertheless, it only provides strong behavior to a system that is close to a sliding-mode condition because of the nonlinear square-root part in the control mechanism.

Another method considered a linear correction term that possesses strong behavior as the system moves away from the sliding-mode condition and an equivalently weak characteristic as the system closes in. Therefore, combining the advantages of STA and the linear term may provide strong behavior at both ends of the initial condition spectrum and allow the system to endure a linearly growing perturbation. Refs. [67, 68] introduced this method, and Refs. [69, 70] tried it on a quadcopter.

1.1.5 Adaptive Sliding-Mode Control

Chattering is the main drawback of the SMC. There are two common approaches that are applicable for reducing the effect of this phenomenon. First, a boundary layer can be used to consider appropriate controller gain tuning. Second, a higher-order SMCr, such as SOSMCr, may be adopted. Nevertheless, knowledge of the uncertainty boundedness is required in both approaches.

Considering that we aim to consider the case where the boundedness

of uncertainties can be disregarded, the adaptive sliding-mode is a suitable technique because it can maintain a dynamic control gain adaptation value that is as small as possible to compensate the uncertainty.

Huang et al. [71] proposed direct control gain dynamics, which depends on the sliding variable without knowledge of uncertainty boundedness; hence, the control gain continually increased to an overestimation that increased the chattering amplitude. Lee and Utkin [72] proposed decreasing the control gain by using an equivalent control to reduce chattering. However, the gain adaptation law requires the knowledge of uncertainty bounds.

On the basis of a previous work [71], Plestan et al. [73] proposed gain dynamics for a first-order SMC, which depends on the sliding variable by adding a bounded sliding-mode layer to rule out the dynamics. Here the control gain decreased with a small magnitude of the sliding variable. By contrast, when the magnitude was high, the control gain increased until the sliding-mode was established and then subsequently decreased. To maintain a positive control gain in the controller, the adaptation law required an additional condition for the minimum control gain, and the gain was increased to enable the adaptation process. Shtessel et al. [73] extended Ref. [74] for a super twisting controller by using linear gain adaptation and considered control gain dynamics, which is proportional to other STA control gains.

1.1.6 Nonlinear Sliding Surface

The design of a sliding surface contributes to the overall performance of the closed-loop dynamics of a control system. A basic sliding surface can be achieved using a linear differential function of a proportional gain [65, 75]. Moreover, the addition of an integral part may improve

tracking performance [76, 77]. The gain of a sliding surface can affect the performance of the controller. For instance, a high gain can obtain a fast response but may make the system unstable, whereas a small gain may provide a slow response but may make the system very stable [78]. Alternatively, SMC performance may improve with a time-varying sliding surface [75, 78–92]. Promkajin and Parnichkun [75] designed an adaptive sliding surface for the attitude and altitude control of a quadcopter. Refs. [78–81] developed a fuzzy system strategy to update the parameters of sliding surface. Salamci and Tombul [82] designed a time-varying sliding surface that is performed like a linear time-invariant system for a nonlinear system via a frozen-time approach. Furthermore, Refs. [49, 70, 83–93] proposed a sliding surface based on a nonlinear function.

1.2 Motivation and Research Objectives

A stable sliding surface permits the evaluation of SMC robustness for quadcopter applications with a specific cascade control structure. In this type of sliding surface, the measurement of position and velocity is necessary. Real-life applications portray a minimalist quadcopter that is usually equipped with basic equipment, such as an ultrasonic sensor for altitude measurement and GPS-tracking. Nonetheless, SMC necessitates a velocity sensor, in addition to these minimum equipment requirements.

As a sign of robust control performance, an autonomous quadcopter has to counteract the effects of uncertainties/disturbances and the limited operational time due to limited power supply capacity. Given that energy consumption is proportional to the control input, saving energy by modifying only the control algorithm into existing hardware is a highly efficient and low-cost strategy. Ref. [49, 69] applied SMC to control motion,

obtain robust tracking, and save energy for a quadcopter system. As emphasized herein, the main challenges SMC designs face include the chattering phenomenon and the knowledge requirement of disturbance in gradient boundary layers, which is insurmountably difficult to obtain in most practical cases. These two issues result in an overestimated control gain, which negatively affects the control performance and energy utilization of the quadcopter system.

On the basis of the above reasons, our thesis aims to achieve two objectives for a quadcopter:

1. Apply SMC over a cascade control structure only via the observation of positional states without necessarily obtaining the knowledge of velocity measurements.

2. Apply the modified adaptive SOSM [94] to reduce chattering and save energy for extended operational times without necessarily having knowledge of uncertainty/disturbance boundedness and without control gain overestimation.

1.3   Thesis Contributions

The main contributions of this thesis are as follows:

1. It presents a reduced-order observer design for the estimation of velocity states by using first-order SMC over a cascade control structure.

2. It introduces the design of a robust and energy-efficient SMC strategy for quadcopters based on STA-SMC with an adaptive gain and a nonlinear sliding surface (NLSS) for indoor environment applications.

1.4   Thesis Organization

This thesis contains five chapters. A brief description of the contents in each chapter is presented as follows:

- Chapter 2: This chapter describes the kinematic and dynamic models of a quadcopter obtained through the application of the Newton–Euler formulation for a 6-DOF rigid body in free motion, with two referential coordinate frames. Furthermore, we obtained the thrust force of a real motor from empirical formula with respect to voltage. The resistance of the real motor is estimated to obtain the energy consumption, and the quadcopter experimental testbed applied is explained together with the sensor configuration and the testbed parameters.

- Chapter 3: This chapter presents the cascade control structure of the quadcopter governed by a least squares algorithm that solves the control input problem in a given translational motion dynamics. A reduced-order observer is presented and applied for the estimation of the velocities of the quadcopter experimental testbed from the measured position states. The effectiveness of the control structure and the reduced-observer design are evaluated experimentally by applying a first-order SMC controller.

- Chapter 4: • An SOSMC based on a modified STA with adaptive gain (ASTA) and NLSS is presented for the robust tracking control of a quadcopter. The ASTA controller is designed to control tracking performance without knowledge of the boundary of disturbances, and the NLSS equation, as a function of tracking error, is designed as the time-varying properties of the closed-loop dynamics (damping ratio and natural frequency) to minimize the tracking error. Lyapunov stability theory is applied to prove the stability of the proposed method in and out of the sliding-mode. Moreover, a comparative study for STA and ASTA is conducted. The effectiveness of these strategies in terms of robustness and

energy efficiency are evaluated with the quadcopter experimental testbed.

 • Chapter 5: This chapter summarizes the important points of the thesis and provides an extended description of future works by the authors.

Chapter 2

Mathematical Modeling of Quadcopter and Experimental Set-up

The kinematic and dynamic quadcopter models presented herein was constructed by applying the Newton–Euler formulation into a 6-DOF rigid body in free motion. A quadcopter experimental testbed was presented and elaborated, along with the configuration of sensors and the testbed parameters.

2.1 Modeling of Quadcopter

A quadcopter is a famous multirotor aerial robot with its four rotors attached on the propeller. It has a symmetrical body of two arms crossing each other and has propellers in a fixed and parallel configuration. A pair of rotors (M2 and M4) rotates clockwise, whereas the other pair (M1 and M3) rotates in a counterclockwise motion. To obtain an upward force f_j with $j = 1, .., 4$ representing the j-th motor, all propellers are built and attached to rotors so that the air flow points downward according to the described

rotation direction. In this structure, all rotors form a rigid link network where the only variables are their velocities [35].

2.1.1   Kinematics Modeling
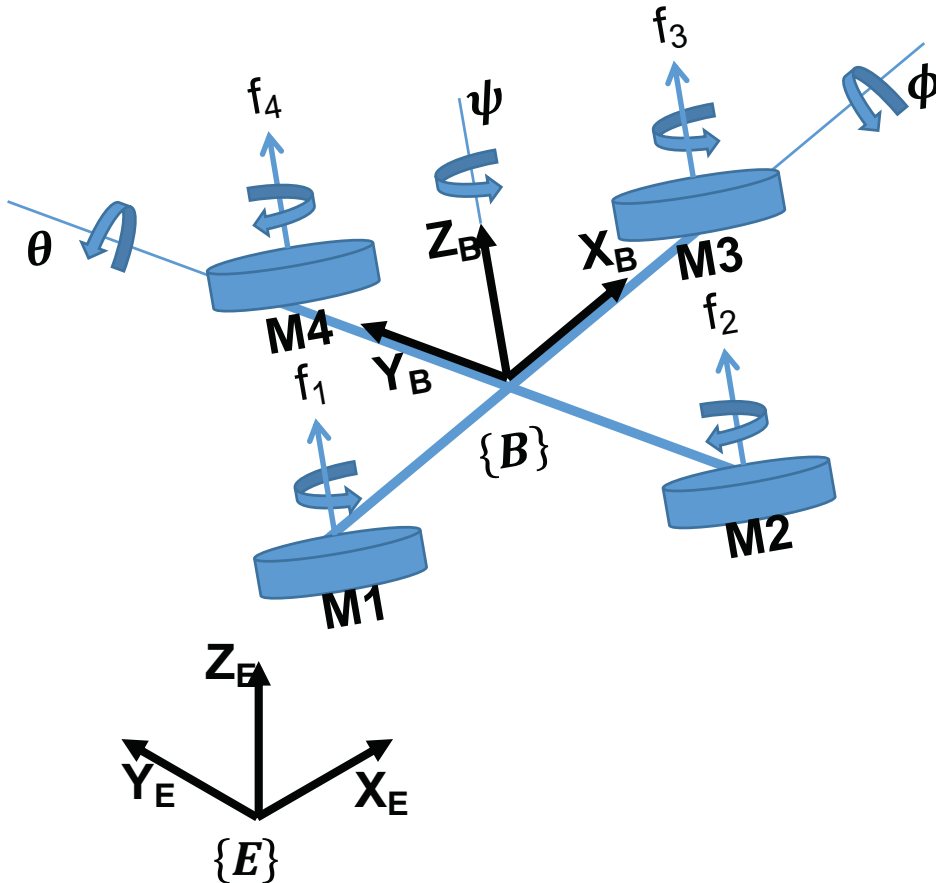
Figure 2.1: Quadcopter model

To describe a 6-DOF rigid body, two reference frames need to be defined: the inertial/earth reference as frame {E} and the body-fixed reference as frame {B}. Frame {B} is a fixed at the center of gravity of the quadcopter, where the rotor axes point to the positive $z-$axis, and the two cross arms point to $x-$ and $y-$axes. On the contrary, frame {E} is a rigid body with respect to the ground. The pose of the quadcopter is a 6-DOF vector composed of a linear and an angular position. In frame {E}, we express

the pose of the quadcopter as $\xi = [X^T, \; \Theta^T]^T$, where $X = [x, y, z]^T[\mathrm{m}]$ is a Cartesian coordinate position vector; $\Theta = [\phi, \theta, \psi]^T[\mathrm{rad}]$ is an orientation vector representing the pitch, roll, and yaw angle rotations along the x, y, and z-axes, respectively; $\dot{X} = [\dot{x}, \dot{y}, \dot{z}]^T[\mathrm{m/s}]$ and $\dot{\Theta} = [\dot{\phi}, \dot{\theta}, \dot{\psi}]^T[\mathrm{rad/s}]$ are the linear and angular velocities, respectively.

Given that the quadcopter has only four independent inputs with 6-DOFs, it falls under the underactuated system category. Therefore, its motions are controlled by the inputs produced from the combination of its four rotors (Fig. 2.1). The four independent inputs that represent the movement of the quadcopter are as follows:

1. Throttle (u_1 [N])

This force is directly related to the linear acceleration along the z-axis. Throttle motion is obtained by varying the velocity of all rotors by the same amount to create a vertical force that pushes up or pulls down the quadcopter body. In the case of hovering, the throttle force causes the quadcopter to fly up or down with unchanged x and y positions.

2. Roll (u_2 [N.m])

This torque is directly related to the angular acceleration along the x-axis. The roll motion is obtained by maintaining the speeds of M1 and M3 while varying those of M2 and M4 so that the body rotates along the x-axis. A negative roll is obtained by decreasing the speed of M4 while increasing the speed of M2 at an equivalent rate.

3. Pitch(u_3 [N.m])

This torque is directly related to the angular acceleration along the y-axis. Similar to roll motion, pitch motion is obtained by maintaining the speeds of M2 and M4 and varying those of M1 and M3 by the same amount. A positive pitch is achieved by increasing the speed of M1 while decreasing that of M3 by the same amount; conversely, a negative pitch occurs when the speed of M1 decreases while the speed of M3 increases at the same rate.

4. Yaw (u_4 [N.m])

This torque is directly related to the angular acceleration along the z-axis. It uses a pair of rotors that moves clockwise and another pair that moves counterclockwise. Varying the speeds of these rotors in both rotations creates a difference and imbalance in the torques along the z-axis, and make the body rotated along the same axis.

Eq. (2.1) describes the relation between the body movement and thrust force generated from each propeller velocity.

$$
\begin{bmatrix} u_1 \\ u_2 \\ u_3 \\ u_4 \end{bmatrix} = \begin{bmatrix} 1 & 1 & 1 & 1 \\ 0 & -L & 0 & L \\ L & 0 & -L & 0 \\ -d & d & -d & d \end{bmatrix} \begin{bmatrix} f_1 \\ f_2 \\ f_3 \\ f_4 \end{bmatrix}
\tag{2.1}
$$

Here, L[m] is the distance of each rotor from the center of gravity, and d[Nms^2] is a scaling coefficient from force to moment.

The position and orientation in {E} are measured from the sensors attached on the body in {B}. Here, the linear and angular velocity in {B} are denoted by ν and ω. Frames {E} and {B} are related by a rotation and a translation of the rigid body transformation. The translation of frame {B} with respect to frame {E} is the vector itself. The rotation frame {B} with respect to frame {E} is a rotation matrix given by Eq. (2.2) where s and c denote the sine and cosine variables, respectively.

$$R_\Theta = R_z(\psi)R_x(\phi)R_y(\theta)$$

$$
= \begin{bmatrix} c\psi & -s\psi & 0 \\ s\psi & c\psi & 0 \\ 0 & 0 & 1 \end{bmatrix} \begin{bmatrix} 1 & 0 & 0 \\ 0 & c\phi & -s\phi \\ 0 & s\phi & c\phi \end{bmatrix} \begin{bmatrix} c\theta & 0 & s\theta \\ 0 & 1 & 0 \\ -s\theta & 0 & c\theta \end{bmatrix} \tag{2.2}
$$

$$
= \begin{bmatrix} -s\phi s\theta s\psi + c\theta c\psi & -c\phi s\psi & s\phi c\theta s\psi + s\theta c\psi \\ s\phi s\theta c\psi + c\theta s\psi & c\phi c\psi & -s\phi c\theta c\psi + s\theta s\psi \\ -c\phi s\theta & s\phi & c\phi c\theta \end{bmatrix}
$$

The linear velocity of the quadcopter in frame $\{E\}, \dot{X}$, is obtained by
differentiating the vector position X. Here, the relation between linear
and angular velocity in frames $\{E\}$ and $\{B\}$ are described as follows:

$$\dot{X} = R_\Theta v \tag{2.3}$$

where $v = [v_x, \ v_y, \ v_z]^T$ is vector of linear velocity in frame $\{B\}$ [38]. The
linear velocity $\dot{X}$ can be obtained by the required information of Euler
angles Θ. As far as we know, Θ is function of time where $\dot{\Theta}$ depends on
the angular velocity $\omega = [\omega_x, \ \omega_y, \ \omega_z]^T$ of the body of quadcopter which is
measured in frame $\{B\}$. Moreover, we need to obtain the angular velocity $\bar{\omega}$
from the property of rotational matrix R_Θ. From the orthogonal matrix, we
have

$$R_\Theta R_\Theta^T = I$$
$$R_\Theta^T = R_\Theta^{-1} \tag{2.4}$$

By taking the derivative of Eq. (2.4) we have

$$\dot{R}_\Theta R_\Theta^T + R_\Theta \dot{R}_\Theta^T = 0 \tag{2.5}$$

The following equation is obtained from the skew symmetric property of

matrix $S \in SO(3)$ [95]:

$$S(\bar{\omega}) + S(\bar{\omega})^T = 0 \tag{2.6}$$

where $\bar{\omega} = [\bar{\omega}_x, \bar{\omega}_y, \bar{\omega}_z]^T$ is the angular velocity in frame $\{E\}$, and we choose

$$S(\bar{\omega}) = \begin{bmatrix} 0 & -\bar{\omega}_z & \bar{\omega}_y \\ \bar{\omega}_z & 0 & -\bar{\omega}_x \\ -\bar{\omega}_y & \bar{\omega}_x & 0 \end{bmatrix} \tag{2.7}$$

Hence, by using the relation between Eqs. (2.5) and (2.6), we have

$$S(\bar{\omega}) = \dot{R}_\Theta R_\Theta^T \tag{2.8}$$

Considering Eqs. (2.2) and (2.7) (2.8), we can rewrite Eq. (2.8) into:

$$S(\bar{\omega}) = \left(\dot{R}_z R_x R_y + R_z \dot{R}_x R_y + R_z R_x \dot{R}_y \right) R_y^T R_x^T R_z^T$$

$$= \dot{R}_z R_z^T + R_z \dot{R}_x R_x^T R_z^T + R_z R_x R_y R_y^T R_x^T R_z^T$$

$$\begin{bmatrix} 0 & -\bar{\omega}_z & \bar{\omega}_y \\ \bar{\omega}_z & 0 & -\bar{\omega}_x \\ -\bar{\omega}_y & \bar{\omega}_x & 0 \end{bmatrix} = \psi \begin{bmatrix} 0 & -1 & 0 \\ 1 & 0 & 0 \\ 0 & 0 & 0 \end{bmatrix} + \phi \begin{bmatrix} 0 & 0 & s\psi \\ 0 & 0 & -c\psi \\ -s\psi & c\psi & 0 \end{bmatrix} \tag{2.9}$$

$$+ \dot{\theta} \begin{bmatrix} 0 & -s\phi & c\phi c\psi \\ s\phi & 0 & c\phi s\psi \\ -c\phi c\psi & -c\phi s\psi & 0 \end{bmatrix}$$

By relating the equation to the left and right sides of Eq. (2.9), we have

$$\bar{\omega} = \begin{bmatrix} c\psi & -c\phi s\psi & 0 \\ s\psi & c\phi c\psi & 0 \\ 0 & s\phi & 1 \end{bmatrix} \begin{bmatrix} \dot{\phi} \\ \dot{\theta} \\ \dot{\psi} \end{bmatrix} \tag{2.10}$$

Hence, we obtain the relation between the angular velocity in frames

{B} and {E} in Eq. (2.10) as follows:

$$
\omega = R_\Theta^T \bar{\omega} = R_\Theta^T
\begin{bmatrix}
c\psi & -c\phi s\psi & 0 \\
s\psi & c\phi c\psi & 0 \\
0 & s\phi & 1
\end{bmatrix}
\begin{bmatrix}
\dot{\phi} \\
\dot{\theta} \\
\dot{\psi}
\end{bmatrix}
=
\begin{bmatrix}
c\theta & 0 & -c\phi s\theta \\
0 & 1 & s\phi \\
s\theta & 0 & c\phi c\theta
\end{bmatrix}
\begin{bmatrix}
\dot{\phi} \\
\dot{\theta} \\
\dot{\psi}
\end{bmatrix}
$$

$$
\omega = T_\Theta \dot{\Theta}
$$

(2.11)

2.1.2 Dynamics Modeling

The dynamics of a quadcopter is derived by applying the Newton's second
law for translational and rotational motions [5, 10, 15, 33, 48, 96]. Therefore,
in frame {E}, we have

$$
\sum F_{ext} = m\ddot{X}
$$

$$
\sum T_{ext} = I_\Theta \dot{\omega} + \omega \times I_\Theta \omega
$$

(2.12)

where $\sum F_{ext}$ is the total force applied on the body of quadcopter with
respect to frame {E}, m[kg] is the total mass of quadcopter, $\ddot{X} =
[\ddot{x}, \ddot{y}, \ddot{z}]^T$[m/s^2] is the translational acceleration vector in frame {E}, $\dot{\omega} =
[\dot{\omega}_x, \ \dot{\omega}_y, \ \dot{\omega}_z]^T$[rad/s^2] is the rotational acceleration vector in frame {B} and
$\sum T_{ext} = [u_2, \ u_3, \ u_4]^T$ is the total torque acting on the body of quadcopter
with respect to frame {B}. In a rotational motion, we have the inertia
matrix as follows:

$$
I_\Theta =
\begin{bmatrix}
I_{xx} & -I_{xy} & -I_{xz} \\
-I_{yx} & I_{yy} & -I_{yz} \\
-I_{zx} & -I_{zy} & I_{zz}
\end{bmatrix}
$$

(2.13)

where I_{xx}, I_{yy}, and I_{zz} are the moments of inertia with respect to $x-$, $y-$, and
$z-$ axes, respectively. $I_{xy}, I_{xz}, I_{yx}, I_{yz}, I_{zx}$, and I_{zy}, are the products of inertia.
Given that a quadcopter is a rigid body with constant mass and has an axis

that is aligned with the principal axis of inertia, then the product of inertia $I_{xy} = I_{xz} = I_{yx} = I_{yz} = I_{zx} = I_{zy} = 0$, and the inertia matrix in Eq. (2.13) becomes a diagonal matrix as follows:

$$I_\Theta = \begin{bmatrix} I_{xx} & 0 & 0 \\ 0 & I_{yy} & 0 \\ 0 & 0 & I_{zz} \end{bmatrix} \tag{2.14}$$

By substituting Eq. (2.10) together with Eq. (2.2) in the translational motion, we obtain,

$$\ddot{X} = \frac{1}{m} \sum F_{ext} = R_\Theta \begin{bmatrix} 0 \\ 0 \\ \frac{u_1}{m} \end{bmatrix} + \begin{bmatrix} 0 \\ 0 \\ -g \end{bmatrix}$$

$$\begin{bmatrix} \ddot{x} \\ \ddot{y} \\ \ddot{z} \end{bmatrix} = \begin{bmatrix} s\phi c\theta s\psi + s\theta c\psi \\ -s\phi c\theta c\psi + s\theta s\psi \\ c\phi c\theta \end{bmatrix} \frac{u_1}{m} + \begin{bmatrix} 0 \\ 0 \\ -g \end{bmatrix} \tag{2.15}$$

where g is the acceleration due to gravity.

For Newton's second law of rotational motion in Eq. (2.12), substitute using Eq. (2.11) with its derivative, and consider Eq. (2.2), then we have,

$$I_\Theta(\dot{T}_\Theta\dot{\Theta} + T_\Theta\ddot{\Theta}) = -T_\Theta\dot{\Theta} \times I_\Theta T_\Theta\dot{\Theta} + \sum T_{ext} \tag{2.16}$$

where $\dot{T}_\Theta$ is the derivative of the transformation matrix T_Θ in Eq. (2.11) and $\ddot{\Theta} = [\ddot{\phi}, \ddot{\theta}, \ddot{\psi}]^T$ is the angular acceleration vector in frame {E}. By solving Eq. (2.16), we have the following result:

$$\begin{bmatrix} \ddot{\phi} \\ \ddot{\theta} \\ \ddot{\psi} \end{bmatrix} = J^{-1} \begin{bmatrix} K_1\left(\Theta, \dot{\Theta}\right) \\ K_2\left(\Theta, \dot{\Theta}\right) \\ K_3\left(\Theta, \dot{\Theta}\right) \end{bmatrix} + J^{-1} \begin{bmatrix} u_2 \\ u_3 \\ u_4 \end{bmatrix} \tag{2.17}$$

where

$$J = \begin{bmatrix} I_{xx}c\theta & 0 & -I_{xx}c\phi s\theta \\ 0 & I_{yy} & I_{yy}s\phi \\ I_{zz}s\theta & 0 & I_{zz}c\phi c\theta \end{bmatrix}$$

$$K_1 = (I_x + I_y - I_z)\dot{\phi}\dot{\theta}s\theta + (-I_x + I_y - I_z)\dot{\phi}\dot{\psi}s\phi s\theta$$
$$+ (I_x + I_y - I_z)\dot{\theta}\dot{\psi}c\phi c\theta + (I_y - I_z)\dot{\psi}^2 s\phi c\phi c\theta,$$

$$K_2 = (-I_y + (I_z - I_x)c2\theta)\dot{\phi}\dot{\psi}c\phi + (I_z - I_x)(\dot{\phi}^2 - \dot{\psi}^2 c^2\phi)s\theta c\theta,$$

$$K_3 = (-I_z + I_x - I_y)\dot{\phi}\dot{\theta}c\theta + (I_z + I_x - I_y)\dot{\phi}\dot{\psi}s\phi c\theta$$
$$+ (I_z - I_x + I_y)\dot{\theta}\dot{\psi}c\phi s\theta - (I_x - I_y)\dot{\psi}^2 s\phi c\phi s\theta.$$

By combining Eqs. (2.15) and (2.17), we obtain the complete dynamics
model of a quadcopter as follows:

$$\ddot{\xi} = \bar{f}_1(\Theta,\ \dot{\Theta}) + \bar{f}(\Theta,\ u) \tag{2.18}$$

where

$$\ddot{\xi} = [\ddot{x}, \ddot{y}, \ddot{z}, \ddot{\phi}, \ddot{\theta}, \ddot{\psi}]^T, \ J_m = \begin{bmatrix} mI_{3\times3} & 0_{3\times3} \\ 0_{3\times3} & J \end{bmatrix}$$

$$\bar{f}_1(\Theta, \Theta) = J_m^{-1}[0, 0, -mg, K_1(\Theta, \Theta), K_2(\Theta, \Theta), K_3(\Theta, \Theta)]^T,$$

$$\bar{f}_2(\Theta, u)J_m = J_m^{-1}\left[(s\phi c\theta s\psi + s\theta c\psi)u_1, (-s\phi c\theta c\psi + s\theta s\psi)u_1, c\phi c\theta u_1, u_2, u_3, u_4 \right]^T,$$

$I_{3\times3}$ and $0_{3\times3}$ are a 3×3 identity matrix and a 3×3 null matrices,
respectively. The quadcopter dynamics in Eq. (2.18) is obtained by
neglecting the aerodynamics effects and gyroscopic terms. These terms
will be considered as disturbances in the controller design.

2.2   Experimental Set-up
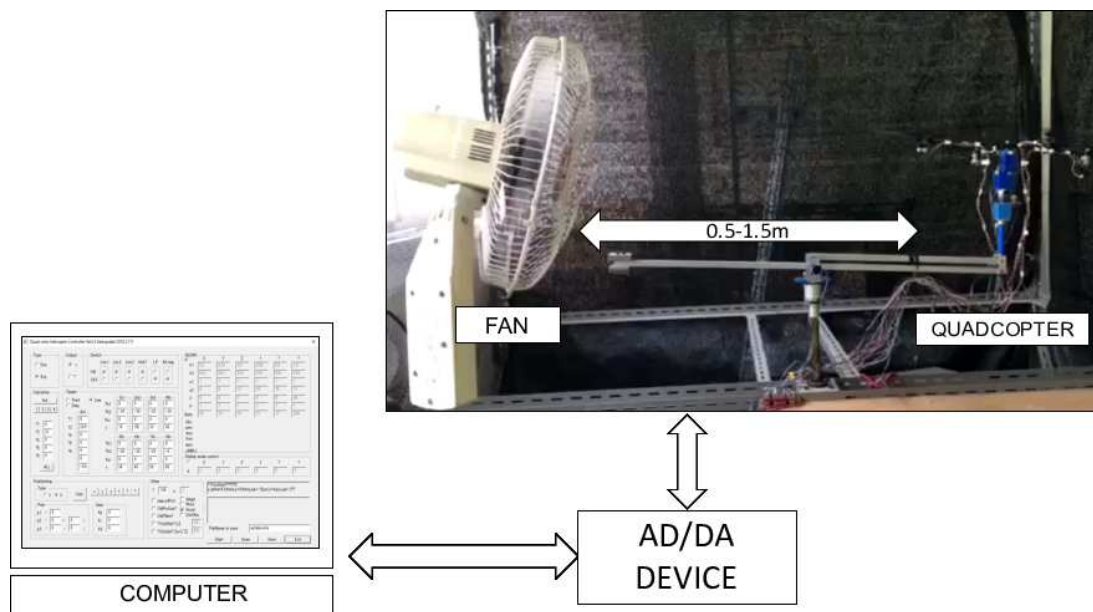
Figure 2.2: Quadcopter configuration for experimental testbed

Figure 2.2 shows the configuration of the testbed used in the experiment. The quadcopter was placed at the rigid links, which also serve as a safety link, to minimize damage or prevent the quadcopter from crashing due to an unstable flight. The links can be operated in fixed motions, i.e., circular and vertical motions with limit attitude motions, which affect the desired trajectory design for the latter experiments. In real-life applications, the rigid links can be assumed as payloads that produce uncertainties and provide tracking error during motion. This testbed is used for multiple times experiment with the same experiment test to verify and evaluate the effectiveness and repeatability of the control strategy.

To operate and control the motions, the controller was developed in a personal computer (PC) and connected to the quadcopter via analog-to-digital (AD) and digital-to-analog (DA) converter devices. The AD converter received state information from the five sensors in the DC voltage, whereas the DA converter sent the control signal generated from the flight controller

in the PC to the actuators of the DC motors.

A 57 W electric fan was placed at a specific position to provide wind
speeds of 4.2–7.7 m/s (from 100–50 cm measurements)[1], which were
applied to the obtained distances of 0.5–1.5 m, to generate a disturbance
for the quadcopter and evaluate the robustness of the control design. The
strength of the disturbances was proportional to the distance between the
quadcopter and the fan.

Potentiometers were attached on each link as shown (Fig. 2.3) to
measure the position states of the quadcopter. From the dynamics model
in Eq. (2.18), a quadcopter appears as a type of second-order system that
requires position information (translational and attitudinal) and velocity
(linear and angular) states for the controller design. Thus, an observer was
developed to estimate the velocity states. The design implemented for the
observer is described in the next chapter. In the succeeding section, we will
discuss the derivation process for determining the position and attitude
states from the sensors of the quadcopter in the testbed.

2.2.1   Sensor Configuration and Coordinate Frame

Figure 2.3 shows the location of the potentiometers $(S_1 - S_5)$, which measure
the variable states for controller, for all positions of the rotational motion
on each link $(\theta_1 - \theta_5)$. To obtain the position of the quadcopter with respect
to frame $\{E\}$, we used a coordinate frame transformation for the rigid
links. Figure 2.4 shows that the assignment of frames $\{B\}$ and $\{E\}$ as
the body and inertial frames of frames {0-5} for each rotational link and of
the rotational angles based on the link. Given that the motion of link L_2
depends on link L_1, then the rotational angle θ'_2 is equal to θ_2. Here, we

---

[1]Fan Speed Cheat Sheet http://www.rechargelabs.org/sites/default/files/WINDSPEED_0.pdf
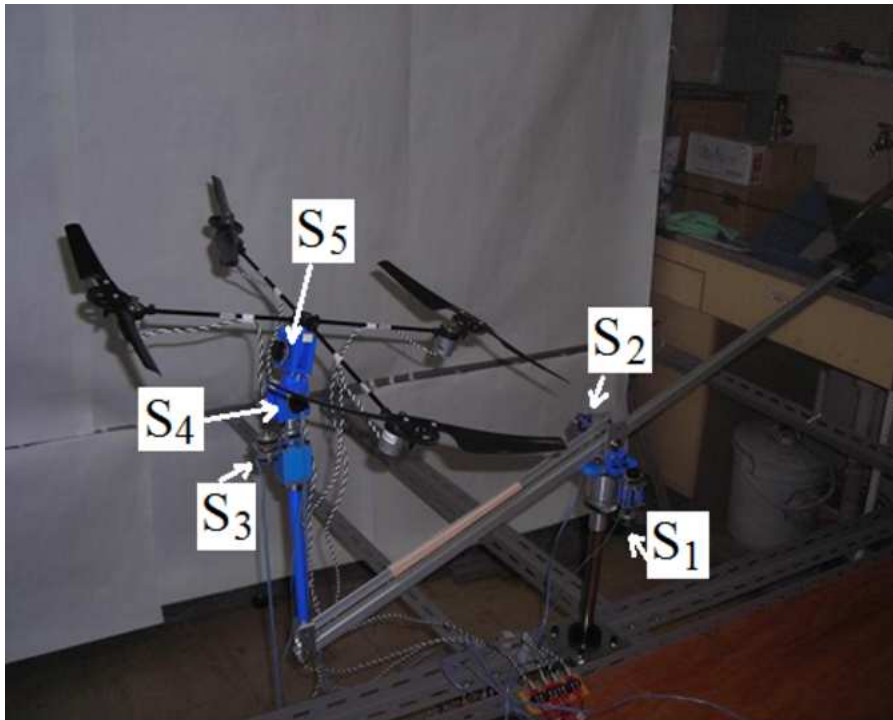
Figure 2.3: Sensors placement on the quadcopter experimental testbed
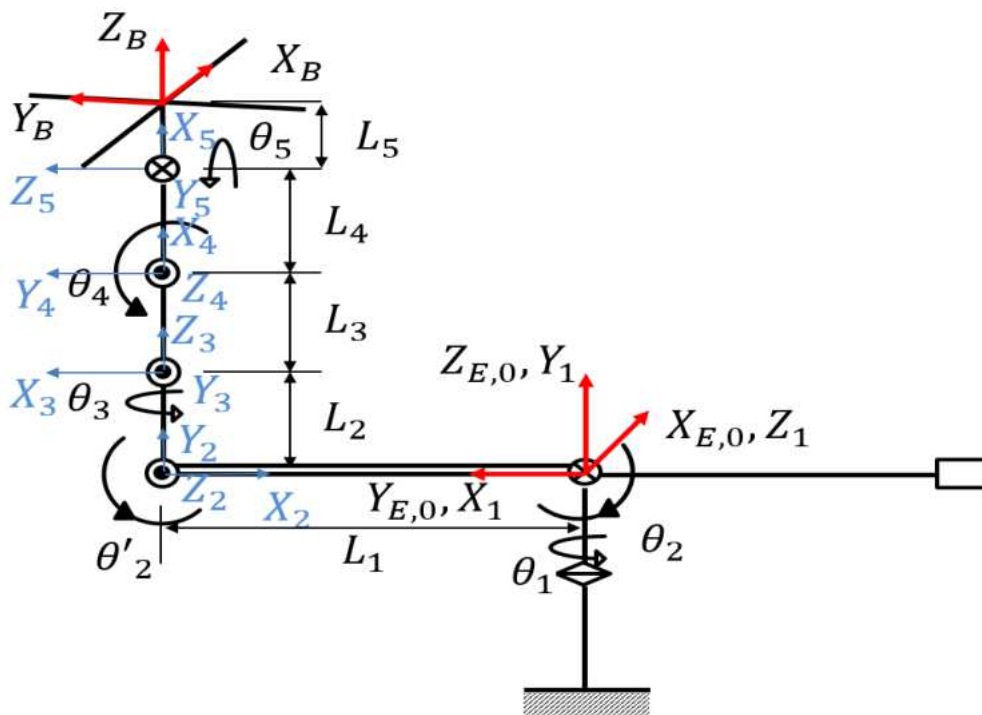
Figure 2.4: Frame transformation on the quadcopter experimental testbed

could describe the transformation matrices for each frame as follows:

$$
{}^E_0T = \begin{bmatrix} c\theta_1 & -s\theta_1 & 0 & 0 \\ s\theta_1 & c\theta_1 & 0 & 0 \\ 0 & 0 & 1 & 0 \\ 0 & 0 & 0 & 1 \end{bmatrix}
\qquad
{}^0_1T = \begin{bmatrix} 0 & 0 & 1 & 0 \\ c\theta_2 & -s\theta_2 & 0 & 0 \\ s\theta_2 & c\theta_2 & 0 & 0 \\ 0 & 0 & 0 & 1 \end{bmatrix}
$$

$$
{}^1_2T = \begin{bmatrix} -c\theta'_2 & s\theta'_2 & 0 & L_1 \\ s\theta'_2 & c\theta'_2 & 0 & 0 \\ 0 & 0 & -1 & 0 \\ 0 & 0 & 0 & 1 \end{bmatrix}
\qquad
{}^2_3T = \begin{bmatrix} -c\theta_3 & s\theta_3 & 0 & 0 \\ 0 & 0 & 1 & L_2 \\ s\theta_3 & c\theta_3 & 0 & 0 \\ 0 & 0 & 0 & 1 \end{bmatrix}
\qquad (2.19)
$$

$$
{}^3_4T = \begin{bmatrix} s\theta_4 & c\theta_4 & 0 & 0 \\ 0 & 0 & 1 & 0 \\ c\theta_4 & -s\theta_4 & 0 & L_3 \\ 0 & 0 & 0 & 1 \end{bmatrix}
\qquad
{}^4_5T = \begin{bmatrix} c\theta_5 & -s\theta_5 & 0 & L_4 \\ 0 & 0 & 1 & 0 \\ -s\theta_5 & -c\theta_5 & 0 & 0 \\ 0 & 0 & 0 & 1 \end{bmatrix}
$$

$$
{}^5_BT = \begin{bmatrix} 0 & 0 & 1 & L_5 \\ 1 & 0 & 0 & 0 \\ 0 & 1 & 0 & 0 \\ 0 & 0 & 0 & 1 \end{bmatrix}
$$

The transformation matrix of body coordinate frame {B} with respect to inertial frame {E} is obtained as follows:

$$
{}^{E}_{B}T = {}^{E}_{0}T\,{}^{0}_{1}T\,{}^{1}_{2}T\,{}^{2}_{3}T\,{}^{3}_{4}T\,{}^{4}_{5}T\,{}^{5}_{B}T =
\begin{bmatrix}
{}^{E}_{B}R & {}^{E}_{B}P \\
0_{1\times3} & 1
\end{bmatrix}
$$

$$
{}^{E}_{B}R =
\begin{bmatrix}
c\theta_5 c\theta_{1+3} + s\theta_4 s\theta_5 s\theta_{1+3} & -c\theta_4 s\theta_{1+3} & s\theta_5 c\theta_{1+3} - c\theta_5 s\theta_4 s\theta_{1+3} \\
c\theta_5 s\theta_{1+3} - s\theta_4 s\theta_5 c\theta_{1+3} & c\theta_4 c\theta_{1+3} & s\theta_5 s\theta_{1+3} + c\theta_5 s\theta_4 c\theta_{1+3} \\
-c\theta_4 s\theta_5 & -s\theta_4 & c\theta_4 c\theta_5
\end{bmatrix} \quad (2.20)
$$

$$
{}^{E}_{B}P =
\begin{bmatrix}
L_5(s\theta_5 c\theta_{1+3} - c\theta_5 s\theta_4 s\theta_{1+3}) - L_1 c\theta_2 s\theta_1 - L_4 s\theta_4 s\theta_{1+3} \\
L_5(s\theta_5 s\theta_{1+3} + c\theta_5 s\theta_4 c\theta_{1+3}) + L_1 c\theta_1 c\theta_2 + L_4 s\theta_4 c\theta_{1+3} \\
L_2 + L_3 + L_1 s\theta_2 + L_4 c\theta_4 + L_5 c\theta_4 c\theta_5
\end{bmatrix}
$$

where $\theta_{1+3} = \theta_1 + \theta_3$.

From Eq. (2.20) and considering Eq. (2.2), the position and attitude of the quadcopter with respect to frame {E} are defined as follows:

$$
\begin{aligned}
X &= [x, \mathrm{y}, z]^T = {}^{E}_{B}P, \\
\phi &= -\theta_4, \\
\theta &= \theta_5, \\
\psi &= \theta_1 + \theta_3
\end{aligned}
\qquad (2.21)
$$

2.2.2 Energy Calculations

The energy consumption can be evaluated by integrating the electric power consumption of each motor of quadcopter during a flight mission. The power consumption can be evaluated when the voltage and resistance of a motor are measured and defined. A thrust force is generated by a voltage motor Therefore, we need to build a thrust force model with respect to a voltage motor, then we can evaluate the energy by using this model.
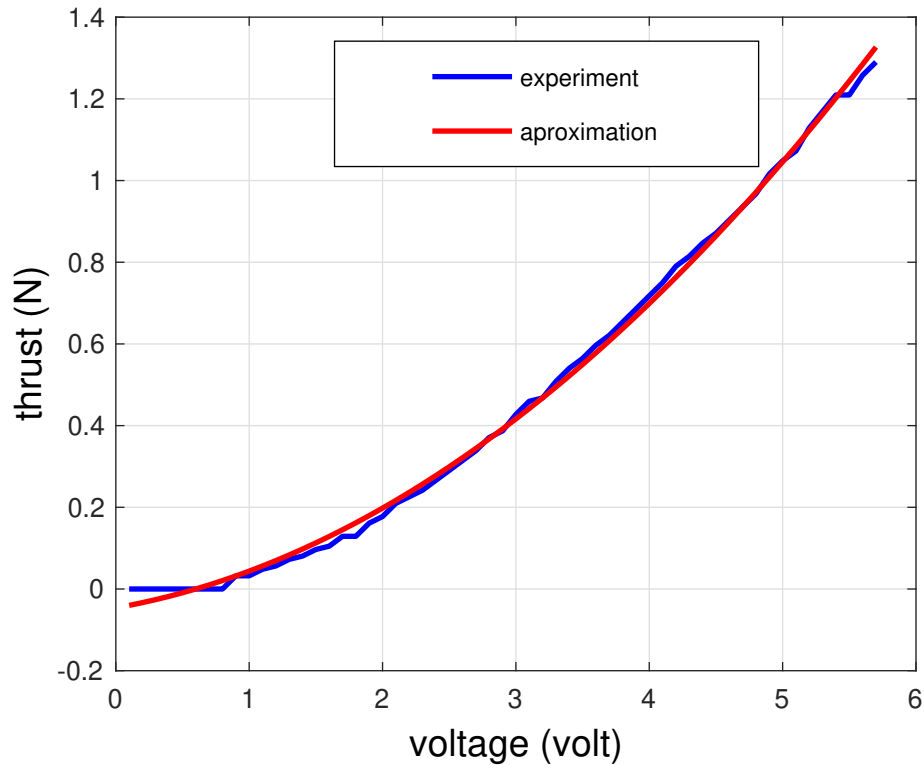
Figure 2.5: Comparison thrust force from experiment and aproximation

2.2.2.1   Thrust Force model

The thrust force of the quadcopter experimental testbed is generated by four motors with gears and blades. Thus, we performed an experiment on the voltage motor driving the rotors to generate thrust and obtain an empirical formula of this force with respect to voltage by using the least squares approximation of a second-order polynomial function (Fig. 2.5). The experiment approach we used was the easiest technique for identifying the thrust model compared with using an analytical model. The thrust model built from the experimental is described as follows:

$$f_j = 0.0321V_j^2 + 0.0579V_j - 0.0462 \tag{2.22}$$

where V_j (volt) is the voltage applied to the j-th motor ($j = 1, \ldots, 4$). Subsequently, we used Eq. (2.22) to estimate each thrust force f_j(N) in
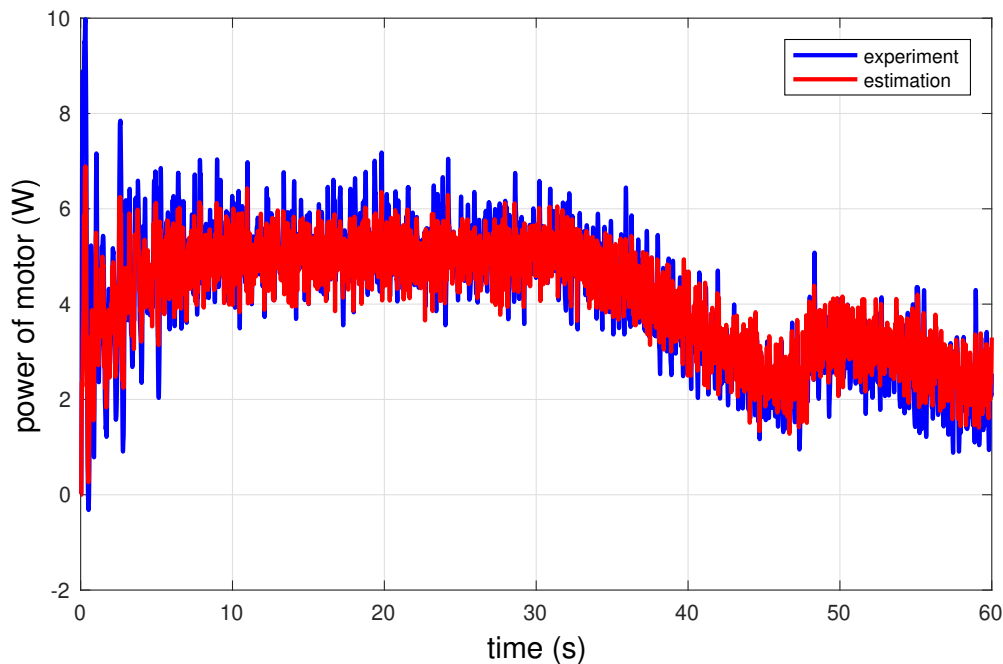
Figure 2.6: Electric power of a motor in hovering motion from experiment measurement and estimated calculation with $R_j = 2.975$ ohm

the experiment.

2.2.2.2 Electric Power Consumption

To calculate the total energy consumption for a completed flight mission, we evaluated the power consumption of a DC motor of the quadcopter during flight by considering the motor as a resistance load and exploiting the following energy equation:

$$P_j = \frac{V_j^2}{R_j} \tag{2.23}$$

where P_j and R_j are the power and resistance of the j-th motor, respectively. Here, the value of R_j is estimated by conducting several experiments and the P_j for one motor is measured by applying V_j to Eq. (2.23). By following this procedure, we estimated the resistance as $R_j = 2.975$ ohm.

Moreover, we validated R_j by allowing the quadcopter to perform a hovering motion on the testbed, as guided by types of experiment, and
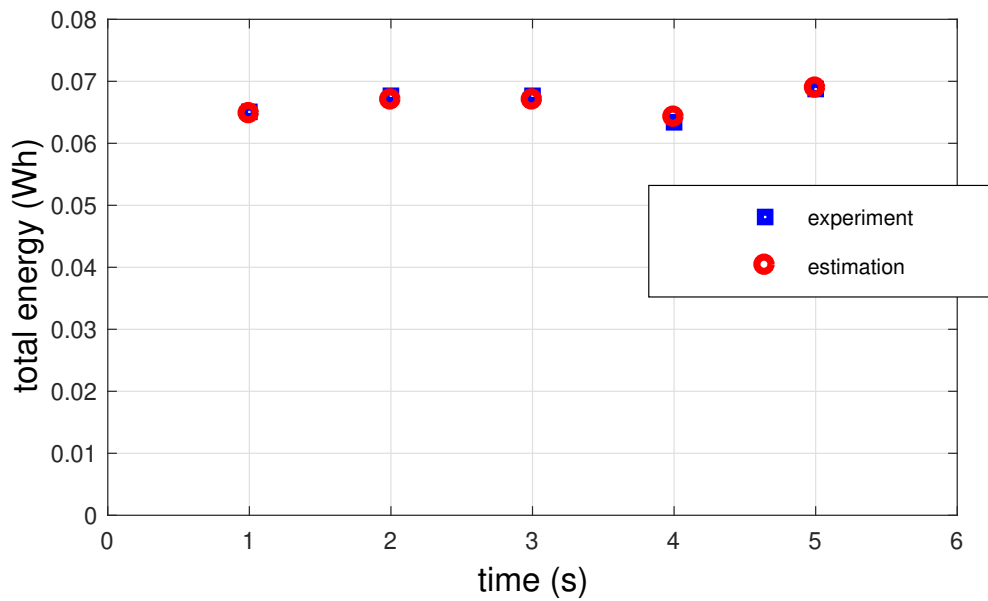
Figure 2.7: Total energy consumed by a motor in hovering motion from measurements and estimated calculation in five time experiment tests

compared the estimation of R_j by using Eq. (2.23). One experiment measured the power consumed by the motor. The second consisted of five repetitions of an experiment measuring the total energy of a quadcopter via a summation of all measured power consumption during the motion. Figures 2.6 and 2.7 show that the estimation result was similar to the measured power. Therefore, the value of resistance R_j can be used to estimate power and total energy consumption by using a motor in a testbed and by assuming that all motors are identical.

2.2.3 Experimental Testbed Parameters

Tables 2.1 and 2.2 show the components and parameters of the experimental quadcopter testbed.

Table 2.1: Components in experimental testbed configuration

Component	Type	Manufacturer
4 rotor helicopter	DRAGANFLYER IV	RCTOYS
AD converter board	ADA16-8/2(CB)L	Contec
DA converter board	DAI16-4(USB)	Contec
Potentiometer	JC22fi1k	Copal Electronics
DC motor	RC-280SA-2485	Mabuchi Motor Co., Ltd.
Motor driver	ADS50-5	Maxon Motor
Power supply	PUP5-2	Takasago
Power supply	HWS100-12/A	$Densei - \lambda$
PC(OS)	Core i5 3rd Gen (Windows 10 64 bit)	Panasonic(Microsoft)

Table 2.2: Parameter of quadcopter experimental testbed

Symbol	Parameter	Value (unit)
m	mass of quadcopter testbed	0.285(kg)
L	distance of rotor to the quadcopter center of gravity	0.212(m)
g	gravitational acceleration	9.807 (m/s^2)
d	force to moment scaling factor	1(m)
I_x	moment of inertia about x axis in body frame	5.136×10^{-3} (kg.m^2)
I_y	moment of inertia about y axis in body frame	5.136×10^{-3} (kg.m^2)
I_z	moment of inertia about z axis in body frame	1.016×10^{-2} (kg.m^2)

Chapter 3

Closed-Loop Configuration and Velocity Estimation

3.1 Introduction

In the previous chapter, we derived the dynamics of a quadcopter with four independent inputs with 6-DOFs and categorized the system as underactuated. It is worth mentioning that it is not easy to develop the strategy that controls all motions via the four original inputs of such a system. Thus, for simplicity, we used a virtual/synthetic input to easily transform the dynamics of the quadcopter into a simple decoupled linear form and then proceeded to design the control strategy with this virtual input. In developing a closed-loop control structure via virtual input consideration, we could solve the problem of overestimation in both the translation input and rotational input of the quadcopter by using the least squares method [49, 93] and a simple dynamic inversion, respectively.

The position and attitude states of the quadcopter were provided and measured only at each sampling time from the sensors in the quadcopter experimental testbed. On the contrary, we used a reduced-order observer [29] to estimate the velocity states of the controller from a continuous-time

dynamics model by considering a discrete-time control system. Therefore, the observer could also be applied to the testbed. For this case, we applied SMC in both translational and rotational motion controls to verify the effectiveness of the method experimentally and reflect the advantages of SMC as a robust controller in all DOFs.

3.2   Quadcopter Dynamics

To simplify the controller design for an underactuated quadcopter system, where the number of DOF exceeds the input number, we transformed the original underactuated dynamics described in Eq. (2.18) into a decoupled system [93]. Given a synthetic input $v = \bar{f}_1(\Theta, \dot{\Theta}) + \bar{f}_2(\Theta, u)$, the decoupled system in Eq. (2.18) is written in the following simple linear form:

$$
\begin{aligned}
\dot{\xi}_1 &= \xi_2 \\
\dot{\xi}_2 &= v
\end{aligned}
\tag{3.1}
$$

where $\xi_1 = \xi = [x, y, z, \phi, \theta, \psi]$ and $\xi_2 = \dot{\xi}$, $v = [v_x, v_y, v_z, v_\phi, v_\theta, v_\psi]^T$ is a new controller-design input vector that enables us to consider a fully actuated system.

Given the aerodynamics and gyroscopic effects, along with wind effects as disturbance, we could rewrite the decoupled dynamics of a quadcopter as follows:

$$
\begin{aligned}
\dot{\xi}_1 &= \xi_2 \\
\dot{\xi}_2 &= v + \rho_d \\
y_1(k) &= \xi_1(k)
\end{aligned}
\tag{3.2}
$$

where ξ_1 is the position, ξ_2 is the velocity, v is the synthetic input, and ρ_d is the disturbance vector.

3.3 Observer-Based Output Sliding-Mode Controller

3.3.1 Control Structure
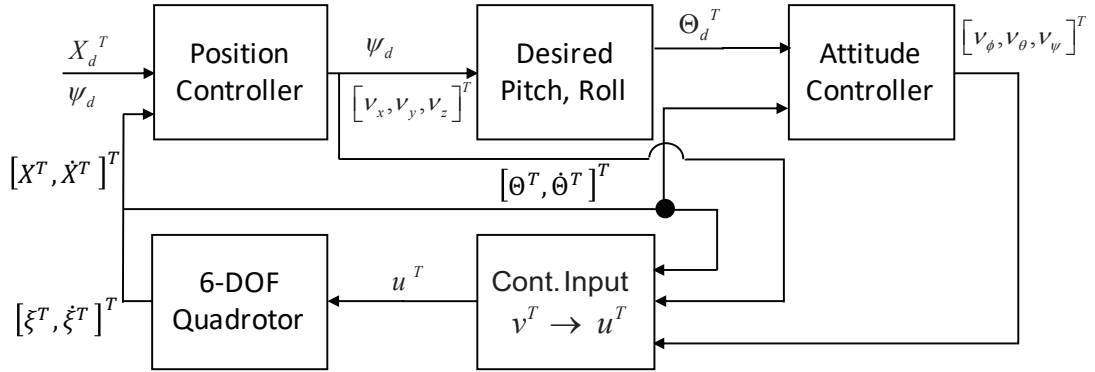
Figure 3.1: Control System Structure

For the quadcopter to fly in an autonomous system, we chose the desired output as the absolute position $X_d = [x_d, y_d, z_d]^T$, and yaw angle ψ_d. In this configuration, we divided the control structure into two parts, namely, a translational controller for the absolute position tracking and a rotational controller for attitude tracking.

From the new definition of the virtual input vector in Eq. (4.2), we obtained two sets of translation and rotational dynamics equations. For translational dynamics, we have

$$v_x = (\sin\theta\cos\psi + \sin\phi\cos\theta\sin\psi)\frac{u_1}{m}$$

$$v_y = (\sin\theta\sin\psi - \sin\phi\cos\theta\cos\psi)\frac{u_1}{m} \tag{3.3}$$

$$v_z = \cos\phi\cos\theta\frac{u_1}{m} - g$$

For rotational dynamics, we have

$$[v_\phi, v_\theta, v_\psi]^T = J^{-1}\left([u_2, u_3, u_4]^T + [K_1, K_2, K_3]^T\right) \tag{3.4}$$

By varying the attitude variables into the desired attitude variables in Eq. (3.3), we could calculate the desired pitch and roll angles in Eq. (3.5).

$$\phi_d = \arctan\left(\frac{v_x \sin\psi_d - v_y \cos\psi_d}{v_z + g}\right) \tag{3.5}$$

$$\theta_d =$$

$$\arctan\left(\frac{v_x \cos\psi_d + v_y \sin\psi_d}{\sqrt{(v_x \sin\psi_d - v_y \cos\psi_d)^2 + (v_z + g)^2}}\right)$$

To obtain the original inputs (u_1, u_2, u_3, and u_4) in Eq. (2.18), we utilized the method presented in [49]. We obtained input u_1 from Eqs. (4.2) and (3.3) as follows :

$$u_1 = m\sqrt{v_x^2 + v_y^2 + (v_z + g)^2} \tag{3.6}$$

For input u_2, u_3, and u_4 we exploited a simple dynamics inversion from Eq. (3.4); thus, we obtained the following:

$$[u_2, u_3, u_4]^T = J[v_\phi, v_\theta, v_\psi]^T - [K_1, K_2, K_3]^T \tag{3.7}$$

Fig. 3.1 summarizes and describes the above control strategy as follows:

- (Step 1) The desired trajectory of $X_d = [x_d, y_d, z_d]^T$, and yaw angle ψ_d were assigned to the position controller, which computes the virtual control input $[v_x, v_z, v_y]^T$ from the tracking errors between the current positional states X and their desired trajectories X_d. This step provides the desired trajectory of roll angle ϕ_d and pitch angle θ_d, and ψ_d remains as assigned.

- (Step 2) The attitude controller which is explained in the succeeding

section, handled the attitude tracking error between the current angular states Θ and their desired trajectories Θ_d, and subsequently provided the virtual control inputs $[v_\phi, v_\theta, v_\psi]^T$.

- (Step 3) The virtual input vector $v = [v_x, v_y, v_z, v_\phi, v_\theta, v_\psi]^T$ was transformed into the real vector $u = [u_1, u_2, u_3, u_4]^T$ with Eqs. (3.6) and (3.7).

3.3.2 Controller Design

A stable sliding surface is determined in an SMC design, and the robust control strategy is designed to force the system onto the sliding surface. Controller stabilization and tracking based on the SMC strategy is designed for the dynamics in Eq. (3.2). The sliding-surface equation in Eq. (3.2) is designed as follows [65]:

$$s = \dot{\varepsilon} + \lambda_s \varepsilon \tag{3.8}$$

where ε and $\dot{\varepsilon}$ are the tracking errors of the ξ_1 and ξ_2, positions and velocities, to desired trajectories $\xi_d = [x_d, y_d, z_d, \phi_d, \theta_d, \psi_d]^T$ and $\dot{\xi}_d = [\dot{x}_d, \dot{y}_d, \dot{z}_d, \dot{\phi}_d, \dot{\theta}_d, \dot{\psi}_d]^T$, respectively; $\lambda_s = \text{diag}\{\lambda_{si}\}$. i=1,2,...,6, is a matrix with positive diagonal elements, and $s = 0$; $s = [s_1, s_2, \cdots, s_6]^T$ is a sliding surface.

To improve tracking performance, an integral part was added to Eq. (3.8) to yield the following sliding-surface equation [77]:

$$s = \dot{\varepsilon} + \lambda_s \varepsilon + \alpha \int_0^t \varepsilon(\tau)\mathrm{d}\tau \tag{3.9}$$

where $\alpha = \text{diag}\{\alpha_i\}$, i=1,2,...,6, is a matrix with positive diagonal elements.

The control objective here is to force the system into the sliding-mode $s = 0$. Once the system reaches the sliding surface, the controller

maintains this sliding-mode condition, robustness is provided, and error tracking converges exponentially to zero.

Considering the sliding surface in Eq. (3.8), we could write the control system dynamics as follows:

$$\dot{s} = \ddot{\varepsilon} + \lambda_s \dot{\varepsilon} \tag{3.10}$$

By substituting $\ddot{\varepsilon} = \ddot{\xi}_d - \dot{\xi}_2$ and Eq. (3.2) into Eq. (3.10) gives

$$\dot{s} = \ddot{\xi}_d - v - \rho_d + \lambda_s \dot{\varepsilon} \tag{3.11}$$

where $\ddot{\xi}_d$ is the desired acceleration.

To achieve condition $s = 0$, we considered the synthetic control input v with a constant and a proportional rate reaching law as follows:

$$v = \hat{u} + ks + q\mathrm{sign}(s) \tag{3.12}$$

where $k = \mathrm{diag}\{k_i\}$ and $q = \mathrm{diag}\{q_i\}$ are positive diagonal elements, and $\mathrm{sign}(.)$ is a signum function defined as follows:

$$\mathbf{sign}(s) \quad = \quad \begin{cases} 1 & \text{if } s > 0 \\ 0 & \text{if } s = 0 \\ -1 & \text{if } s < 0 \end{cases}$$

$\hat{u}$ is equivalent control input for dynamics in Eq. (3.11) :

$$\hat{u} = \ddot{\xi}_d + \lambda_s \dot{\varepsilon} \tag{3.13}$$

Taking the integral sliding-surface equation in Eq. (3.9) into consideration,

equivalent control input $\hat{u}$ is as follows:

$$\hat{u} = \ddot{\xi}_d + \lambda_s \dot{\epsilon} + \alpha \varepsilon \tag{3.14}$$

3.3.3 Stability Analysis

3.3.3.1 Sliding-Mode Controller

In order to have to analyze the stability of the controller in Eq. (3.13) then we should consider the quadcopter have six motion that can be controlled independently. The Lyapunov function candidate is given for each DOF as follows:

$$V_i = \frac{1}{2} s_i^2 \tag{3.15}$$

The first derivative Eq. (3.15) using Eq. (3.10) can be obtained as follows:

$$\dot{V}_i = s_i(-k_i s_i - q_i \text{sign}(s_i) - \rho_{di}) \tag{3.16}$$

where k_i and q_i are the elements from diagonal matrix of k and q respectively, and ρ_{di} is element from diagonal matrix ρ_d. Assume that there is positive value D_i bounded of ρ_{di} where

$$|\rho_{di}| < D_i \tag{3.17}$$

then, we could obtain

$$\dot{V}_i < s_i(-k_i s_i - q_i \text{sign}(s_i) - D_i) \tag{3.18}$$

where the $k > 0$ and $q > D$, then $\dot{V}_i$ becomes negative definite. Therefore, the stability of the controller in Eq. (3.13) for each DOF is guaranteed and overall system is stable. Therefore, the sliding-mode condition in Eq . (3.8) can be converged to zero.

3.3.3.2   Sliding Surface

When sliding-mode condition $s = 0$, we could obtain the dynamics of sliding surface in Eq. (3.8) as follows:

$$\dot{\varepsilon}_i = -\lambda \varepsilon_i \tag{3.19}$$

To guarantee the stability of dynamics of the sliding surface in Eq. (3.8), we define the Lyapunov function candidate for each DOF as follows:

$$V_i = \frac{1}{2}\varepsilon_i^2 \tag{3.20}$$

The first derivative of Eq. (3.20) using Eq. (3.19), we obtain

$$\dot{V}_i = -\lambda_{si}\varepsilon_i^2 \tag{3.21}$$

where $\lambda_{si} > 0$ is selected and $\dot{V}_i$ becomes negative definite. Therefore, the stability of the sliding surface in Eq. (3.8) is guaranteed and ε_i converge to exponentially. To define the dynamics of integral sliding surface have a similar way in Eq. (3.9) when sliding-mode condition as follows:

$$\dot{\varepsilon}_i = -\lambda_{si}\varepsilon_i - \alpha_i \int_0^t \varepsilon_i(\tau)\mathrm{d}\tau \tag{3.22}$$

The dynamics of the sliding-mode in Eq. (3.22) can have the stability by Routh-Hurwitz criterion method. Selecting $\lambda_i > 0$ and $\alpha_i > 0$ will obtain a negative pole for the dynamics in Eq. (3.22) and its stability is guaranteed. Then ε_i converges to zero exponentially.

3.3.4   Reduced-Order Observer

The quadcopter is a second-order nonlinear system having position and velocity states, as shown in Eq.   (2.18).   We assume only position states, i.e., absolute position and attitude, at each sampling time to be measurable.   In Fig.   3.2, the velocity states are estimated by using a reduced-order observer [97] (see Appendix). This reduced-order observer has the advantage of being applicable to nonlinear sampled-data systems, including the quadcopter. To implement a controller on a digital computer, sampled data must be handled appropriately, even though most observers consider only continuous or linear discrete systems.

We consider the assumptions given in the Appendix for applying the reduced-order observer:

A1: Mappings f_1, f_2, and g_1 in Eq. (A.1) are smooth over compact domain of interest, $f_1(0) = 0$, and $f_2(0,0,0) = 0$.

A2: $m \times m$ matrix $\Phi(\cdot) = g_1(\cdot)^T g_1(\cdot)$, where g_1 is defined as shown in Eq. (A.1), is non-singular, and its inverse is bounded over the compact domain of interest.

Comparing Eqs.   (3.2) and (A.1), we have $f_1(\xi_1) = 0$, $g_1(\xi_1) = 1$, $f_2(\xi_1, \xi_2, u) = \bar{f}_1(\Theta, \dot{\Theta}) + \bar{f}_2(\Theta, u)$. Because $\bar{f}_1(\Theta, \dot{\Theta})$ in Eq. (3.2) includes the term mg, $f_2(\xi_1, \xi_2, u) = \bar{f}_1(\Theta, \dot{\Theta}) + \bar{f}_2(\Theta, u)$ does not satisfy assumption A1 if u is set to zero. We thus consider new control inputs v_x, v_y, and v_z in Eq. (3.1) as $u = [v_x, v_y, v_z, u_2, u_3, u_4]^T$ to cancel the term mg. We thus meet both assumptions A1 and A2 required to design the reduced-order observer as follows:

$$\hat{\xi}_2(k) = (I - TH)\hat{\xi}_2(k-1) + TN_T \qquad (3.23)$$

$k = 0, 1, 2, ...,$ T is a sampling instant, I is a 6×6 identity matrix, and H is
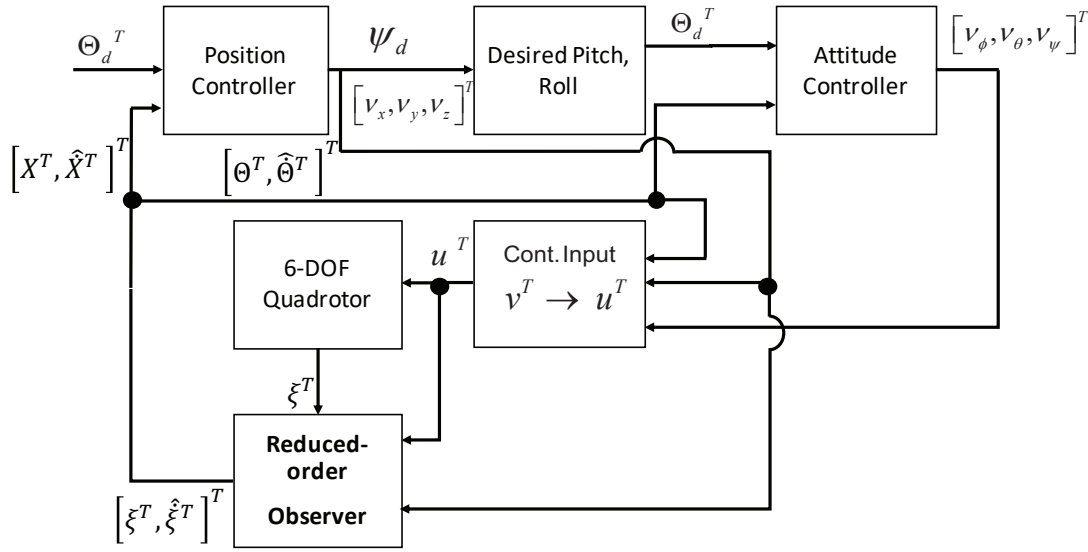
Figure 3.2: Reduced-order observer control structure of quadcopter.

a 6×6 diagonal matrix as explained in Appendix, and

$$
\begin{aligned}
N_T &= H\Psi_T + f_2(y_1(k-1), \Psi_T, u(k-1)), \\
\Psi_T &= \frac{y_1(k) - y_1(k-1)}{T}.
\end{aligned}
$$

Observed state $\hat{\xi}_2(k)$ is used in the closed loop controller design in Eq. (3.12).

3.4 Experimental Results

We present experimental results to demonstrate the effectiveness of our proposed method using the quadcopter test bed shown in Fig. 3.3 (a). This test bed was built by attaching four rotors to rigid links for conducting the same experiments multiple times to verify repeatability. Potentiometers (S_1-S_5) measure all positions and attitudes. The experimental test bed parameters are as follows: $m = 0.285$ kg, $L = 0.212$ m, $g = 9.807$ m/s^2, $d = 1$ m, $I_x = I_y = 5.136 \times 10^{-3}$ kg.m^2, and $I_z = 1.016 \times 10^{-2}$ kg.m^2.

The effectiveness of the reduced-order observer in Eq. (3.23) for estimating velocity is verified by comparing with the common practical method by

(a) (b)
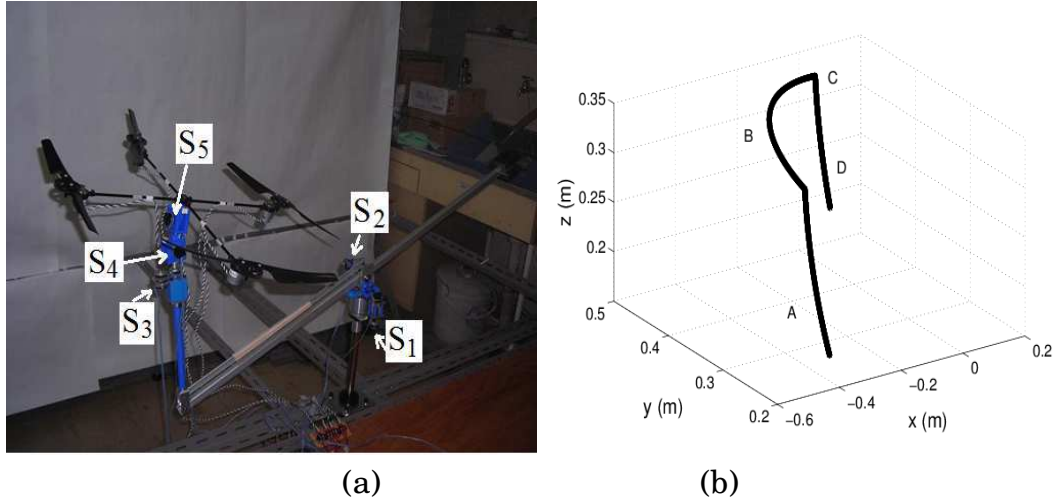
Figure 3.3: (a) Quadcopter test bed; (b) 3D-desired trajectory.

backward-difference method which considered the difference of current and previous position states. To calculate velocity based on the backward-difference method, we applied a second-order low-pass filter with cut-off frequency $\omega = 15$Hz to reduce high-frequency noise:

$$
\begin{aligned}
\hat{\xi}_2(k) &= \alpha[\hat{\dot{\xi}}_1(k) + 2\hat{\dot{\xi}}_1(k-1) + \hat{\dot{\xi}}_1(k-2)] \\
&\quad -2\beta\hat{\xi}_2(k-1) - \gamma\hat{\xi}_2(k-2) \quad (3.24) \\
\hat{\dot{\xi}}_1(k) &= \frac{\xi_1(k) - \xi_1(k-1)}{T} \quad (3.25) \\
\alpha &= \frac{(T\omega)^2}{(T\omega - 2)}\beta, \ \beta = \frac{T\omega - 2}{T\omega + 2}, \ \gamma = \beta^2 \quad (3.26)
\end{aligned}
$$

where $\hat{\dot{\xi}}_1(k)$ is the velocity signal estimated by the backward-difference method at the kth sampling instant. We obtained $\hat{\xi}_2(k)$ by using the second-order low-pass filter and used it for control.

We used these estimated velocities in the SMC in Eq. (3.12) by tuning the control parameters for both methods to achieve the best experimental results, obtained as follows:

The SMC with a reduced-ordered observer is expressed as follows:

k=diag(6.5,6,16,22,20,70),

λ=diag(3,4,9,8,7,40),

H=diag(90,90,100,50,60,50),

q=diag(0.6,0.6,1,0.8,0.8,1),

Moreover, the SMC with a backward-difference is expressed as follows:

k=diag(4,3,13,11,10,30),

λ=diag(3,4,9,8,7,40),

q=diag(0.6,0.6,1,0.8,0.8,1),

The desired trajectory (Fig. 3.3 [b]) consists of the following four different motions within 60 s :

A: Takeoff motion (0-10 s),

B: Maneuvering in the $x - y$ plane (10-15 s),

C: Hovering by performing a yaw motion (15-45 s),

D: Landing (45-60 s).

Figures 3.4 and 3.5 illustrate the superior efficiency of the reduced-order observer in decreasing high-frequency compared with the backward-difference method with a low-pass filter. The observer estimates reduced the root-mean-square error (RMSE) by 37.4% and the standard deviation (STD) of the velocity signal from the backward-difference method by 47.6% on the average (Tables 3.1-3.3). The observer estimated the states relatively quickly, i.e., within 25 ms, corresponding to the fifth sampling time, which is useful from a real-time application point-of-view.

Furthermore, applying the reduced-order observer enabled us to choose relatively higher SMC gains than by using the backward-difference method; therefore, the tracking performance is improved (Fig. 3.6), and a lower tracking error is depicted of the observer (Fig. 3.7). Nevertheless, the SMC with the sliding-surface function in Eq. (3.8) gave a relatively higher tracking error. Therefore, to improve the tracking performance, we designed an integral sliding surface in Eq. (3.9). After tuning, the

Table 3.1: RSME and variance of tracking error between backward-difference and reduced-order observer

Position	Backward-diff.		Reduced-order	
	Average of RSME	Average of variance	Average of RSME	Average of variance
x (cm)	5.321	4.124	2.449	2.389
y (cm)	2.259	2.285	1.669	1.445
z (cm)	1.745	0.977	1.881	0.901
ϕ (deg)	4.581	3.771	2.438	2.221
θ (deg)	4.442	2.703	2.252	1.375
ψ (deg)	1.683	1.051	1.314	0.882

experimental gain of the integral part became the following:

$$\alpha = \mathbf{diag}\{0.5, 0.5, 0.6, 0.4, 0.2, 0.6\}$$

Fig.   3.8 describes the effectiveness of this sliding-surface design. Therefore, the integral SMC reduced the RMSE from the SMC by 10.9% on average.

We verified the reliability of our proposed method by performing several experiments under the same condition. Fig. 3.9 summarizes the RMSE and STD for both methods and further indicates that the SMC with a reduced-order observer outperformed the backward-difference method. The latter method provided a variable performance in each trial, whereas the reduced-order observer yielded a steady result.

3.5   Conclusions

We presented a quadcopter velocity estimator based on the sampled data of position measurements and experimentally confirmed the effectiveness of the estimator on the basis of a reduced-order observer. Thereafter, we

Table 3.2: Variance of velocity between backward-difference and reduced-order observer

	Average of variance velocity	
	Backward-diff.	Reduced-order
x (m/s)	0.15934	0.08140
y (m/s)	0.13780	0.06857
z (m/s)	0.14869	0.05539
ϕ (rad/s)	0.65414	0.20022
θ (rad/s)	0.74347	0.23809
ψ (rad/s)	0.38966	0.60972

Table 3.3: Variance of control input between backward-difference and reduced-order observer

Control input	Average of variance control input	
	Backward-diff.	Reduced-order
u_1 (N)	0.212	0.181
u_2 (Nm)	0.140	0.127
u_3 (Nm)	0.129	0.128
u_4 (Nm)	0.184	0.179

designed an SMC for stabilizing and tracking the desired trajectory and compared its performance with that of a backward-difference method with a low-pass filter. In the experiments, the reduced-order observer estimated the velocity of the quadcopter from its initial value within 25 ms after the fifth sampling time; this result proved the suitability of the observer for practical applications. Furthermore, the observer enabled us to choose a relatively higher gain for the closed-loop controller, thus significantly reduced the tracking error. On average, the proposed method reduced the RMSE in tracking by 37.4% and reduced the STD of the velocity signal from the backward-difference method by 47.6%. Moreover, the integral SMC reduced the RMSE in tracking from the SMC by 10.9% on average. We confirmed the reliability of our proposed method via multiple experiments. Our future work would include position and attitude observations from acceleration and angular velocity signals that are typically obtained from an IMU.
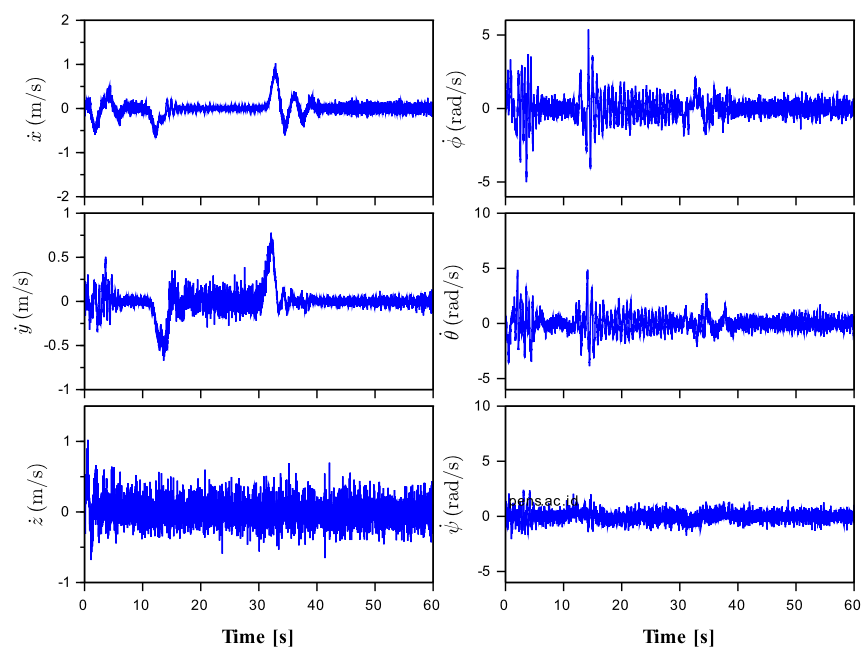
(a)
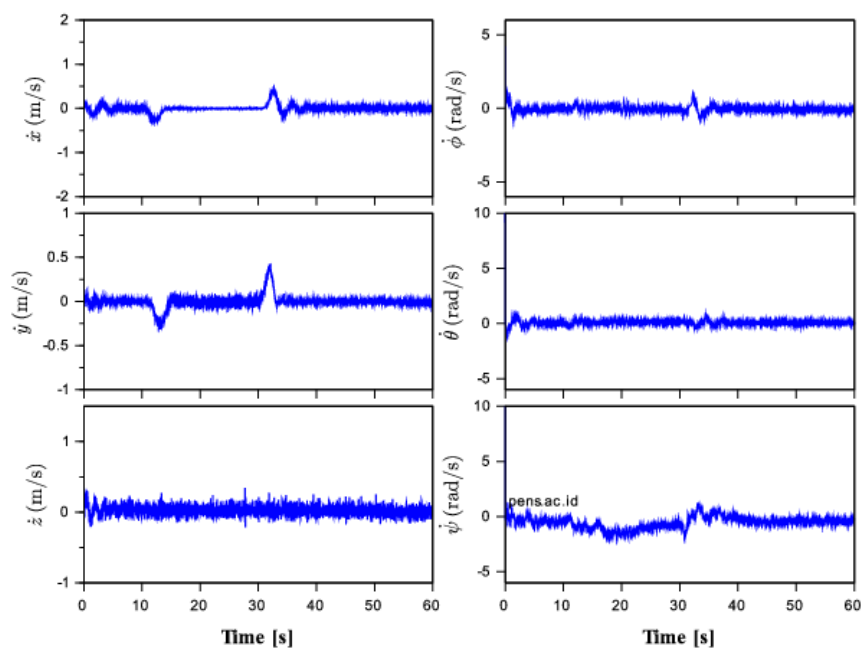
(b)

Figure 3.4: Velocity profiles obtained by (a) the backward-difference method and (b) the reduced-order observer.
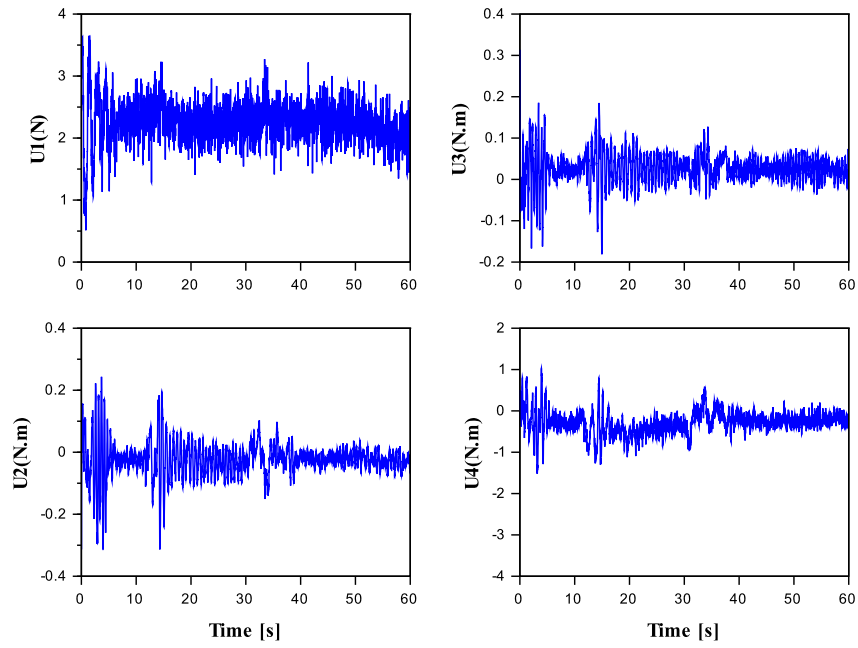
(a)
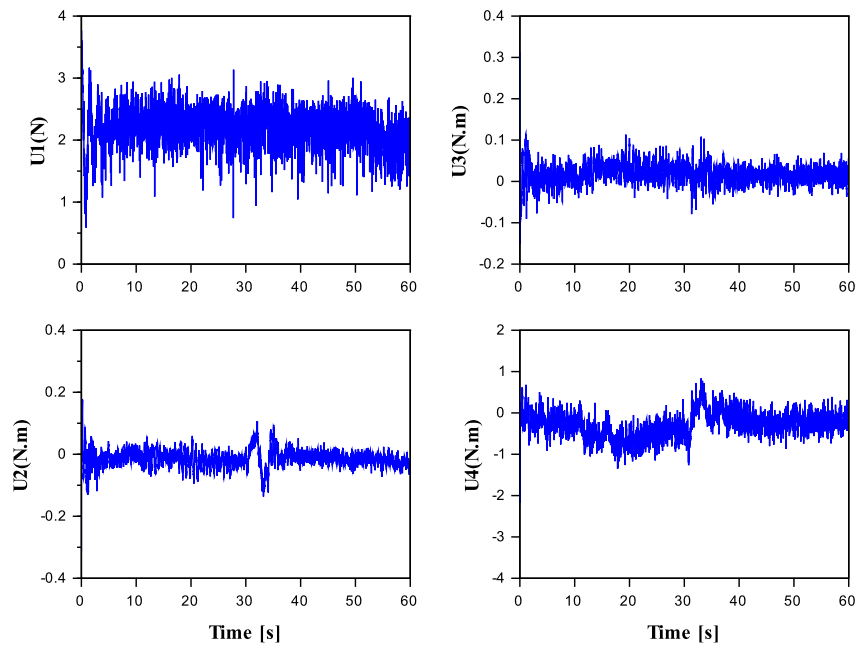
(b)

Figure 3.5: Control input profiles by (a) the backward-difference method and (b) the reduced-order observer
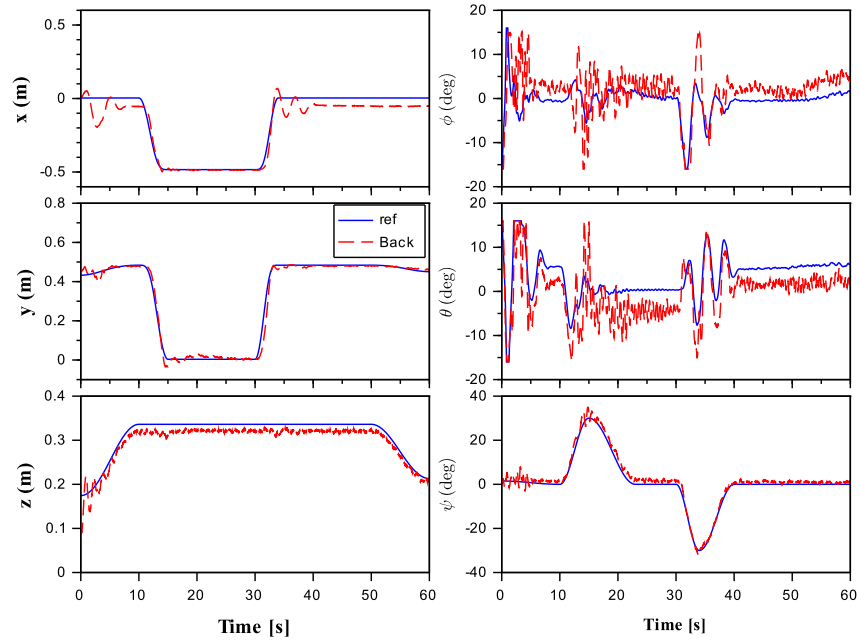
(a)
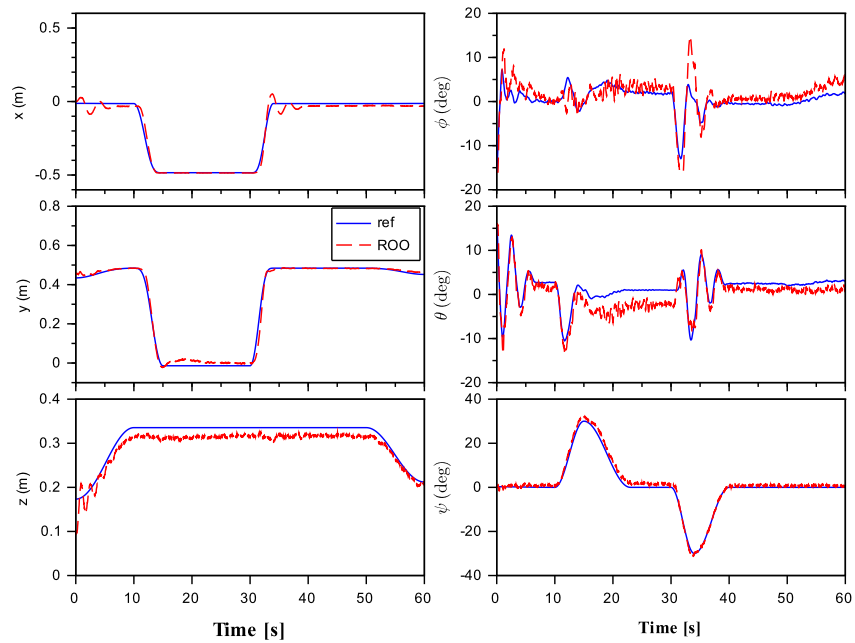
(b)

Figure 3.6: Tracking control results by (a) the backward-difference method, Back, and (b) the reduced-order observer , ROO
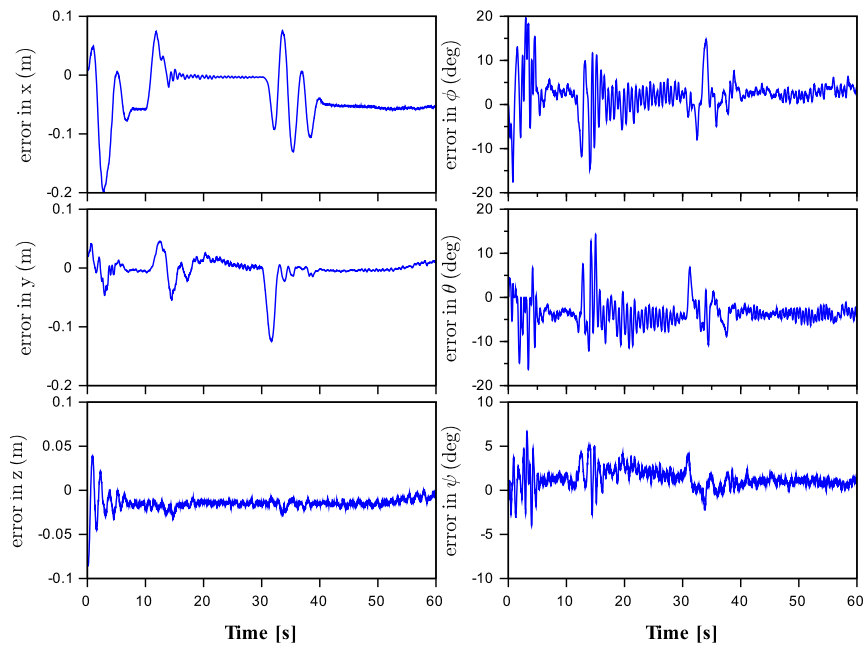
(a)
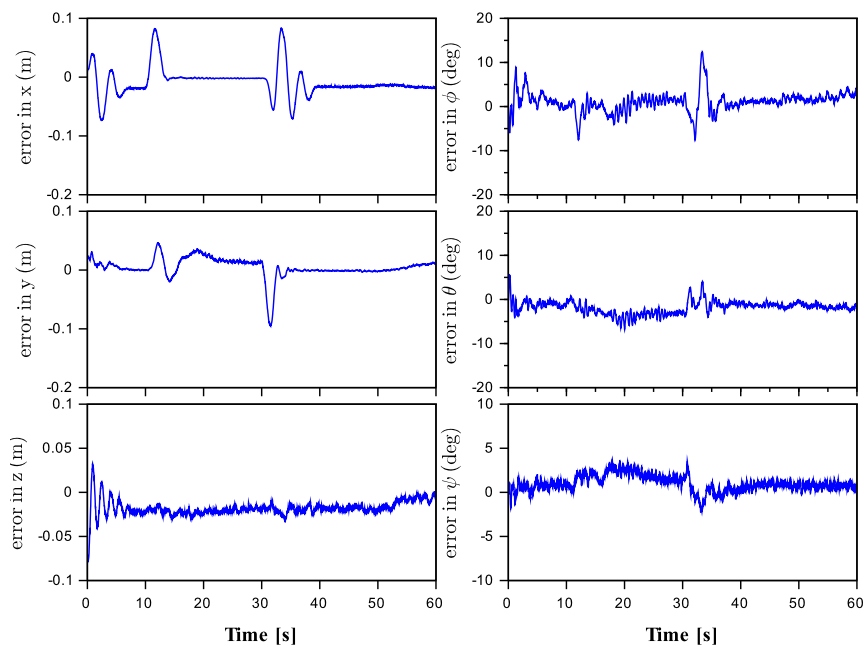
(b)

Figure 3.7: Tracking error results by (a) the backward-difference method and (b) the reduced-order observer tracking control results
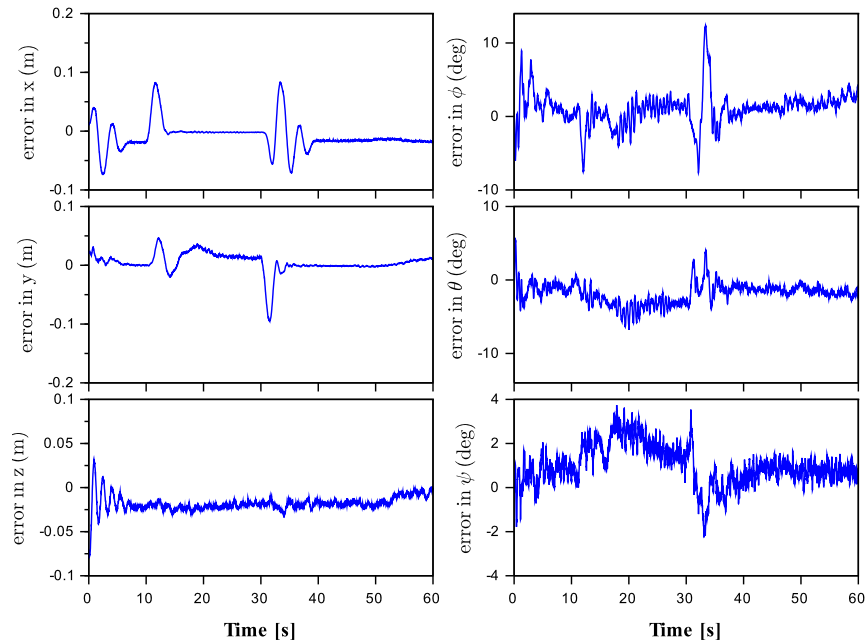
(a)
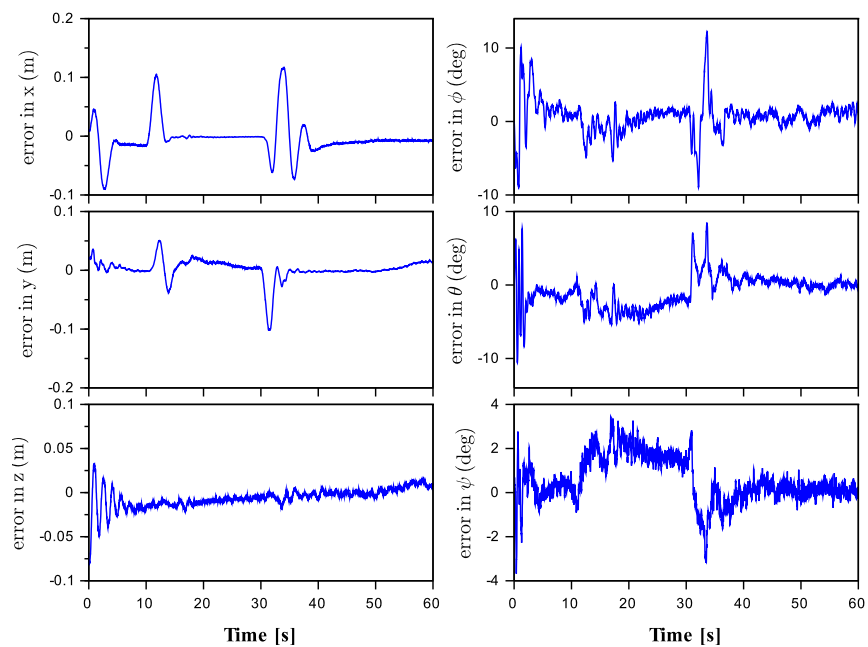
(b)

Figure 3.8: Tracking error results by (a) SMC and (b) integral SMC
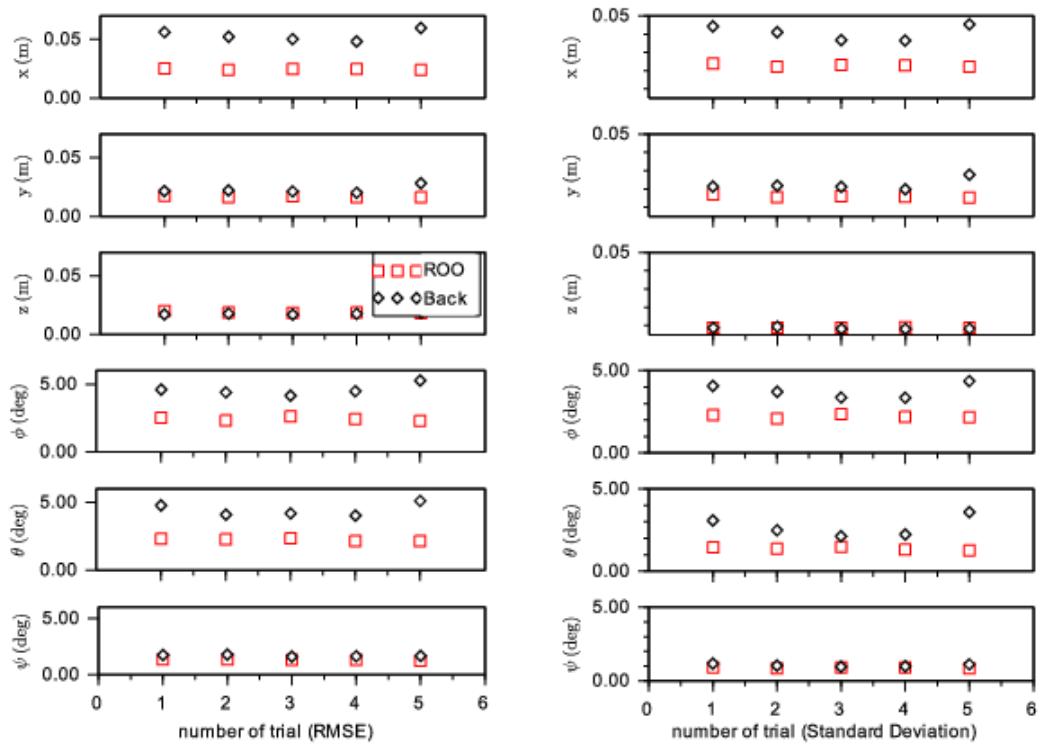
Figure 3.9: RMSE and standard deviation with the reduced-order observer, ROO, and the backward-difference method, Back, from five experiments

Chapter 4

Robust Trajectory Tracking and Energy Saving by Adaptive Modified Super-Twisting Control with a Nonlinear Sliding Surface

4.1   Introduction

Quadcopter UAVs have attracted research interest because of their wide range of applications, such as in navigation tasks (surveillance, mapping, rescuing, etc.) [58,98,99] and physical interactions (environment and object manipulation) [100, 101]. Nevertheless, the quadcopter requires robust control performance under aerodynamic forces, gyroscopic effects, altitude variations, wind payloads and resources, and limited operational time due to limited power supply capacity. In reality, quadcopter dynamics is a nonlinear and coupled system; therefore, it requires a robust controller to compensate the uncertainties and external disturbances and to consider

energy consumption. Most studies focused on reducing quadcopter energy consumption and discussed the design of the platform or mechanical parts of the quadcopter. Another approach suggests changing only the control algorithm on existing hardware, thus providing less cost and higher efficiency. This chapter addresses the effect of a robust control algorithm for energy saving.

A quadcopter has highly nonlinear and time-varying behavior owing to the constant influence of random disturbances. Conventional control approaches exploit feedback linearization [102], which obtains a linear decoupled closed-loop system after a change in coordinates in the state space. The requirement to measure all states for the feedback controller is the most important limitation and is vulnerable to parameter uncertainties. SMC is used to address model uncertainties [103]because it provides perturbation rejection by designing a boundary layer on the sliding-mode surface in the range of such uncertainties/perturbation [30]. However, in most practical cases, the estimation of the boundary can be extremely challenging and often lead to the overestimation of control, thus aggravating the chattering phenomenon, which potentially decreases the tracking performance and increases energy loss. To overcome this weakness, an adaptive SMC was introduced to stabilize the control system in altitude (and its motion) against the boundedness of uncertainties [98]. This algorithm aims to increase/decrease the gain to adapt the control magnitude to the perturbations and uncertainties in the sliding-mode condition. Furthermore, this algorithm forces the control gain to increase for continuous adaptation even when the condition is not in the sliding-mode. Thus, a backstepping and sliding-mode controller was developed via a simulation to control the position and attitude with an observer to identify the boundedness of the fault of the system [104].

Another technique known as the SOSMC was introduced for chattering

reduction [66, 103].   SOSMC keeps the main advantages of SMC and
improves control performance with respect to the chattering effects.
SOSMC generates continuous control that drives the sliding variable and
its derivative to zero in finite time. Among SOSMC, the Super Twisting
Algorithm (STA) is a well-known controller which ensures robustness with
respect to modeling errors and external disturbances because it contains
a discontinuous function under the integral term and can reduce the
chattering effect [58].   However, in practice, it is not easy to choose
appropriate parameters of the STA for good control performance because
the classical STA gain requires the bounds of the disturbance and its time
derivatives. ASTA improved this weakness without knowing the bounds
of the disturbance and unmodeled dynamics [74], whereas a modified
STA added a linear stabilizing term to provide faster convergence to the
sliding-mode condition and robustness from any initial condition [105].
Multivariable STA was applied with a NeuroFuzzy observer to estimate the
bounds of the uncertainty in the SMC of the attitude of quadcopter in the
simulation [106]. Nonetheless, all of these SMC methods are not conducted
in real-time applications and do not consider energy consumption.

The closed-loop dynamics in SMC [58] depends on the design of the
stable sliding surface. To improve the performance in SMC, a fuzzy system
strategy was utilized to update the parameters of a sliding surface [81], a
time-varying sliding surface was considered [83], and a variable damping
ratio of closed-loop dynamics was applied to reduce high overshoot [85].
However, these methods will increase the computation time.

Recent studies on disturbance rejection for a quadcopter have been
developed against wind gust in an outdoor environment. A controller
based on active disturbance rejection was introduced to observe the
presence of disturbance and maintain the position at a fix point [107].
Another approach used an adaptive observer with incremental nonlinear

dynamic inversion, to counter the wind gust disturbance by using a small quadcopter [108]. However, these methods are only verified in hovering motion and do not consider the energy consumption.

In this study, we propose a real time robust control algorithm and an NLSS [93] for a quadcopter for robust tracking control and energy saving. The robust control algorithm is inspired from the ASTA [94] and is based on adaptive SMOSC and a modified STA that has a robust behavior to model errors, uncertainties and perturbations with unknown bounds while having a dynamically adapted controller. Furthermore, it consists of the equivalent control part with a nonlinear function and an ASTA. On the contrary, the NLSS tracks error and is designed to reduce the energy consumption of quadcopter during the flight. We verify the effectiveness of the quadcopter via a simulation and an experiment. Furthermore, we show the control signals in order to verify the chattering reduction that relates to reduced energy consumption. To assess the reproducibility of the performance of the proposed controller and ensure the fair comparison with conventional controllers, we conduct repeated experiments in an indoor environment for a given artificial wind disturbance.

4.2   Control System Design

The control scheme for the quadcopter, which is a 6-DOF underactuated system with four control inputs, is discussed herein. The system dynamics is changed into a decoupled system by transforming the control inputs u to six new synthetic inputs v to obtain a linear form. Thereafter, input v is transformed into the original original control input u, desired attitude ϕ_d, and θ_d. To drive the system dynamics, we chose a combination of robust controller called the modified STA [94] with adaptation gain [74] and NLSS to attenuate the chattering phenomenon, increase tracking accuracy , and

avoid gain overestimation. The STA is based on an SOSMC, and the sliding
surface is designed with the nonlinear function.

Furthermore, the control of the pitch and roll angles are quite sensitive,
and the discontinuous control law could cause system instability. It can
further reduce the interest of using robust discontinuous control laws as
the first-order SMC. The second-order SMCr is an attractive approach
for avoiding discontinuity. The proposed controller adaptively limits the
magnitude of the control input and the chattering. Similarly, the STA
limits the essential discontinuous behavior of the control input, which does
not use the time derivative of the sliding variable as the standard SOSMC.

4.2.1   Control System Structure

To simplify our controller design, we transformed the system dynamics in
Eq. (2.18) into a decoupled system similar to that in [49] by considering the
virtual input

$$v = f + U \tag{4.1}$$

Hence, the decoupled system in Eq. (2.18), which considers Eq. (4.1), is
rewritten into a linear state form as follows :

$$\begin{aligned}
\dot{\xi}_1 &= \xi_2 \\
\dot{\xi}_2 &= v + \rho_d
\end{aligned} \tag{4.2}$$

where $\xi_1 = [x, y, z, \phi, \theta, \psi]^T$ is the positional vector, ξ_2 is the velocity vector,
$v = [v_x, v_y, v_z, \ v_\phi, v_\theta, v_\psi]^T$ is a new virtual control input vector, and ρ_d
is aerodynamics and gyroscopic effects together with wind effects and
uncertainty as a disturbance vector. Therefore, the virtual input v is
enabling us to consider a fully actuated system. The upper bound of $\|\rho_d\|$
is generally unknown; thus, an adaptive was considered in this study.

Furthermore, it was necessary to design a robust controller to compensate for the effects of uncertainties/perturbations. Therefore, the adaptive STA was applied as described in the next section.

4.2.2   Design of Nonlinear Sliding Surface

We applied SMC for the calculation of virtual inputs v and achieve a robust control performance. Here, an NLSS function was utilized to dynamically change the damping ratio of the closed-loop system in a range of initial (minimum) to final (maximum) values as the output form of the desired trajectory. The nonlinear sliding-surface equation for the dynamics in Eq. (4.2) is designed as follows [85]:

$$s_l = [F - \Psi \ I][e_1 \ e_2]^T \tag{4.3}$$

where $s_l = [s_{l1}, .., s_{l6}]^T$ is the sliding surface vector in all DOFs, $F = \text{diag} \{F_i\}$ and $\Psi = \text{diag} \{\Psi_i\}$ with $i = 1, 2, \ldots, 6$ are diagonal matrices with positive and nonpositive function diagonal elements, I is a 6×6 identity matrix, $e_1 = \xi_1 - \xi_{1d}$ and $e_2 = \xi_2 - \xi_{2d}$ are tracking error vectors with $\xi_{1d} = [x_d, y_d, z_d, \phi_d, \theta_d, \psi_d]^T$ and $\xi_{2d} = [\dot{x}_d, \dot{y}_d, \dot{z}_d, \dot{\phi}_d, \dot{\theta}_d, \dot{\psi}_d]^T$ are the desired trajectory vectors, respectively. Matrix Ψ consists of nonlinear functions as follows [93]:

$$\Psi_i = -\beta_i \left(\frac{1 - \exp(-1)}{\exp(\epsilon_i^2) - \exp(-1)} \right), \ \epsilon_i \in e_1 \tag{4.4}$$

where $\beta_i > 0$ to satisfy $\Psi_i < 0$. The stability of using the nonlinear sliding surface has been discussed and proved in [61] for $\beta_i \leq 3F_i$ $(F_i > 0)$. Moreover, 4.3.1 briefly shows the stability analysis.

The nonlinear function, Ψ_i, in Eq. (4.4) generates a varying time-constant for the NLSS as a function of error. It changes the time-constant

from a minimum value to a maximum value as the error magnitude
changes from zero to a high value. In principle, a system has a faster
response with a lower time-constant than with a higher time-constant,
but the lower time-constant requires more energy in a control system.
Therefore, in order to reduce the energy consumption with a relatively fast
response was considered by varying the time-constant [61].

To let the SMC law achieve $s_l = \dot{s}_l = 0$, we took the first derivative of
the sliding surface equation (Eq. (4.3)),

$$\dot{s}_l = \dot{e}_2 + (F - \Psi)\dot{e}_1 - \dot{\Psi}e_1 \tag{4.5}$$

From Eqs. (4.2) and (4.5) lead to

$$\dot{s}_l = v - \dot{\xi}_{2d} + (F - \Psi)\dot{e}_1 - \dot{\Psi}e_1 \tag{4.6}$$

Thereafter, we chose a control law v that consists of equivalent control v_{eq}
and the STA part v_{st},

$$v = v_{eq} + v_{st} \tag{4.7}$$

where

$$v_{eq} = -(F - \Psi)\dot{e}_1 + \dot{\Psi}e_1 + \dot{\xi}_{2d} \tag{4.8}$$

We assume that the desired accelerations of pitch and roll motions were
zero to avoid a second derivative calculation of Eq. (3.5).

4.2.3   Design of Adaptive Super-Twisting Control

We considered an STA that is an extension of previous control algorithm
[66], which contains a constant and a proportional and power-rate reaching
law, to include an extra linear correction term that ensures the finite-time
convergence of the sliding variable for a broader class of uncertainties, thus

leading to stronger robustness and faster convergence speed [109]. This STA has an important feature that is directly applicable to systems with a relative degree of one without measuring the derivative of the sliding variable $\dot{s}_{li}$. The controller in Eq. (4.7) was designed as follows:

$$v = v_{eq} + v_{st} = v_{eq} - k_a\Phi_1 - k_b \int \Phi_2 \mathrm{dt} \qquad (4.9)$$

where

$$\Phi_1 = s_l + k_c |s_l|^{\frac{1}{2}} \mathbf{sign}(s_l)$$

$$\Phi_2 = s_l + \frac{3}{2}k_c |s_l|^{\frac{1}{2}} \mathbf{sign}(s_l) + \frac{1}{2}k_c^2 \mathbf{sign}(s_l) \qquad (4.10)$$

are the nonlinear stabilizing terms and $|s_l|^{\frac{1}{2}} = \mathrm{diag}\left\{|s_{li}|^{\frac{1}{2}}\right\}$, $\mathbf{sign}(s_l)$ is the vector signum function, and $k_a = \mathrm{diag}\{k_{ai}\}$, $k_b = \mathrm{diag}\{k_{bi}\}$, and $k_c = \mathrm{diag}\{k_{ci}\}$ (i=1,2,..6), are diagonal matrices with positive diagonal elements.

Generally, the gains of k_a and k_b were selected with sufficiently high values by considering the upper bound of perturbation. Considering that the upper bound on ρ_{di} in Eq.(4.2) is unknown, we considered the adaptation of gains online for each DOF according to the law proposed in [74] for each DOF as follows:

$$\dot{k}_{ai} = \begin{cases} \bar{k}_i\sqrt{\dfrac{\gamma_i}{2}}\mathrm{sign}(|s_{li}| - \mu_i) & \text{if } k_{ai} > k_{mi} \\ \eta_i & \text{if } k_{ai} \leq k_{mi} \end{cases} \qquad (4.11)$$

$$k_{bi} = 2k_{di}k_{ai}$$

where $\bar{k}_i$, γ_i, η_i, k_{di}, and k_{mi} are all positive constants, and μ_i is a positive parameter that defines the boundary layer for the sliding-mode. Under a few assumptions in [74], the adaptive gain law in (4.11) achieves the finite-time convergence of sliding variable to a real two sliding-mode when

$|s_{li}| \leq \varpi_{1i}$ and $|\dot{s}_{li}| \leq \varpi_{2i}$, with $\varpi_{1i} \geq \mu_i$ and $\varpi_{2i} > 0$. In principle, ASTA aims to dynamically increase or decrease the control gains $k_{ai_\cdot}$ and $k_{bi_\cdot}$ until a second-order sliding-mode with respect to $\dot{s}$ is established. The gains then start to decrease. Alternately, this gain increases again to force the adaptation process again when the condition on $\dot{s}$ becomes lost (owing to an extremely small gain). When $|s_{li}| \leq \mu_i$, the ASTA reduces the control gains until the two sliding-mode is established; the gain increases once the sliding variable starts deviating from the two sliding mode.

The second line of the adaptation law ensurse that the gains are always positive. We may consider to tune k_{mi} as small as possible when only small uncertainties are necessarily considered.

The overall closed-loop dynamics is obtained by substituting Eq. (4.7) into Eq. (4.2) and by considering Eq. (4.3) as follows:

$$
\ddot{e}_1 + (F - \Psi + k_a)\dot{e}_1 + (k_a(F - \Psi) - \dot{\Psi})e_1 - \rho_d + k_a k_c |s_l|^{\frac{1}{2}} \operatorname{sign}(s_l)
$$

$$
+ k_b \int_0^t \left\{ \dot{e}_1 + (F - \Psi)e_1 + \frac{1}{2}k_c |s_l|^{\frac{1}{2}} \operatorname{sign}(s_l) + \frac{3}{2}k_c^2 \operatorname{sign}(s_l) \right\} dt = 0 \quad (4.12)
$$

4.3   Stability Analysis

4.3.1   Nonlinear Sliding Surface

By considering the sliding-mode condition $s_l = \dot{s}_l = 0$ and applying to Eqs. (4.3) and (4.5), we obtain the following equations

$$
\begin{cases}
\dot{e} = -(F - \Psi)e \\
\ddot{e} = \dot{\Psi}e - (F - \Psi)\dot{e}
\end{cases}
\quad (4.13)
$$

As F and Ψ are diagonal matrices, Eq. (4.13) can be confirmed in each DOF independently. We chose the Lyapunov function candidate for each

DOF as follows:

$$V_{1i} = 2\varepsilon_{\mathrm{i}}^2 + 2\dot{\varepsilon}_{\mathrm{i}}^2, \ \varepsilon_{\mathrm{i}} \in e \tag{4.14}$$

By considering Eqs. (4.4) and (4.13), we arrive at the first derivative of Eq. (4.14) as

$$\dot{V}_{1i} = \left\{(F_i - \Psi_{\mathrm{i}})^2 + 1 - \frac{2\Psi_i(F_i - \Psi_i)\varepsilon_i^2 \exp(\varepsilon_i^2)}{\exp(\varepsilon_i^2) - \exp(-1)}\right\} \times \left\{-(F_i - \Psi_{\mathrm{i}})\varepsilon_i^2\right\} \tag{4.15}$$

Then, we have $\dot{V}_{1i} \leq 0$, where $F_i > 0$ and $\Psi_i < 0$ with by choosing proper F_i and β_i in Eq. (4.4). Therefore, the stability in SMC in Eq. (4.13) is guaranteed.

4.3.2   Adaptive Super-Twisting

This subsection partially shows the stability of ASTA with reference to [74]. To establish the convergence of ASTA, we applied Eqs. (4.6)-(4.10) and obtained the sliding dynamics as follows:

$$\begin{aligned}\dot{s}_l &= -k_a\Phi_1 + c + \rho_d \\ \dot{c} &= -k_b\Phi_2\end{aligned} \tag{4.16}$$

where

$$\Phi_1 = s_l + k_c \left|s_l\right|^{\frac{1}{2}} \mathbf{sign}(s_l)$$

$$\Phi_2 = \Phi_1\Phi_3$$

$$\Phi_3 = \left(\frac{1}{2}k_c \left|s_l\right|^{-\frac{1}{2}} + I\right) \tag{4.17}$$

came from the definitions in Eq. (4.10). Considering that k_a, k_b and k_c are diagonal matrices, Eq. (4.16) can be decoupled into each DOF. Therefore, to analyze the stability of Eq. (4.16), we considered a Lyapunov function

candidate for each DOF (with $i = 1, .., 6$), as inspired by [74, 105],

$$V_{2i} = V_{sti} + V_{adi} = \left\{ q_i^T P_i q_i \right\} + \tag{4.18}$$

$$\left\{ \frac{1}{2\gamma_{ai}}(k_{ai} - k_{ai}^*)^2 + \frac{1}{2\gamma_{bi}}(k_{bi} - k_{bi}^*)^2 \right\}$$

$$q_i = \begin{bmatrix} q_{1i} \\ q_{2i} \end{bmatrix} = \begin{bmatrix} \Phi_{1i}(s_{li}) \\ c_i \end{bmatrix}, \tag{4.19}$$

$$P_i = \begin{bmatrix} \lambda_i + 4k_{di}^2 & -2k_{di} \\ -2k_{di} & 1 \end{bmatrix} \tag{4.20}$$

where $k_{ai}^* > 0$ and $k_{bi}^* > 0$ are the expected values of k_{ai} and k_{bi}, γ_{ai} and γ_{bi} are positive constants, and $\lambda_i > 0$ and $k_{di} > 0$. By considering Eq. (4.16), we determine the first derivative of q_i

$$\dot{q}_i = \begin{bmatrix} \dot{\Phi}_{1i}\dot{s}_{li} \\ \dot{c}_i \end{bmatrix} = \begin{bmatrix} \Phi_{3i}(-k_{ai}\Phi_{1i} + c_i) \\ -k_{bi}\Phi_{3i}\Phi_{1i} \end{bmatrix}$$

$$= \begin{bmatrix} -k_{ai} & 1 \\ -k_{bi} & 0 \end{bmatrix} \Phi_{3i} \begin{bmatrix} \Phi_{1i} \\ c \end{bmatrix} = A_i \tilde{q}_i \tag{4.21}$$

$$\tilde{q}_i = \Phi_{3i} q_i$$

The first derivative of the first term V_{sti} using Eq. (4.21) was as follows:

$$\begin{aligned} \dot{V}_{sti} &= q_i^T P_i \dot{q}_i + \dot{q}_i^T P_i q_i \\ &= q_i^T P_i A_i \tilde{q}_i + \tilde{q}_i^T A_i^T P_i q_i \\ &= q_i^T (P_i A_i + A_i^T P_i) \tilde{q}_i = -q_i^T Q_i \tilde{q}_i \end{aligned} \tag{4.22}$$

where Q_i is a positive definite symmetric matrix with

$$
\begin{aligned}
Q_i &= \begin{bmatrix} Q_{1i} & Q_{2i} \\ Q_{2i} & 4k_{di} \end{bmatrix} \\
Q_{1i} &= 2k_{ai}(\lambda_i + 4k_{di}^2) - 4k_{di}k_{bi}, \\
Q_{2i} &= (k_{bi} - 2k_{di}k_{ai}) - (\lambda_i + 4k_{di}^2)
\end{aligned}
\tag{4.23}
$$

To guarantee the positive definiteness of matrix Q_i, we chose

$$
k_{bi} = 2k_{di}k_{ai} \tag{4.24}
$$

and considered Eq. (4.24) and the Schur complement with $Q_{1i} - Q_{2i}^T(4k_{di})^{-1}Q_{2i} > 0$; thus, we obtain

$$
k_{ai} > \frac{(\lambda_i + 4k_{di}^2)^2}{8\lambda k_{di}}. \tag{4.25}
$$

The standard inequality for the quadratic form considering Eqs. (4.18)-(4.22),

$$
\lambda_{\min}(P_i)\|q_i\|_2^2 \le q_i^T P_i q_i \le \lambda_{\max}(P_i)\|q_i\|_2^2 \tag{4.26}
$$

$$
\lambda_{\min}(Q_i)\Phi_{3i}\|q_i\|_2^2 \le q_i^T Q_i \Phi_{3i} q_i \tag{4.27}
$$

$$
q_i^T Q_i \Phi_{3i} q_i \le \lambda_{\max}(Q_i)\Phi_{3i}\|q_i\|_2^2 \tag{4.28}
$$

where $\lambda_{\min}(\cdot)$ and $\lambda_{\max}(\cdot)$ are minimum and maximum eigenvalue of $(\cdot)$, respectively, and

$$
\begin{aligned}
\|q_i\|^2 &= q_{1i}^2 + q_{2i}^2 = \Phi_{1i}^2 + c_i^2 \\
&= s_{li}^2 + k_{ci}^2|s_{li}| + k_{ci}|s_{li}|^{\frac{3}{2}} + c_i^2 \ge |s_{li}|
\end{aligned}
\tag{4.29}
$$

is Euclidean norm of q_i. By considering Eqs. (4.19), (4.26) and (4.29), we

obtained the inequality

$$|s_{li}|^{\frac{1}{2}} \leq \|q_i\| \leq \frac{V_{sti}^{\frac{1}{2}}}{\lambda_{\min}^{\frac{1}{2}}(P_i)} \tag{4.30}$$

Furthermore, by applying Eqs. (4.17), (4.22), (4.26), (4.27) and (4.30), we
have the inequality,

$$\begin{aligned}
\dot{V}_{sti} = & - q_i^T Q_i \tilde{q}_i \leq -\lambda_{\min}(Q_i)\Phi_{3i} \|q_i\|_2^2 \\
\leq & - \lambda_{\min}(Q_i) \left(\frac{1}{2}k_{ci} |s_{li}|^{-\frac{1}{2}} + 1\right) \|q_i\|_2^2 \\
\leq & - \lambda_{\min}(Q_i) \left(\frac{1}{2}k_{ci}\lambda_{\min}^{\frac{1}{2}}(P_i)V_{sti}^{-\frac{1}{2}} + 1\right) V_{sti}\lambda_{\max}^{-1}(P_i) \\
\leq & - r_{1i}V_{sti}^{\frac{1}{2}} - r_{2i}V_{sti}
\end{aligned} \tag{4.31}$$

where

$$\begin{aligned}
r_{1i} &= \frac{k_{ci}.\lambda_{\min}(Q_i)\lambda_{\min}^{1/2}(P_i)}{2\lambda_{\max}(P_i)} \\
r_{2i} &= \frac{\lambda_{\min}(Q_i)}{\lambda_{\max}(P_i)}
\end{aligned} \tag{4.32}$$

In view of Eq. (4.18), we assumed the condition $\gamma_{k_a i} = k_{ai} - k_{ai}^* < 0$ and
$\gamma_{k_b i} = k_{bi} - k_{bi}^* < 0$ as in [74]. Thereafter, we could write the derivative of the
Lyapunov function candidate V_{2i} in Eq. (4.18) with Eq. (4.31) as follows:

$$\dot{V}_{2i} \leq \quad -r_{1i}V_{sti}^{1/2} - r_{2i}V_{sti} - \frac{1}{\gamma_{ai}} |\gamma_{k_a i}| \dot{k}_{ai} - \frac{1}{\gamma_{bi}} |\gamma_{k_b i}| \dot{k}_{bi} \tag{4.33}$$

Eq. (4.33) could be extended as follows:

$$
\begin{aligned}
\dot{V}_{2i} \leq\; & -r_{1i}V_{sti}^{1/2} - r_{2i}V_{sti} - \frac{1}{\gamma_{ai}}\,|\gamma_{k_a i}|\,\dot{k}_{ai} \\
& -\frac{1}{\gamma_{bi}}\,|\gamma_{k_b i}|\,\dot{k}_{bi} + \frac{\bar{k}_{ai}}{\sqrt{2\gamma_{ai}}}\,|\gamma_{k_a i}| - \frac{\bar{k}_{ai}}{\sqrt{2\gamma_{ai}}}\,|\gamma_{k_a i}| \\
& +\frac{\bar{k}_{bi}}{\sqrt{2\gamma_{bi}}}\,|\gamma_{k_b i}| - \frac{\bar{k}_{bi}}{\sqrt{2\gamma_{bi}}}\,|\gamma_{k_b i}|
\end{aligned}
\tag{4.34}
$$

where $\bar{k}_{ai}$ and $\bar{k}_{bi}$ are positive constants. We applied the well-known inequality $(x^2 + y^2 + z^2)^{1/2} \leq |x| + |y| + |z|$ by considering Eq. (4.18) to obtain the inequality

$$
-r_3 V_{2i}^{1/2} \geq -r_{1i}V_{sti}^{1/2} - \frac{\bar{k}_{ai}}{\sqrt{2\gamma_{ai}}}\,|\gamma_{k_a i}| - \frac{\bar{k}_{bi}}{\sqrt{2\gamma_{bi}}}\,|\gamma_{k_b i}|
\tag{4.35}
$$

with $r_{3i} = \min(r_{1i}, \bar{k}_{ai}, \bar{k}_{bi})$. On the basis of (4.35), the function in Eq. (4.34) can be rewritten as follows:

$$
\dot{V}_{2i} \leq\;\; -r_{3i}V_{2i}^{1/2} - r_{2i}V_{sti} + \triangle_i
\tag{4.36}
$$

where

$$
\begin{aligned}
\triangle_i = & -|\gamma_{k_a i}|\left(\frac{1}{\gamma_{ai}}\dot{k}_{ai} - \frac{\bar{k}_{ai}}{\sqrt{2\gamma_{ai}}}\right) \\
& -|\gamma_{k_b i}|\left(\frac{1}{\gamma_{bi}}\dot{k}_{bi} - \frac{\bar{k}_{bi}}{\sqrt{2\gamma_{bi}}}\right)
\end{aligned}
\tag{4.37}
$$

To simplify $\triangle_i$ in Eq. (4.37), we chose $\dot{k}_{bi} = \bar{k}_{bi}\sqrt{\gamma_{bi}/2}$, to transform $\triangle_i$ as follows:

$$
\triangle_i = -|\gamma_{k_a i}|\left(\frac{1}{\gamma_{ai}}\dot{k}_{ai} - \frac{\bar{k}_{ai}}{\sqrt{2\gamma_{ai}}}\right)
\tag{4.38}
$$

If the condition $|s_{li}| > \mu_i$ and $k_{ai} > k_{mi}$ are satisfied in Eq. (4.11), we have

$$
\dot{k}_{ai} = \bar{k}_{ai}\sqrt{\frac{\gamma_{ai}}{2}}
\tag{4.39}
$$
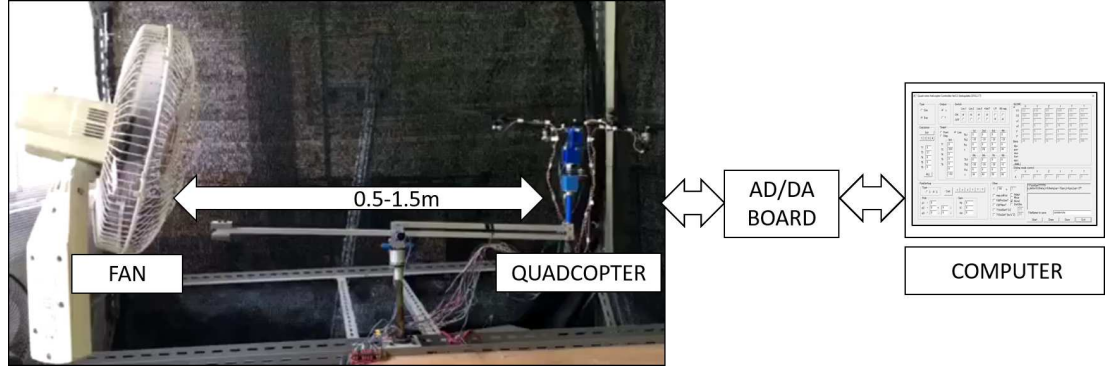
Figure 4.1: Experimental system configuration

With Eq. (4.39) into Eq. (4.38), $\triangle_i$ could be canceled; hence, Eq. (4.36) guarantees the stability. Proofs for stability under other conditions including the case $|s_{li}| \leq \mu_i$ are given in [74].

4.4   Implementation and Evaluation

We examined the effectiveness and robustness of the proposed controller design by comparing the results with STA and ASTA controllers in numerical and experimental tests with and without disturbance. Figure 4.1 shows the quadcopter testbed we used in the experiment. As earlier described, this testbed was designed to verify the repeatability of the results under the same experimental condition. The parameters in Eq. (2.18) for these numerical and experimental tests were obtained from a previous work [93] as follows: $m = 0.285$ kg, $L = 0.212$ m, $g = 9.807$ m/s^2, $d = 1$ m, $I_x = I_y = 5.136 \times 10^{-3}$ kg.m^2, and $I_z = 1.016 \times 10^{-2}$ kg.m^2. For the purpose of comparison, we assigned the linear sliding surface $s_l = \lambda e_1 + e_2$. Moreover, we designed the control input v_{eq} in Eq. (4.7) is designed as follows:

$$v_{eq} = -\lambda \dot{e}_1 + \dot{\xi}_{2d} \qquad (4.40)$$

λ is decomposed into F and β, where $\lambda = F + \beta$ and $\beta = \mathrm{diag}\{\beta_1, ..., \beta_6\}$ in **Eq.** (4.4).

The parameter design for ASTA and NSS is important. To the best of our knowledge, no systematic method of parameter selection for these methods has been discussed in existing literature. Herein, all values were selected by extensive trials. We allowed the STA and adaptive gains to start from a low-to-high value to bind the disturbance. Consequently, we adjusted the nonlinear function after obtaining the minimum number of linear sliding surfaces.

For the simulation, we employed the same trajectory as in our previous work [70] to verify the effectiveness of the proposed controller over the previous one, as well as its effectiveness to disturbance rejection. Moreover, as the trajectory in the simulation consisted of constant velocity motions, we developed a more practical trajectory of varying velocity motions in the experiment to further confirm the effectiveness of the controller.

4.4.1   Simulation Results

Under this section, the simulation results were evaluated to assess the performance of the controller at a sampling time of 0.005 s. Figure 4.2 illustrates the desired trajectory, which consists of four different motions for a total time of 60 s: (1) takeoff: from A to B (0–25 s) at a height of 0.1 m; (2) x–y plane maneuvers: from B to C (25–40s) at a height of 0.35 m; (3) yaw: from A to C (0–40 s); and 4) landing (40–60s): from C to D. The designed trajectory consisted of x–y–z simultaneous motions from 25–40 s, in which the robustness of the controller design may be evaluated under disturbances during this motion. We assumed a fixed disturbance, such as wind gust at approximately 4 m/s along the x- and y-axes, and a small error measurement in x–y–z.
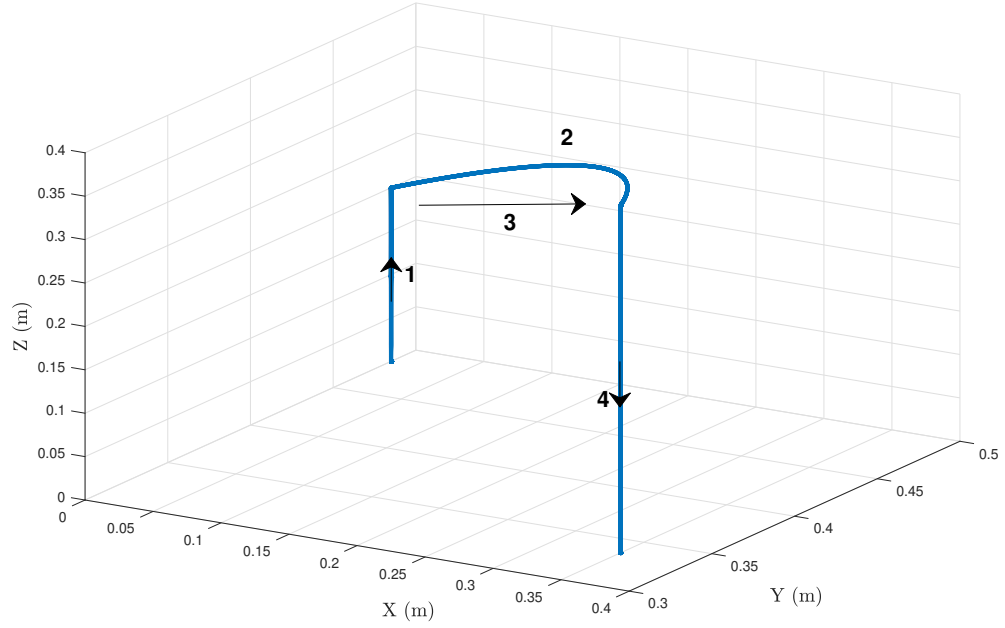
Figure 4.2: 3D desired trajectory in simulation

We performed the simulation with different parameters from the previous work [70] with disturbances consideration. For fair comparison, the same tuning parameters were chosen, including NSS parameters and the initial adaptation parameters (units are omitted) as follows: $k_a = $ **diag**$\{5, 5, 20, 8, 8, 15\}$, $k_b = $ **diag**$\{1, 1, 10\ 8, 1, 8\}$, and $k_c = $ **diag**$\{0.1,$ $0.1, 0.1, 0.1, 0.1, 0.1\}$. The NSS parameters were $F = $ **diag**$\{5, 10, 5, 5,$ $5\ 5\}$, and $\beta = $ **diag**$\{10, 10, 10, 10, 10, 10\}$. On the contrary, the tuning parameters for ASTA were: $\overline{k} = [2, 2, 10, 2, 2, 2$, $\gamma_i = 2$, $\mu_i = 0.01,$ $k_{mi} = 0.1$, $k_d = [1, 1, 3, 1, 1, 1]$, $i = 1, 2, ..6$, and $\eta = k_m$. To demonstrate the performance of the system in a realistic environment, we entered a static wind disturbance at 20–30 s and a time-varying disturbance that can be calculated as $\rho_d = [0.2, 0.2, 3, 1, 1, 1]^T \times \cos(t)$.

The ASTA with NSS (ASTAN) achieves a smaller tracking position error in Fig. 4.3, and reduced on average the mean and variance of the tracking position error by 33% without disturbance and 26.8% with disturbance. Figure 4.4 shows the control performances of these controllers. Control

Table 4.1: Tracking error comparison results in simulation

Condition	Controller	RMSE		STD	
		(cm)	(deg)	(cm)	(deg)
None	ASTAN	1.2×10^{-1}	6.74×10^{-2}	1.2×10^{-1}	6.74×10^{-2}
	ASTA	1.8×10^{-1}	5.85×10^{-2}	1.8×10^{-1}	5.01×10^{-2}
	STA	5.6×10^{-1}	7.8×10^{-2}	5.5×10^{-1}	7.8×10^{-2}
Dist.	ASTAN	7.1×10^{-1}	8.14×10^{-1}	7	8.14×10^{-1}
	ASTA	9.9×10^{-1}	5.7×10^{-1}	9.7	5.7×10^{-1}
	STA	3.6	1	35.9	1

Table 4.2: Control input variance comparison results in simulation

Controller	Variance	
	None	Disturbance
STA	4.48×10^{-2}	8.20×10^{-2}
ASTA	3.52×10^{-2}	5.87×10^{-2}
ASTAN	2.85×10^{-2}	5.32×10^{-2}

input u_1 generated a relatively high total, particularly at 0.2 s for the takeoff motion, thus implying that ASTAN has a faster initial takeoff under disturbance with a reduced overshoot. Figure 4.5 shows the dynamically changing control gains relative to the behavior of the tracking error without and with disturbance. Under disturbance, gains for pitch and roll showed different results after 20 s because significant tracking error changes in the x and y positions occurred and directly influenced ϕ_d and θ_d. Nevertheless, both adaptive methods detected this substantial error and tried to compensate them.

Table 4.1summarizes the RMSE and STD for all methods. Here, ASTAN outperformed ASTA. Moreover, the effectiveness of the adaptive mechanism for ASTAN was confirmed in both disturbance conditions. Table 4.2, summarizes the variances of the control input for these methods. Similarly, ASTAN effectively reduces system chattering.
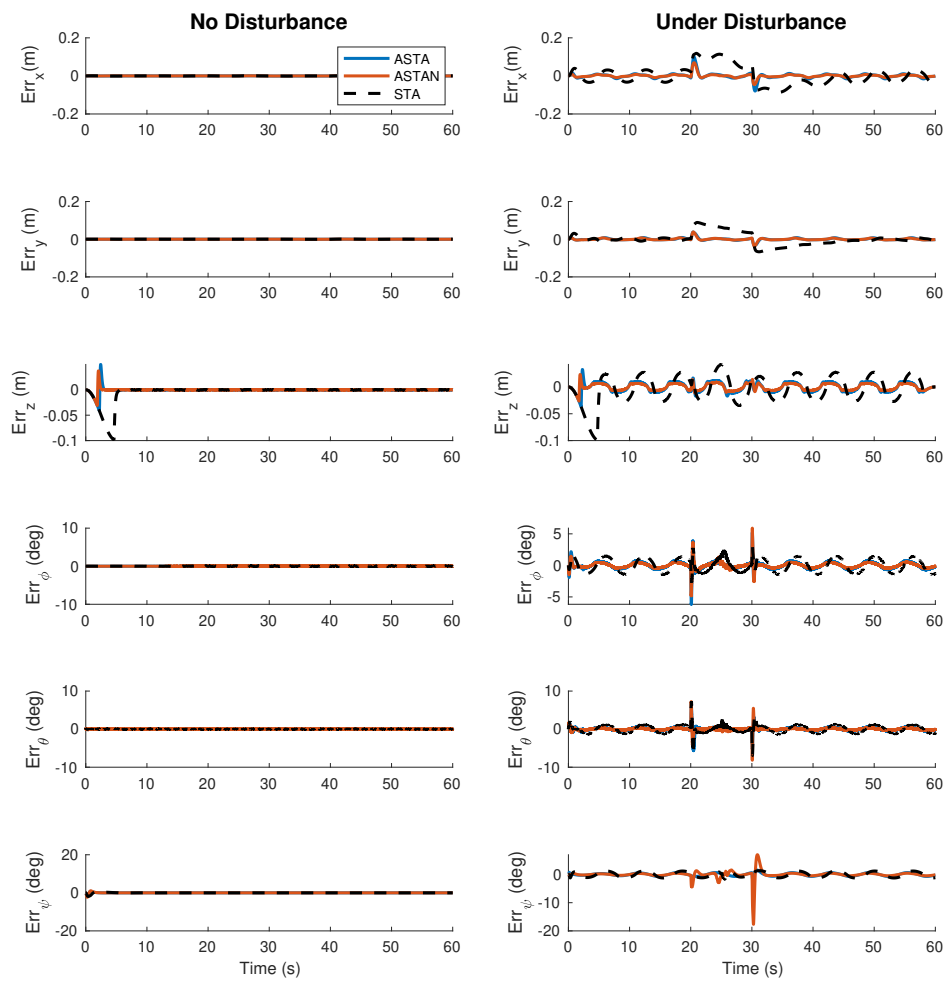
Figure 4.3: Tracking error results in simulation
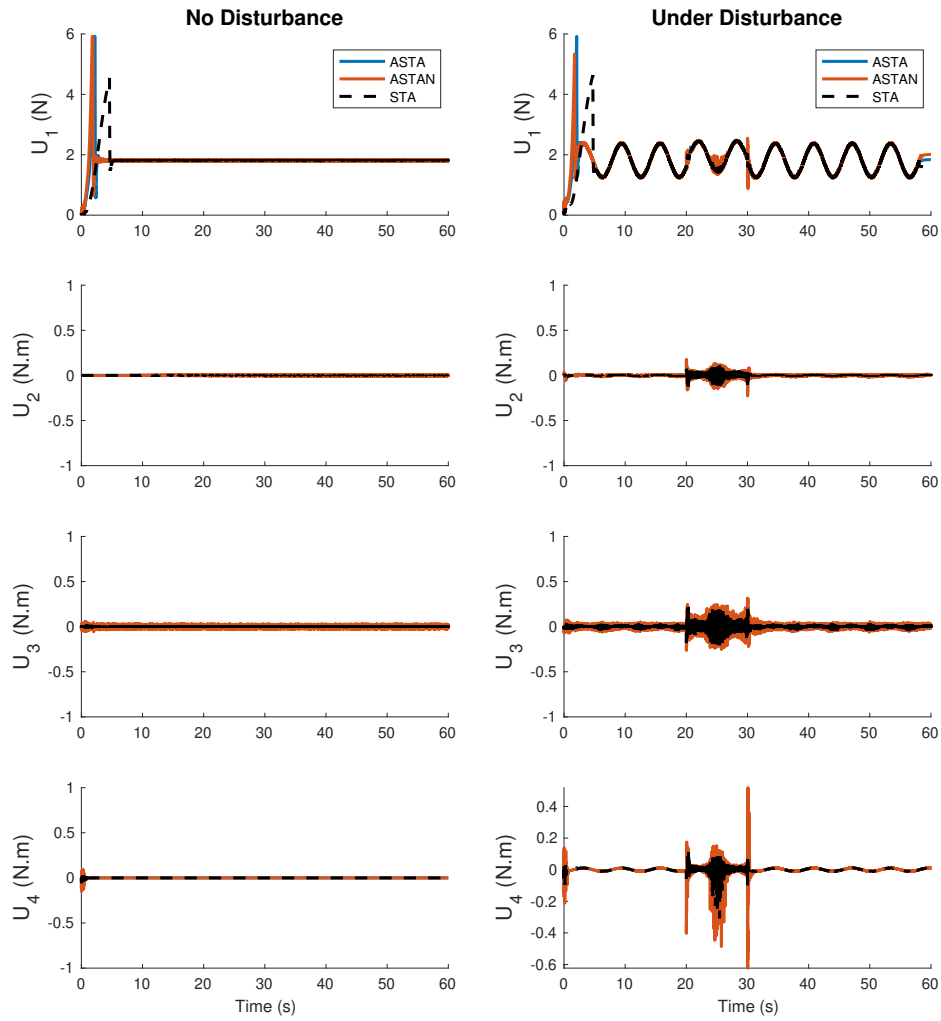
Figure 4.4: Control input profiles in simulation
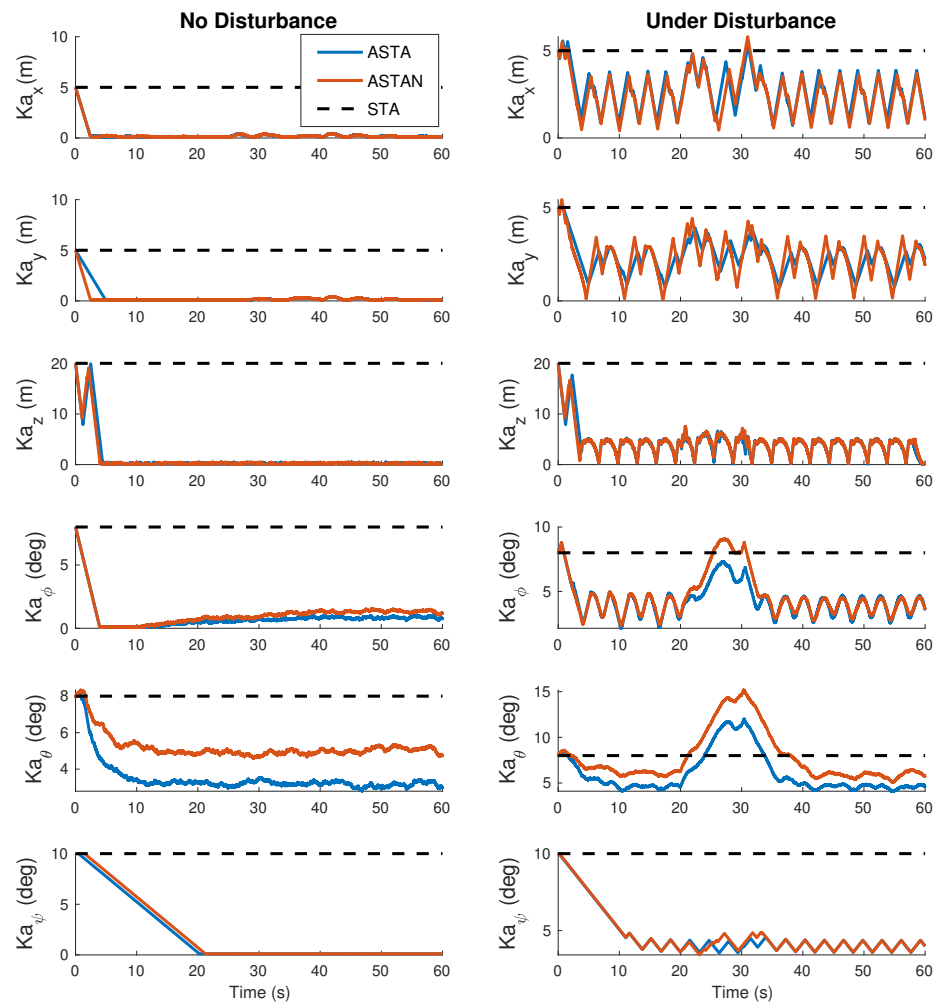
Figure 4.5: Results of adaptive gain k_a in simulation
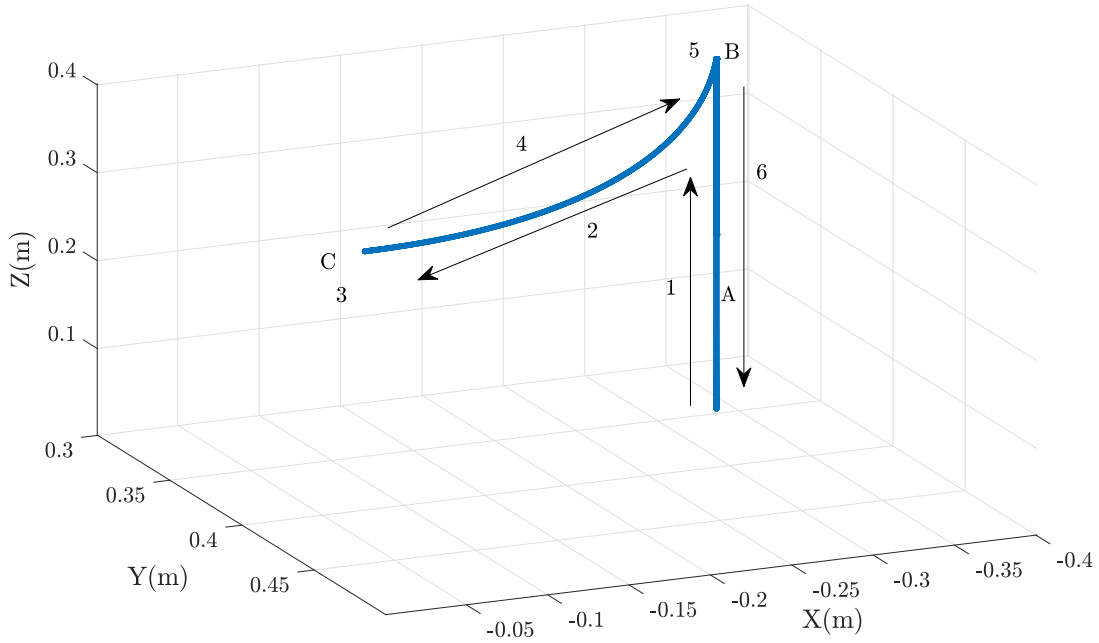
Figure 4.6: 3D desired trajectory in experiment

4.4.2   Experimental Results

The experimental results of trajectory tracking and stabilization for the proposed controller are explained in this section. Figure 4.6 displays the desired trajectory in the experiment. It consisted of six motions during 60 s with the following arrangement: (1) take off: from A to B (0–10 s); (2) yaw and x–y plane maneuvers: from B to C (10–15 s); (3) hovering, at C (15–30 s); (4) maneuvers: from C to B (30–34 s); (5) hovering: at B (34–50 s); and (6) landing: from B to A (50–60 s). We applied wind disturbance by using a 57 W electric fan to verify the robustness of the proposed method at distances of 0.5–1.5 m (Fig. 4.1). The disturbance magnitude was proportional to the distance between the quadcopter and the fan. The variable disturbance conditions were considered along the trajectory from B to C and vice versa with a maximum at C. The position and direction of the fan was fixed to generate different air flow directions to the motion of the quadcopter in the desired trajectory. Therefore,

we could evaluate the effectiveness of the proposed controller by using
the variable magnitudes and directions of the wind disturbance.   The
environment in the experimental testbed included dynamics uncertainties
and perturbation, which were different from the simulation. We obtained
the controller parameters from the various experiments as follows (units
are omitted): $k_a = \textbf{diag}\{1, 1, 4, 8, 8, 15\}$, $k_b = \textbf{diag}\{0.5\ 0.5, 0.5, 1, 1, 8\}$,
and $k_c = \textbf{diag}\{0.1, 0.1, 0.1, 0.1, 0.1, 0.1\}$. The NSS parameters were $F =$
$\textbf{diag}\{5, 5, 5, 5, 5, 50\}$, and $\beta = \textbf{diag}\{15, 15, 15, 10, 10, 150\}$. The values of
β should be designed properly because a relatively small value would still
give a chattering effect, whereas a relatively large value would reduce the
robustness according to the previous work [93]. The tuning parameters
for the ASTA were $\overline{k} = [0.01, 0.01, 0.01, 0.05, 0.05, 0.04]$, $\gamma_i = 2$, $\mu_i = [2,$
$2, 1, 1, 1, 1]$, $k_{mi} = 0.1$, $k_d = [0.07, 0.1, 0.1, 0.06, 0.06, 0.6]$, $i = 1, 2, ..6$, and
$\eta = k_m$.

4.4.2.1   Control Performance Evaluation

Figure 4.7 shows the tracking errors resulting from the three control
experimental strategies without/under wind disturbance.   Both control
strategies provided robustness in the two disturbance conditions.
Generally, a larger error occurred with the quadcopter hovering after
maneuvering.   All states had larger magnitude errors with wind
disturbances than without. During hovering, the pitch motion exhibited
larger error results than the other state motions, thus implying that it was
largely affected by wind disturbance. From Table 4.3, we could conclude
that ASTAN produces the smallest tracking errors among the rest of the
states in both disturbance conditions. On the contrary, we evaluated the
reproducibility of these controllers via a five-time repetition of a single
experiment. Figures 4.8 and 4.9 show the results. On average, ASTAN
yielded mean values that were approximately 2% and 3.5% smaller than

those of ASTA and STA, respectively, in both disturbance conditions, but it correspondingly produced variances that were approximately 1.5% and 5% smaller without wind disturbance. Figure 4.10 illustrates the performance of the controller in each trajectory condition in Fig. 4.6. On average, ASTAN was more effective than the others for maneuvering and hovering without wind disturbance.

Furthermore, Fig. 4.11 shows the profiles of the control input. Control input u1 produced a great total thrust to lift the quadcopter minimum value to almost 2 N. For the initial takeoff, the quadcopter required a total force of nearly 3.5–4 N, which continually increased under wind disturbance, particularly at a maximum disturbance near position C (30–35 s) proximal to the fan. Figures 4.12 and 4.13 summarize the variances of control inputs, and Table 4.4. Figure 4.13 shows that the takeoff motion produced larger magnitudes of chattering, which increased during hovering motion proximal to the fan. Therefore, ASTAN provided low variance in the control inputs, and its effectiveness in reducing chattering was verified in all conditions.

Moreover, we use the voltage formula and power measurement for each motor, as obtained from Ref. [49], including the calculation of power exerted by each motor from control inputs u_1, u_2, u_3, and u_4. The DC motors were assumed to have identical resistance loads for the estimation of power consumption. The chattering of the control inputs caused a corresponding chattering in the electric power of each motor.

The total energy consumed in each actuator was calculated by integrating its electric power during motion. The effect of chattering on energy consumption was evaluated for a similar five-time experiment without/with wind disturbance (Fig. 4.14 and Table 4.5). The results showed that ASTAN was most effective at reducing energy consumption in both conditions, as illustrated by values that are 3% and 5% higher
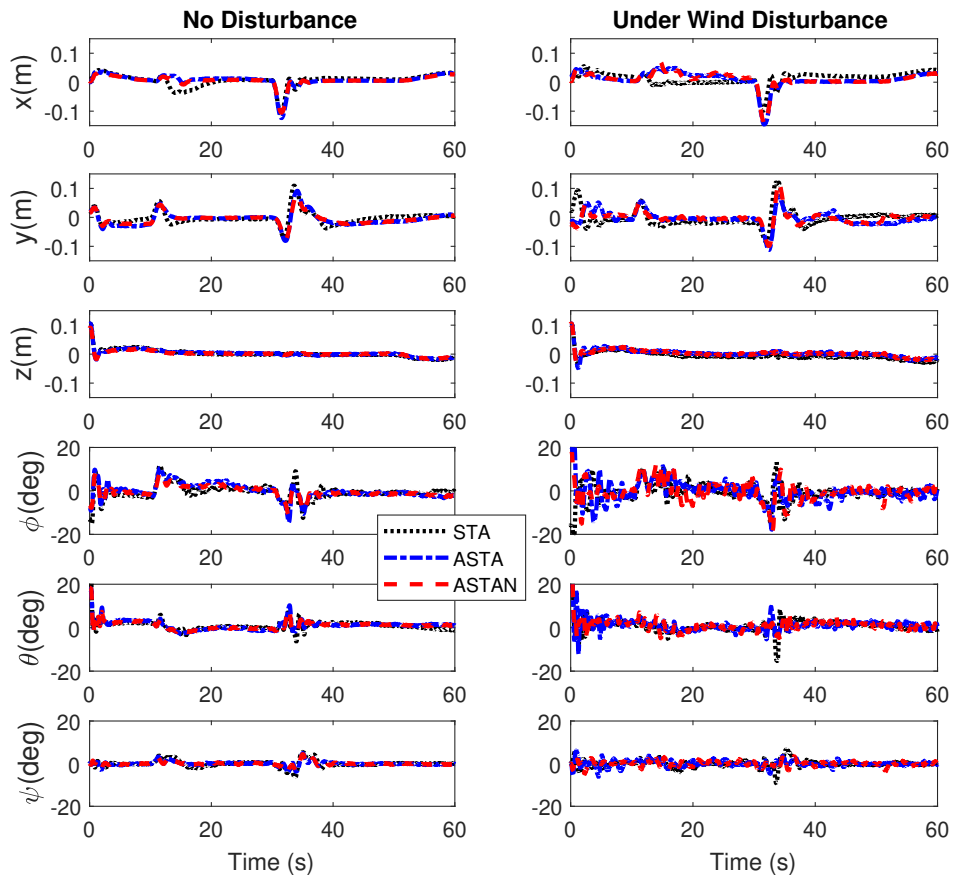
Figure 4.7: Tracking error profiles in experiment

in ASTA and STA (without disturbance), respectively, and 1.4% and 3.3%
higher in ASTA and STA (under wind disturbance), respectively.

We extended the evaluation in six trials to obtain the information of
energy consumption during operational flight (Figs 4.15 and 4.16. Figure
4.15 describes the average energy consumption for each motion, in which
the hovering motion consumed less energy than the other motions. On the
other contrary, Figure 4.16 describes the energy consumption for several
experiments in each motion, where ASTAN has less energy consumption
significantly for a case without disturbance. Although there was no
significant difference in energy consumption under wind disturbance,
ASTAN had less energy consumption than the others during hovering
motion on average.
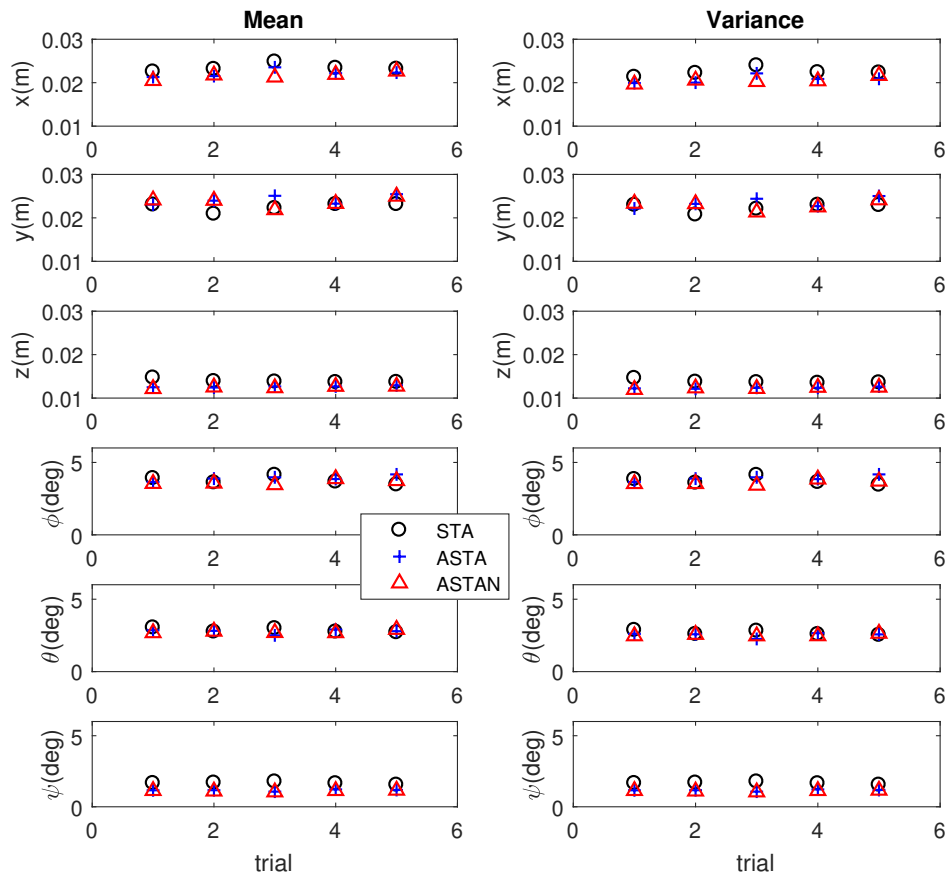
Figure 4.8: Comparison of root mean square and variance of tracking errors without wind diturbance

Table 4.3: Tracking error comparison results in experiment

Disturbance	Controller	Mean		Variance	
		(cm)	(deg)	(cm)	(deg)
None	STA	1.99	1.675	1.95	1.675
	ASTA	1.96	1.135	1.88	1.134
	ASTAN	1.92	1.134	1.85	1.133
Wind	STA	2.30	1.589	2.14	1.588
	ASTA	2.17	1.332	2.11	1.33
	ASTAN	2.14	1.313	2.08	1.311

Table 4.4: Control input variance comparison results in experiment

Controller	Variance	
	None	Wind
STA	0.1472	0.1566
ASTA	0.1484	0.1544
ASTAN	0.1458	0.146
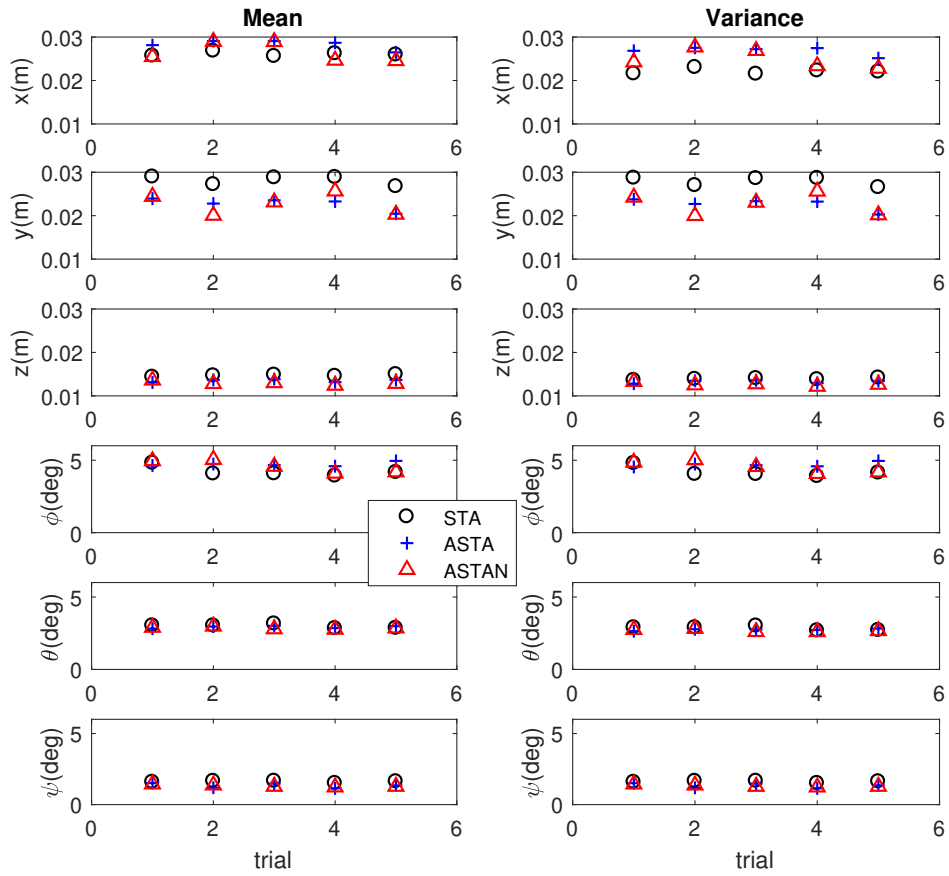
Figure 4.9: Comparison of root mean square and variance of tracking erros
under wind disturbance

Table 4.5: Total energy comparison results in experiment

Dist. Cont.	None E (mWh)	Wind E (mWh)
STA	302.5	299.5
ASTA	297.0	293.4
ASTAN	288.3	289.8
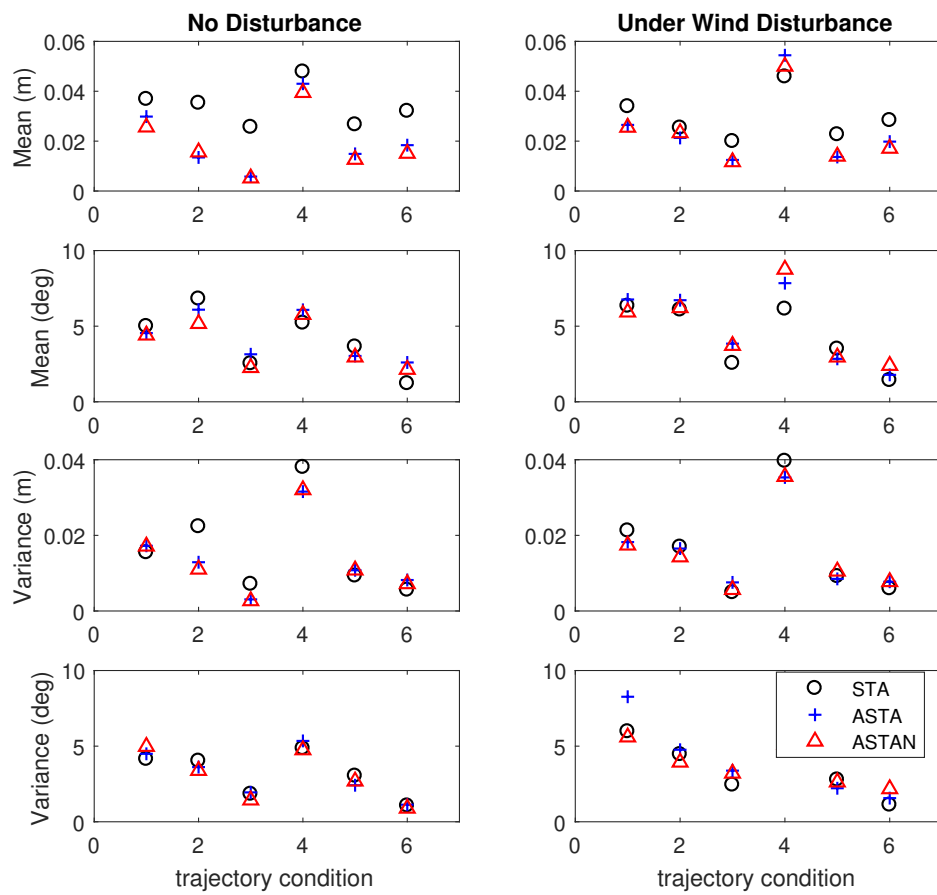
Figure 4.10: Comparison of root mean square and variance of tracking errors in six trajectory conditions
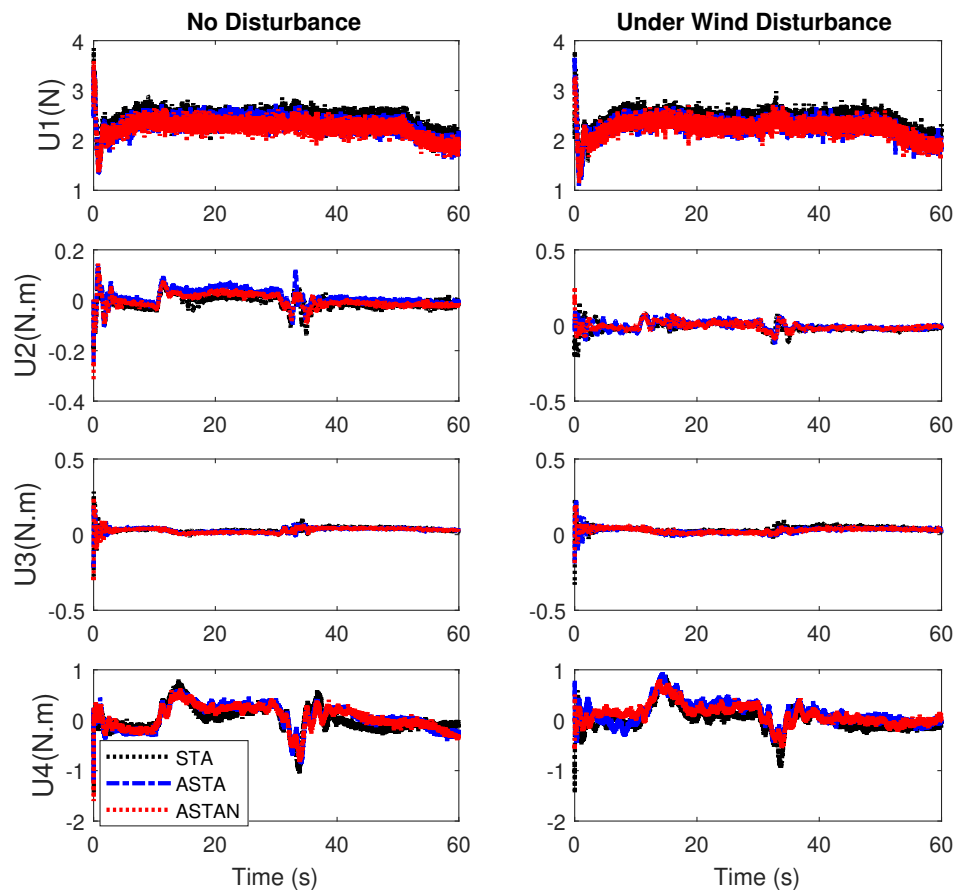
Figure 4.11: Control input profiles
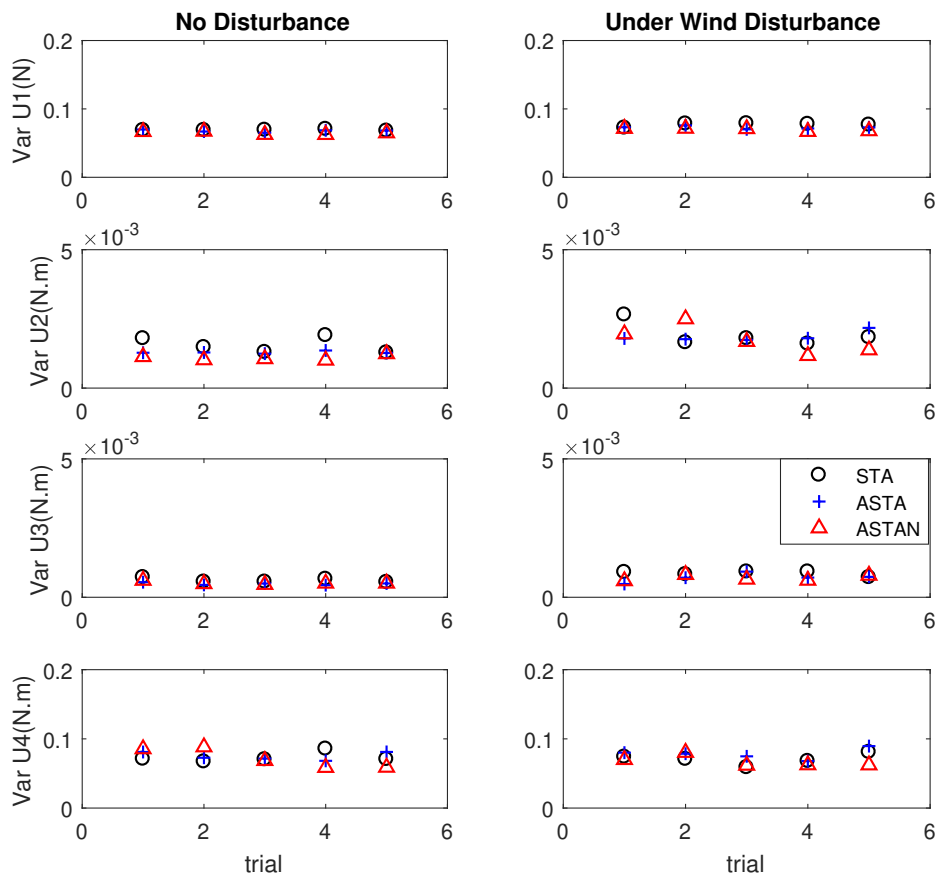
Figure 4.12: Control input variance in five times experiment
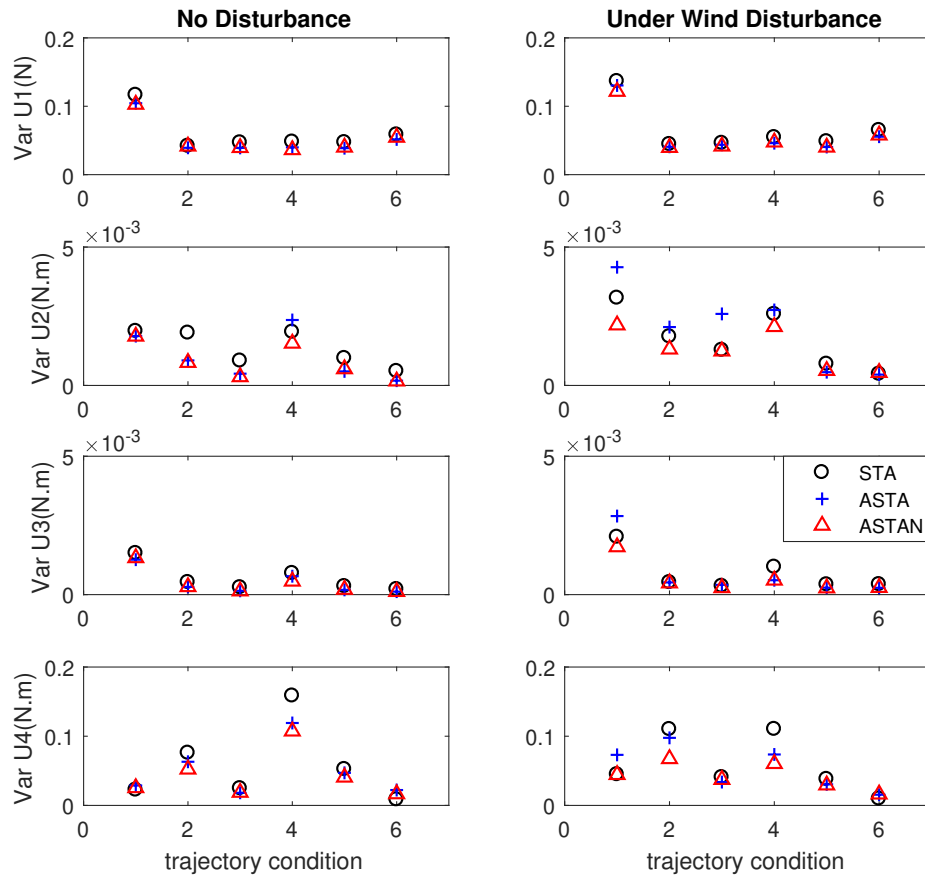
Figure 4.13: Control input variance in six trajectory conditions
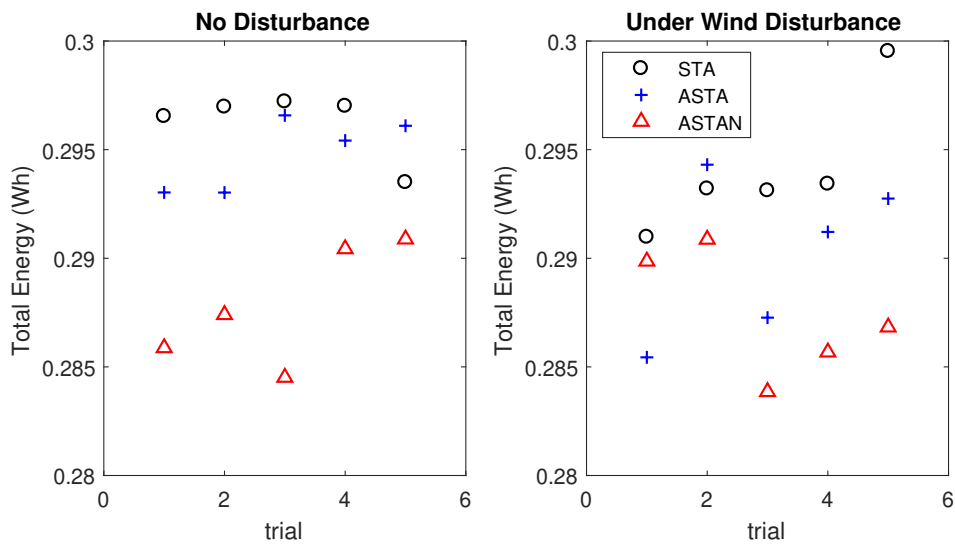
Figure 4.14: Total energy consumed in actuators in five times experiment
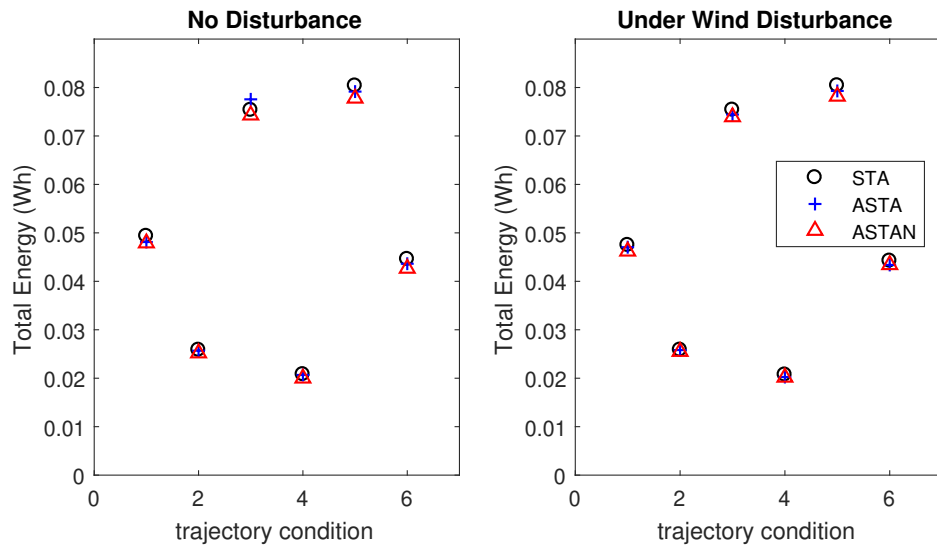
Figure 4.15:   Total energy consumed in actuators for each trajectory condition
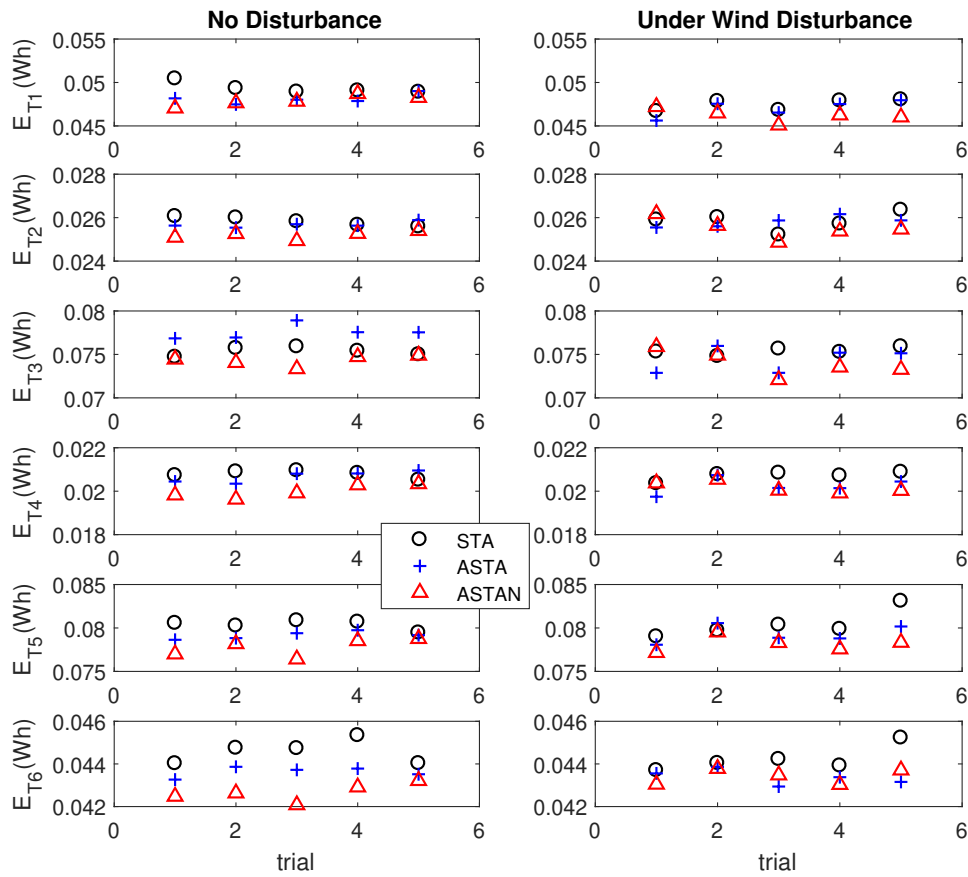
Figure 4.16:   Total energy consumed in actuators for six trajectory conditions (E_{Ti}: energy consumption in the i-th trajectory condition)

4.5   Conclusion

For this chapter, we designed an ASTAN for the trajectory tracking
of a quadcopter system.   Considering that the parameter adjustment
of NSS was sensitive, we included an adaptation mechanism on the
basis of Lyapunov stability theory.   The designed ASTAN was verified
by comparative simulation and experiments with conventional STA and
ASTA. The results showed that it maintains stability against external
disturbances and provides smaller tracking errors.   Specifically, the
experiment results verified its superior performance over the STA and
ASTA, as indicated by the higher reduction in the average mean of tracking
error by 2% and 3.5% (cm) than in STA and ASTA in both conditions,
respectively (1% and 32% [deg] without disturbance and 1.5% and 17.3%
[deg] under wind disturbance).   Moreover, the variance of the tracking
error reductions were higher by 1.5% and 5% (cm) than in STA and ASTA,
respectively, without wind disturbance and higher by 1.5% and 2.8% (cm)
under wind disturbance than in STA and ASTA, respectively(1% and 30%
[deg] without disturbance and 1.5% and 17.5% under wind disturbance).
ASTAN was also effective in reducing energy consumption by 3% and 5%
higher without wind disturbance than in STA and ASTA, respectively, and
1.4% and 3.3% higher under wind disturbance than in STA and ASTA. In
our future work, we aim to include unmatched disturbance rejection and
plan to conduct an outdoor experiment with the proposed control method.

Chapter 5

Conclusion

5.1 Summary

In this thesis, we presented experiments to design a robust and energy-efficient SMC-adaptive-based controller for a quadcopter. The quadcopter had 6-DOFs and was controlled by four independent inputs, which were less than the total number of DOFs; given the difference in the number of inputs and outputs, this specification describes an underactuated system. In theory, it is difficult to control all DOFs directly and simultaneously in such a system. Thus, we selected the desired outputs as position and yaw angles to match the underactuated system. Virtual input was introduced to create a fully actuated system and establish a decoupled system where the input on each motion can be controlled independently. Moreover, a cascade control structure was constructed on the basis of the translational and rotational dynamics. The original input could be obtained by algebraic calculations from the equations of translational dynamics by using the least squares method and from the equations of rotational dynamics by using dynamic inversion with a reference virtual input. Therefore, this feature structure enabled the easy control of the quadcopter with any common control algorithm.

Considering that the quadcopter experimental testbed can only provide measurements of absolute position and attitude states on each sampling time, we applied a velocity states estimator on the basis of a reduced-order observer, which performs estimations by using a continuous-time dynamic model that considers the discrete-time control system. Moreover, we presented a quadcopter velocity estimator based on the sampled data of position measurement and experimentally confirmed its effectiveness by using a reduced-order observer. We introduced an SMC for stabilizing and tracking the desired trajectory and then evaluated its effectiveness via a comparison against a backward-difference method with a low-pass filter. The reduced-order observer estimated the quadcopter velocity from its initial value within 25 ms after the fifth sampling time; this result was acceptable and suitable in terms of practical applications. Furthermore, the reduced-order observer enabled us to choose a relatively higher gain for the closed-loop controller, thus greatly reducing the tracking error while increasing control performance.

We also introduced an adaptive nonlinear design for robust tracking and energy saving based on the SMC of quadcopter dynamics. The strategy proved successful in controlling systems that are affected by uncertainty/disturbance. A conventional SMC is characterized by the presence of high-frequency oscillations in the control input, i.e., chattering, which potentially damages the actuators and increase the energy consumption of the quadcopter. Its other drawback is the required knowledge of uncertainty/disturbance bounds. To improve this weakness, we proposed an adaptive gain tuning mechanism based on STA that can estimate the uncertainty adaptively. By using this mechanism, namely, STA-SMC, a knowledge uncertainty/disturbance boundary is no longer needed.

An adaptive sliding mode dynamically increases the control gain until

the two-sliding-mode is reached. Thereafter, the gain starts to decrease or increase again as soon as the sliding variable or its derivative starts deviating from the equilibrium point of the two-sliding-mode. We used the boundary layer of sliding-modes as a "limiter" for this adaptive SMC, thus preventing the overestimation of the control gains. When the condition of the sliding variable is under the boundary layer, the gain is dynamically reduced until the condition is reversed. Alternately, the gain is dynamically increased to force the sliding variable to reach the previous condition in finite time.

The proposed adaptive sliding-mode strategy was used to design an STA-SOSMC for a quadcopter. To improve the transient performance of the quadcopter, we further developed an NLSS-based adaptive chattering-free SMC. The NLSS was considered in this sliding-mode design to improve a time-varying constant of the closed-loop dynamics (the damping ratio and natural frequency). Therefore, a fast initial response and a gradual decrease of overshoot should occur and reduce chattering. With this consideration, energy reduction can be achieved in the control strategy. The stability of this control strategy is guaranteed in the sense of Lyapunov stability theory. Practically, we evaluated its effectiveness by repeating a single experiment in the quadcopter testbed set-up multiple times.

Experimental results showed that ASTAN provides similar robustness to ASTA; however, ASTAN consumes less energy than the linear sliding surface. To evaluate the performance of the control strategies discussed in this thesis in terms of robustness and energy efficiency, we summarized the experimental results for the reduced-order observer and the backward-difference methods in Tables 5.1-5.3.

As shown in Tables 5.1and 5.2, ASTAN outperformed other controller approaches, as indicated by the low RMSE in both translational and rotational motions without and with wind disturbance conditions.

Table 5.1: Root-squared mean of error (RSME) and Variance of error without disturbance

Controller	Translational Motion (cm)		Rotational Motion (deg)	
	RSME	Variance	RSME	Variance
SMC+Backward-diff	3.108	2.981	3.569	3.408
SMC+Roo	1.999	2.070	2.000	1.593
STA+Roo	1.991	1.954	1.675	1.675
ASTA+Roo	1.962	1.883	1.135	1.134
ASTAN+Roo	1.921	1.852	1.134	1.133

Table 5.2: RSME and Variance of error under disturbance

Component	Translational Motion		Rotational Motion	
	RSME (cm)	Variance	RSME (deg)	Variance
SMC+Backward-diff	3.514	3.293	3.147	3.131
SMC+Roo	2.42	2.045	1.803	1.790
STA+Roo	2.30	2.14	1.589	1.588
ASTA+Roo	2.17	2.11	1.332	1.33
ASTAN+Roo	2.14	2.08	1.313	1.311

Similarly, the evaluations of energy consumption showed that ASTAN have better control performance than the others approaches because it consumes less energy (Table 5.3).

5.2   Future Works

1. In this thesis, we considered a fan as the source of an external disturbance (logically known as a matched disturbance). However, the proposed control method may not be fast enough to compensate all known disturbances such as unmatched disturbance (e.g.,., dynamic payload movements or unstable actuators). Our future work will extend the scope of the thesis to an unmatched disturbance rejection.

2. Payloads in quadcopters are new and interesting topics of research. However, the distance between the quadcopter and payload can produce a number of swinging motions that can potentially increase

Table 5.3: Total energy consumption

Controller	without disturbance (mWh)	with disturbance (mWh)
SMC+Backward-diff	310.7	305.4
SMC+Roo	305.6	301.3
STA+Roo	302.5	299.5
ASTA+Roo	297.0	293.4
ASTAN+Roo	288.3	289.8

tracking error and energy consumption. In the future, this work will be extended to the attachment of a payload to the quadcopter and the addition of an antiswing algorithm to the existing controller.

3. The effectiveness and performance of all controller strategies discussed in this thesis were evaluated for an indoor environment. In the future, this work will be extended to an outdoor setting.

4. Many commercial quadcopters have closed sources of the method. In other word, they already have a fixed algorithm. In the future, our proposed control strategy will be evaluated on a commercial quadcopter.

Bibliography

[1] R. Ghazali, Y. M. Sam, M. F. Rahmat, A. W. I. M. Hashim, and
. Zulfatman, "Performance comparison between sliding mode control
with PID sliding surface and PID controller for an electro-hydraulic
positioning system," *International Journal on Advanced Science,
Engineering and Information Technology*, vol. 1, no. 4, p. 447, 2011.

[2] J. F. Roberts, J. C. Zufferey, and D. Floreano, "Energy management
for indoor hovering robots," in *IEEE/RSJ International Conference
on Intelligent Robots and Systems, IROS*, pp. 1242–1247, 2008.

[3] D. Aleksandrov and I. Penkov, "Optimal gap distance between
rotors of mini quadrotor helicopter," in *International DAAAM Baltic
Conference "MECHATRONICS AND SYSTEM ENGINEERING"*,
no. April, 2012.

[4] E. Fresk and G. Nikolakopoulos, "Experimental model derivation and
control of a variable pitch propeller equipped quadrotor," in *IEEE
Conference on Control Applications (CCA)*, pp. 723–729, 2014.

[5] S. González-Vázquez and J. Moreno-Valenzuela, "Motion control of a
quadrotor aircraft via singular perturbations," *International Journal
of Advanced Robotic Systems*, vol. 10, no. 10, p. 368, 2013.

[6] D. Lee, H. J. Kim, and S. Sastry, "Feedback linearization vs. adaptive
sliding mode control for a quadrotor helicopter," *International*

Journal of Control, Automation and Systems, vol. 7, no. 3, pp. 419–428, 2009.

[7] E. Altuğ, J. P. Ostrowski, and C. J. Taylor, "Control of a quadrotor helicopter using dual camera visual feedback," *The International Journal of Robotics Research*, vol. 24, no. 5, pp. 329–341, 2005.

[8] E. Altuğ, J. P. Ostrowski, and R. Mahony, "Control of a quadrotor helicopter using visual feedback," in *IEEE International Conference on Robotics and Automation*, vol. 1, pp. 72–77, IEEE, 2002.

[9] H. Bouadi and M. Tadjine, "Nonlinear observer design and sliding mode control of four rotors helicopter," in *World academy of science, engineering and technology*, vol. 25, pp. 225–230, 2007.

[10] A. Mokhtari and A. Benallegue, "Dynamic feedback controller of Euler angles and wind parameters estimation for a quadrotor unmanned aerial vehicle," in *IEEE International Conference on Robotics and Automation*, vol. 3, pp. 2359–2366, IEEE, 2004.

[11] A. Mokhtari, N. M'Sirdi, K. Meghriche, and A. Belaidi, "Feedback linearization and linear observer for a quadrotor unmanned aerial vehicle," *Advanced Robotics*, vol. 20, no. 1, pp. 71–91, 2006.

[12] A. Benallegue, A. Mokhtari, and L. M. Fridman, "High-order sliding-mode observer for a quadrotor UAV," *International Journal of Robust and Nonlinear Control*, vol. 18, no. 4-5, pp. 427–440, 2008.

[13] L. Besnard, Y. B. Shtessel, and B. Landrum, "Quadrotor vehicle control via sliding mode controller driven by sliding mode disturbance observer," *Journal of the Franklin Institute*, vol. 349, no. 2, pp. 658–684, 2012.

[14] S. Bouabdallah and R. Siegwart, "Backstepping and sliding-mode techniques applied to an indoor micro Quadrotor," in *IEEE International Conference on Robotics and Automation*, vol. 2005, pp. 2247–2252, 2005.

[15] A. A. Mian and D. Wang, "Modeling and backstepping-based nonlinear control strategy for a 6 DOF quadrotor helicopter," *Chinese Journal of Aeronautics*, vol. 21, no. 3, pp. 261–268, 2008.

[16] Q. Hu, Q. Fei, Q. Wu, and Q. Geng, "Research and application of nonlinear control techniques for quad rotor UAV," in *Chinese Control Conference*, pp. 706–710, 2012.

[17] R. Xu and U. Ozguner, "Sliding mode control of a quadrotor helicopter," in *IEEE Conference on Decision and Control*, pp. 4957–4962, 2006.

[18] L. R. Garcia-Carrillo, E. Rondon, A. Dzul, A. Sanchez, and R. Lozano, "Hovering quad-rotor control: A comparison of nonlinear controllers using visual feedback," in *IEEE Conference on Decision and Control*, vol. 48, pp. 1662–1667, IEEE, 2010.

[19] M. Ö. Efe, "Robust low altitude behavior control of a quadrotor rotorcraft through sliding modes," in *Mediterranean Conference on Control and Automation, MED*, 2007.

[20] L. Luque-Vega, B. Castillo-Toledo, and A. G. Loukianov, "Block linearization control of a quadrotor via sliding mode," in *American Control Conference*, pp. 149–154, IEEE, 2012.

[21] L. Luque-Vega, B. Castillo-Toledo, and A. G. Loukianov, "Robust block second order sliding mode control for a quadrotor," *Journal of the Franklin Institute*, vol. 349, no. 2, pp. 719–739, 2012.

[22] E.-h. Zheng and J. Xiong, "Quad-rotor unmanned helicopter control via novel robust terminal sliding mode controller and under-actuated system sliding mode controller," *International Journal for Light and Electron Optics*, vol. 125, no. 12, pp. 2817–2825, 2014.

[23] E.-H. Zheng, J.-J. Xiong, and J.-L. Luo, "Second order sliding mode control for a quadrotor UAV," *ISA Transactions*, vol. 53, no. 4, pp. 1350–1356, 2014.

[24] F. Kendoul, D. Lara, I. Fantoni, and R. Lozano, "Nonlinear control for systems with bounded inputs: Real-time embedded control applied to UAVs," in *IEEE Conference on Decision and Control*, pp. 5888–5893, IEEE, 2006.

[25] M. R. Mokhtari and B. Cherki, "A new robust control for minirotorcraft unmanned aerial vehicles," *ISA Transactions*, vol. 56, pp. 86–101, 2015.

[26] V. Rejón and E. Aranda-Bricaire, "Discrete-time dynamic feedback linearization of a VTOL using observed states," in *IFAC Proceedings Volumes*, vol. 41, pp. 1753–1759, 2008.

[27] T. Chen and B. A. Francis, *Optimal sampled-data control systems*. Springer, 1995.

[28] D. Nešić, A. Teel, and P. Kokotović, "Sufficient conditions for stabilization of sampled-data nonlinear systems via discrete-time approximations," *Systems & Control Letters*, vol. 38, no. 4-5, pp. 259–270, 1999.

[29] H. Katayama and H. Aoki, "Reduced-order observers for nonlinear sampled-data systems with application to marine systems," in *IEEE Conference on Decision and Control*, pp. 5072–5077, IEEE, 2013.

[30] R. Akbar, B. Sumantri, H. Katayama, S. Sano, and N. Uchiyama, "Reduced-order observer based sliding mode control for a quad-rotor helicopter," *Journal of Robotics and Mechatronics*, vol. 28, no. 3, pp. 1–16, 2016.

[31] S. Bouabdallah, A. Noth, and R. Siegwart, "PID vs LQ control techniques applied to an indoor micro quadrotor," in *IEEE/RSJ International Conference on Intelligent Robots and Systems*, vol. 3, pp. 2451–2456, 2004.

[32] J. Li and Y. Li, "Dynamic analysis and PID control for a quadrotor," in *International Conference on Mechatronics and Automation*, pp. 573–578, 2011.

[33] P. E. Pounds, R. Mahony, and P. Corke, "Modelling and control of a large quadrotor robot," *Control Engineering Practice*, vol. 18, no. 7, pp. 691–699, 2010.

[34] P. E. Pounds, D. R. Bersak, and A. M. Dollar, "Stability of small-scale UAV helicopters and quadrotors with added payload mass under PID control," *Autonomous Robots*, vol. 33, no. 1-2, pp. 129–142, 2012.

[35] G. M. Hoffmann, H. Huang, S. L. Waslander, and C. J. Tomlin, "Precision flight control for a multi-vehicle quadrotor helicopter testbed," *Control Engineering Practice*, vol. 19, no. 9, pp. 1023–1036, 2011.

[36] A. Tayebi and S. McGilvray, "Attitude stabilization of a VTOL quadrotor aircraft," *IEEE Transactions on Control Systems Technology*, vol. 14, no. 3, pp. 562–571, 2006.

[37] D. Lara, G. Romero, A. Sanchez, R. Lozano, and A. Guerrero, "Robustness margin for attitude control of a four rotor mini-

rotorcraft: Case of study," *Mechatronics*, vol. 20, no. 1, pp. 143–152, 2010.

[38] Y. Yu, X. Ding, and J. J. Zhu, "Attitude tracking control of a quadrotor UAV in the exponential coordinates," *Journal of the Franklin Institute*, vol. 350, no. 8, pp. 2044–2068, 2013.

[39] Z. He and L. Zhao, "A simple attitude control of quadrotor helicopter based on Ziegler-Nichols rules for tuning pd parameters," *Scientific World Journal*, vol. 2014, 2014.

[40] A. A. H. Saif, "Quadrotor control using feedback linearization with dynamic extension," in *International Symposium on Mechatronics and its Applications, ISMA 2009*, 2009.

[41] H. Voos, "Nonlinear control of a quadrotor micro-uav using feedback-linearization," in *IEEE International Conference on Mechatronics*, 2009.

[42] N. Sydney, B. Smyth, and D. A. Paley, "Dynamic control of autonomous Quadrotor flight in an estimated wind field," in *IEEE Conference on Decision and Control*, pp. 3609–3616, 2013.

[43] J. Ghandour, S. Aberkane, and J.-C. Ponsart, "Feedback linearization approach for standard and fault tolerant control: application to a quadrotor UAV testbed," *Journal of Physics: Conference Series*, vol. 570, no. 8, p. 082003, 2014.

[44] D. Lee, T. C. Burg, D. M. Dawson, D. Shu, B. Xian, and E. Tatlicioglu, "Robust tracking control of an underactuated quadrotor aerial-robot based on a parametric uncertain model," in *IEEE International Conference on Systems, Man and Cybernetics*, pp. 3187–3192, 2009.

[45] P. Castillo, A. Dzul, and R. Lozano, "Real-time stabilization and tracking of a four-rotor mini rotorcraft," *IEEE Transactions on Control Systems Technology*, vol. 12, no. 4, pp. 510–516, 2004.

[46] S. Salazar-Cruz, A. Palomino, and R. Lozano, "Trajectory tracking for a four rotor mini-aircraft," in *IEEE Conference on Decision and Control*, vol. 2005, pp. 2505–2510, IEEE, 2005.

[47] J. Guerrero-Castellanos, N. Marchand, A. Hably, S. Lesecq, and J. Delamare, "Bounded attitude control of rigid bodies: Real-time experimentation to a quadrotor mini-helicopter," *Control Engineering Practice*, vol. 19, no. 8, pp. 790–797, 2011.

[48] H. Bouadi, M. Bouchoucha, and M. Tadjine, "Modelling and stabilizing control laws design based on backstepping for an UAV type-quadrotor," *IFAC Proceedings Volumes*, vol. 40, no. 15, pp. 245–250, 2007.

[49] B. Sumantri, N. Uchiyama, and S. Sano, "Least square based sliding mode control for a quad-rotor helicopter and energy saving by chattering reduction," *Mechanical Systems and Signal Processing*, vol. 66-67, pp. 769–784, 2016.

[50] S. L. Waslander, G. M. Hoffmann, J. S. Jang, and C. J. Tomlin, "Multi-agent quadrotor testbed control design: integral sliding mode vs. reinforcement learning," in *IEEE/RSJ International Conference on Intelligent Robots and Systems, IROS*, pp. 468–473, 2005.

[51] X. Gong, Z.-C. Hou, C.-J. Zhao, Y. Bai, and Y.-T. Tian, "Adaptive backstepping sliding mode trajectory tracking control for a quad-rotor," *International Journal of Automation and Computing*, vol. 9, no. 5, pp. 555–560, 2012.

[52] F. Sharifi, M. Mirzaei, B. W. Gordon, and Y. Zhang, "Fault tolerant control of a quadrotor UAV using sliding mode control," in *Conference on Control and Fault-Tolerant Systems (SysTol)*, pp. 239–244, 2010.

[53] A. Das, F. Lewis, and K. Subbarao, "Sliding mode approach to control quadrotor using dynamic inversion," *Intechopen.Com*, 2006.

[54] H. Mohamed, S. S. Yang, and M. Moghavvemi, "Sliding mode controller design for a flying quadrotor with simplified action planner," in *Iccas-Sice*, pp. 1279–1283, 2009.

[55] A. R. Patel, M. A. Patel, and D. R. Vyas, "Modeling and analysis of quadrotor using sliding mode control," in *Southeastern Symposium on System Theory (SSST)*, pp. 111–114, 2012.

[56] M. Guisser and H. Medromi, "A high gain observer and sliding mode controller for an autonomous quadrotor helicopter," *International Journal of Intelligent Control and Systems*, vol. 14, pp. 204–212, 2009.

[57] J.-J. Xiong and E.-H. Zheng, "Position and attitude tracking control for a quadrotor UAV," *ISA Transactions*, vol. 53, no. 3, pp. 725–731, 2014.

[58] L. Derafa, L. M. Fridman, A. Benallegue, and A. Ouldali, "Super twisting control algorithm for the four rotors helicopter attitude tracking problem," in *International Workshop on Variable Structure Systems (VSS)*, pp. 62–67, IEEE, 2010.

[59] M. Bouchoucha, S. Seghour, and M. Tadjine, "Classical and second order sliding mode control solution to an attitude stabilization of a four rotors helicopter: From theory to experiment," in *IEEE International Conference on Mechatronics*, pp. 162–169, 2011.

[60] L. Derafa, A. Benallegue, and L. M. Fridman, "Super twisting control algorithm for the attitude tracking of a four rotors UAV," *Journal of the Franklin Institute*, vol. 349, no. 2, pp. 685–699, 2012.

[61] B. Sumantri, N. Uchiyama, and S. Sano, "Second order sliding mode control for a quad-rotor helicopter with a nonlinear sliding surface," in *IEEE Conference on Control Applications*, vol. 53, pp. 742–746, 2014.

[62] U. Itkis, *Control systems of variable structure*. Wiley, 1976.

[63] V. I. Utkin, "Variable structure systems with sliding modes," *IEEE Transactions on Automatic Control*, vol. 22, no. 2, pp. 212–222, 1977.

[64] J. Hung, W. Gao, and J. Hung, "Variable structure control: a survey," *IEEE Transactions on Industrial Electronics*, vol. 40, no. 1, pp. 2–22, 1993.

[65] W. L. Jean Slotine, *Applied Nonlinear Control*. Prentice Hall, 1991.

[66] A. Levant, "Sliding order and sliding accuracy in sliding mode control," *International Journal of Control*, vol. 58, no. 6, pp. 1247–1263, 1993.

[67] J. A. Moreno and M. Osorio, "A Lyapunov approach to second-order sliding mode controllers and observers," in *IEEE Conference on Decision and Control*, pp. 2856–2861, 2008.

[68] J. A. Moreno, "A linear framework for the robust stability analysis of a Generalized Super-Twisting Algorithm," in *International Conference on Electrical Engineering, Computing Science and Automatic Control (CCE)*, pp. 1–6, IEEE, 2009.

[69] B. Sumantri, N. Uchiyama, and S. Sano, "Generalized super-twisting sliding mode control with a nonlinear sliding surface for robust and

energy-efficient controller of a quad-rotor helicopter," *Proceedings of the Institution of Mechanical Engineers, Part C: Journal of Mechanical Engineering Science*, vol. 231, no. 11, pp. 2042–2053, 2017.

[70] R. Akbar and N. Uchiyama, "Adaptive modified super-twisting control for a quadrotor helicopter with a nonlinear sliding surface," in *SICE International Symposium on Control Systems (SICE ISCS)*, pp. 93–98, 2017.

[71] S.-H. C. Ying-Jeh Huang, Tzu-Chun Kuo, "Adaptive sliding-mode control for nonlinear systems with uncertain parameters," *IEEE Transactions on Systems, Man, and Cybernetics, Part B (Cybernetics)*, vol. 38, pp. 534–539, Apr 2008.

[72] H. Lee and V. I. Utkin, "Chattering suppression methods in sliding mode control systems," *Annual Reviews in Control*, vol. 31, pp. 179–188, Jan 2007.

[73] F. Plestan, Y. B. Shtessel, V. Bregeault, and A. S. Poznyak, "New methodologies for adaptive sliding mode control," *International Journal of Control*, vol. 83, no. 9, pp. 1907–1919, 2010.

[74] Y. B. Shtessel, M. Taleb, and F. Plestan, "A novel adaptive-gain supertwisting sliding mode controller: Methodology and application," *Automatica*, vol. 48, no. 5, pp. 759–769, 2012.

[75] N. Promkajin and M. Parnichkun, "Attitude and altitude control of a four-rotor hovercraft using sliding mode control with adaptive sliding surface," in *IEEE International Conference on Robotics and Biomimetics*, pp. 1285–1290, IEEE, 2011.

[76] V. I. Utkin and J. Shi, "Integral sliding mode in systems operating under uncertainty conditions," in *IEEE Conference on Decision and Control*, vol. 4, pp. 4591–4596, IEEE, 1996.

[77] K. Nonaka and H. Sugizaki, "Integral sliding mode altitude control for a small model helicopter with ground effect compensation," in *American Control Conference*, pp. 202–207, 2011.

[78] F. Piltan, N. Sulaiman, S. Soltani, M. H. Marhaban, and R. Ramli, "An adaptive sliding surface slope adjustment in PD sliding mode fuzzy control for robot manipulator," *International Journal of Control and Automation*, vol. 4, no. 2, pp. 65–76, 2016.

[79] A. Kareem and M. F. Azeem, "A novel adaptive super-twisting sliding mode controller with a single input-single output fuzzy logic control based moving sliding surface," *International Journal of Control and Automation*, vol. 6, no. 3, pp. 183–198, 2013.

[80] T. Orlowska-Kowalska, M. Kamiński, and K. Szabat, "Implementation of a sliding-mode controller with an integral function and fuzzy gain value for the electrical drive with an elastic joint," *IEEE Transactions on Industrial Electronics*, vol. 57, no. 4, pp. 1309–1317, 2010.

[81] F. Yorgancioglu and H. Komurcugil, "Decoupled sliding-mode controller based on time-varying sliding surfaces for fourth-order systems," *Expert Systems with Applications*, vol. 37, no. 10, pp. 6764–6774, 2010.

[82] M. U. Salamci and G. S. Tombul, "Sliding mode control design with time varying sliding surfaces for a class of nonlinear systems," in *IEEE Conference on Computer Aided Control System Design*, pp. 996–1001, IEEE, 2006.

[83] S. Tokat, I. Eksin, M. Güzelkaya, and M. Söylemez, "Design of a sliding mode controller with a nonlinear time-varying sliding surface," *Transactions of the Institute of Measurement and Control*, vol. 25, no. 2, pp. 145–162, 2003.

[84] C. Binglong, L. Xiangdong, and C. Zhen, "Exponential time-varying sliding mode control for large angle attitude eigenaxis maneuver of rigid spacecraft," *Chinese Journal of Aeronautics*, vol. 23, no. 4, pp. 447–453, 2010.

[85] D. Fulwani, B. Bandyopadhyay, and L. M. Fridman, "Non-linear sliding surface: towards high performance robust control," *IET Control Theory & Applications*, vol. 6, no. 2, p. 235, 2012.

[86] A. E. K. Abd El, N. Uchiyama, and S. Sano, "Energy saving in feed drive systems using sliding-mode-based contouring control with a nonlinear sliding surface," *IEEE/ASME Transactions on Mechatronics*, vol. 20, no. 2, pp. 572–579, 2015.

[87] S. Mobayen, "An LMI-based robust controller design using global nonlinear sliding surfaces and application to chaotic systems," *Nonlinear Dynamics*, vol. 79, no. 2, pp. 1075–1084, 2015.

[88] A. Boubakir, F. Boudjema, C. Boubakir, and S. Labiod, "A fuzzy sliding mode controller using nonlinear sliding surface applied to the coupled tanks system," *International Journal of Fuzzy Systems*, vol. 10, no. 2, pp. 112–118, 2008.

[89] A. Boubakir, F. Boudjema, and S. Labiod, "A neuro-fuzzy-sliding mode controller using nonlinear sliding surface applied to the coupled tanks system," *International Journal of Automation and Computing*, vol. 6, no. 1, pp. 72–80, 2009.

[90] W. J. Cao and J. X. Xu, "Nonlinear integral-type sliding surface for both matched and unmatched uncertain systems," *IEEE Transactions on Automatic Control*, vol. 49, no. 8, pp. 1355–1360, 2004.

[91] S. Mondal and C. Mahanta, "Nonlinear sliding surface based second order sliding mode controller for uncertain linear systems," *Communications in Nonlinear Science and Numerical Simulation*, vol. 16, no. 9, pp. 3760–3769, 2011.

[92] Q. Hu, "Variable structure maneuvering control with time-varying sliding surface and active vibration damping of flexible spacecraft with input saturation," *Acta Astronautica*, vol. 64, no. 11-12, pp. 1085–1108, 2009.

[93] B. Sumantri, N. Uchiyama, S. Sano, and Y. Kawabata, "Robust tracking control of a quad-rotor helicopter utilizing sliding mode control with a nonlinear sliding surface," *Journal of System Design and Dynamics*, vol. 7, no. 2, pp. 226–241, 2013.

[94] J. J. Rath, K. C. Veluvolu, and M. Defoort, "Active control of nonlinear suspension system using modified adaptive supertwisting controller," *Discrete Dynamics in Nature and Society*, vol. 2015, 2015.

[95] I. A. Raptis and K. K. Valavanis, *Linear and nonlinear control of small-scale unmanned helicopters*. Springer, 2011.

[96] T. Hamel, R. Mahony, R. Lozano, and J. P. Ostrowski, "Dynamic modelling and configuration stabilization for an X4-flyer," in *IFAC Proceedings Volumes (IFAC-PapersOnline)*, vol. 15, pp. 217–222, 2002.

[97] H. Katayama and H. Aoki, "Straight-line trajectory tracking control for sampled-data underactuated ships," *IEEE Transactions on Control Systems Technology*, vol. 22, no. 4, pp. 1638–1645, 2014.

[98] H. Bouadi, S. Simoes Cunha, A. Drouin, and F. Mora-Camino, "Adaptive sliding mode control for quadrotor attitude stabilization and altitude tracking," in *IEEE International Symposium on Computational Intelligence and Informatics (CINTI)*, pp. 449–455, IEEE, 2011.

[99] V. Lippiello and F. Ruggiero, "Exploiting redundancy in Cartesian impedance control of UAVs equipped with a robotic arm," in *IEEE International Conference on Intelligent Robots and Systems*, pp. 3768–3773, 2012.

[100] Q. Lindsey, D. Mellinger, and V. Kumar, "Construction of cubic structures with quadrotor teams," *Mechanical Engineering*, 2011.

[101] P. E. Pounds, D. R. Bersak, and A. M. Dollar, "Grasping from the air: Hovering capture and load stability," in *IEEE International Conference on Robotics and Automation*, pp. 2491–2498, 2011.

[102] V. Mistler, A. Benallegue, and N. M'Sirdi, "Exact linearization and noninteracting control of a 4 rotors helicopter via dynamic feedback," in *IEEE International Workshop on Robot and Human Interactive Communication*, pp. 586–593, IEEE, 2001.

[103] Y. B. Shtessel, C. Edwards, L. M. Fridman, and A. Levant, *Sliding mode control and observation*. Control Engineering, New York, NY: Springer New York, 2014.

[104] F. Chen, R. Jiang, K. Zhang, B. Jiang, and G. Tao, "Robust backstepping sliding mode control and observer-based fault

estimation for a quadrotor UAV," *IEEE Transactions on Industrial Electronics*, pp. 5044–5056, 2016.

[105] J. A. Moreno and M. Osorio, "Strict lyapunov functions for the super-twisting algorithm," *IEEE Transactions on Automatic Control*, vol. 57, no. 4, pp. 1035–1040, 2012.

[106] X. Yu, Y. Fu, P. Li, and Y. Zhang, "Fault-tolerant aircraft control based on self-constructing fuzzy neural networks and multivariable SMC under actuator faults," *IEEE Transactions on Fuzzy Systems*, pp. 2324 – 2335, 2017.

[107] A. E. Rodríguez-Mata, I. González-Hernández, J. G. Rangel-Peraza, S. Salazar, and R. L. Leal, "Wind-gust compensation algorithm based on high-gain residual observer to control a quadrotor aircraft: real-time verification task at fixed point," *International Journal of Control, Automation and Systems*, vol. 16, pp. 856–866, Apr 2018.

[108] E. Smeur, G. de Croon, and Q. Chu, "Cascaded incremental nonlinear dynamic inversion for MAV disturbance rejection," *Control Engineering Practice*, vol. 73, pp. 79–90, Apr 2018.

[109] J. A. Moreno, "On strict Lyapunov functions for some non-homogeneous super-twisting algorithms," *Journal of the Franklin Institute*, vol. 351, no. 4, pp. 1902–1919, 2014.

[110] H. K. Khalil, *Nonlinear systems*. Prentice Hall, 2002.

Appendix A

Appendix

A.1 Overview of Reduced-Order Observer

In the work of Katayama and Aoki [29], they considered a nonlinear sampled-data strict-feedback system as follows:

$$\dot{\zeta}_1 = f_1(\zeta_1) + g_1(\zeta_1)\zeta_2$$

$$\dot{\zeta}_2 = f_2(\zeta_1, \zeta_2, u) \tag{A.1}$$

$$y_1(k) = \zeta_1(kT)$$

where $\zeta_1 \in \Re^{n_1}$ and $\zeta_2 \in \Re^{n_2}$ are continuous time states, $u \in \Re^m$ is the control input realized through a zero order hold, and $y_1 \in \Re^{n_1}$ is a sampled output from the sensor, and $T > 0$ is a sampling period. The system in Eq. (A.1) naturally appears in the digital control of mechanical systems where ζ_1 and ζ_2 express the position and velocity, respectively, and $y_1(k) = \zeta_1(kT)$ means that only the position measurement at each sampling time is available for control. It is also assumed that

A1: The mappings f_1, f_2, and g_1 are smooth over the compact domain of interest, $f_1(0) = 0$, and $f_2(0, 0, 0) = 0$.

A2: The $m \times m$ matrix $\Phi(\cdot) = g_1(\cdot)^T g_1(\cdot)$ is nonsingular and its inverse is

bounded over the compact domain of interest.

Let $u(t) = u(kT) =: u(k)$ for any $t \in [kT, (k+1)T)$. Then the difference equations corresponding to the exact model and the Euler approximate model of the system in Eq. (A.1) are given by

$$
\begin{aligned}
\eta_1(k+1) =& \eta_1(k) + \int_{kT}^{(k+1)T} [f_1(\eta_1(s)) + g_1(\eta_1(s))\eta_2(s)]\mathrm{d}s \\
\eta_2(k+1) =& \eta_2(k) + \int_{kT}^{(k+1)T} [f_2(\eta_1(s), \eta_2(s), u(k))]\mathrm{d}s \\
y_1(k) =& \eta_1(k)
\end{aligned}
\tag{A.2}
$$

and

$$
\begin{aligned}
\eta_1(k+1) =& \eta_1(k) + T[f_1(\eta_1(k)) + g_1(\eta_1(k))\eta_2(k)] \\
\eta_2(k+1) =& \eta_2(k) + T[f_2(\eta_1(k), \eta_2(k), u(k))] \\
y_1(k) =& \eta_1(k),
\end{aligned}
\tag{A.3}
$$

respectively. Note that $(\zeta_1, \zeta_2)(kT) = (\eta_1, \eta_2)(k)$ for the exact model. The exact model cannot be generally computable, and hence the Euler approximate model is used for design purpose. Then the following equation

$$
\hat{\eta}_2(k+1) = (I - TH)\hat{\eta}_2(k) + TN_T(y_1(k), \rho y_1(k), u(k))
\tag{A.4}
$$

can be a reduced-order observer of the Euler model in Eq. (2.18), where $H = \mathrm{diag}\{h_1, \ldots, h_{n_2}\}$, $|1 - Th_i| < 1$, $i = 1, \ldots, n_2$, ρ denotes the shift operator,

$$
\begin{aligned}
(\rho y_1)(k) =& y_1(k+1) \\
N_T(y_1, \rho y_1, u) =& H\Psi_T(y_1, \rho y_1) + f_2(y_1, \Psi_T(y_1, \rho y_1), u) \\
\Psi_T(y_1, \rho y_1) =& \Phi(y_1)^{-1} g_1(y_1)^T \cdot \left\{ \frac{\rho y_1 - y_1}{T} - f_1(y_1) \right\}
\end{aligned}
$$

This observer is semiglobal and practical in T for the exact model in Eq. (A.2), i.e., there exist $\beta \in \mathcal{KL}$ such that for any $D > d > 0$ and the compact

sets $\Omega_1 \in \Re^{n_1}$, $\Omega_2 \in \Re^{n_2}$, $U \in \Re^m$ we can find $T^* > 0$ with the property that $||\eta_2(0) - \hat{\eta}_2(0)|| \leq D$ and $\eta_1(k) \in \Omega_1$, $\eta_2(k) \in \Omega_2$, and $u(k) \in U$ for any $k \geq 0$ imply $||\eta_2(k) - \hat{\eta}_2(k)|| \leq \beta(||\eta_2(0) - \hat{\eta}_2(0)||, kT) + d$ for all $T \in (0, T^*)$ [29], where $\beta \in \mathcal{KL}$ means that for any fixed $t \geq 0$, a function $\beta(\cdot, t)$ is continuous, zero at zero, strictly increasing, and for each fixed $s \geq 0$, $\beta(s, \cdot)$ is decreasing to zero as its argument tends to infinity [110]. The robustness of the observer in Eq. (A.4) against sampled observation noise was also discussed in [97].